Tunable Terahertz Components on Substrateless Silicon Platform

by

Panisa Dechwechprasit

B Eng (Biomedical Engineering),
Srinakharinwirot University, Thailand, 2017
M Sc (Computer Science and Information Engineering),
National Formosa University, Taiwan, 2019

Thesis submitted for the degree of

Doctor of Philosophy

in

School of Electrical & Mechanical Engineering
Faculty of Sciences, Engineering & Technology
The University of Adelaide

October, 2023

Supervisors:
Prof. Withawat Withayachumnankul,
School of Electrical & Mechanical Engineering, The University of Adelaide
Prof. Christophe Fumeaux,
School of Electrical Engineering & Computer Science, The University of Queensland

© 2023
Panisa Dechwechprasit
All Rights Reserved

Contents

Contents iii

Abstract v

Originality Declaration vii

Acknowledgments ix

Publications xi

List of Figures xiii

List of Tables xvii

Chapter 1. Introduction 1

- 1.1 Terahertz technology . . . 3
- 1.2 Existing terahertz waveguides . . . 6
  - 1.2.1 Microwave-inspired waveguides . . . 6
  - 1.2.2 Photonic-inspired waveguides . . . 7
- 1.3 Substrateless dielectric waveguide platform . . . 9
- 1.4 Integrated terahertz resonators . . . 11
  - 1.4.1 Disk resonators . . . 12
  - 1.4.2 Metallic resonators . . . 13
  - 1.4.3 Photonic crystal cavities . . . 14
- 1.5 Tunable terahertz structures . . . 16
  - 1.5.1 Optical tuning . . . 16
  - 1.5.2 Electrical tuning . . . 19
- 1.6 Thesis outline and original contributions . . . 24

Chapter 2. Terahertz disk resonator on substrateless waveguide platform 27

2.1 Introduction 29
2.2 Design principles 30
2.3 Fabrication and measurement 32
2.4 Results and Discussion 33
2.5 Photoconductive tuning of the resonance 36
2.6 Conclusion 39

Chapter 3. 1-to-N Terahertz Integrated Switches Enabling Multi-beam Antennas 41

3.1 Introduction 43
3.2 Design and principle of operation 44
3.3 Fabrication and measurement 48
3.4 Demonstration of terahertz switches 50
3.5 Multi-beam switching with integrated antenna 53
3.6 Conclusion 59

Chapter 4. Terahertz modulators on substrateless silicon platform 61

4.1 Introduction 63
4.2 Proposed design 64
    4.2.1 Overview of the structure 64
    4.2.2 Modulation principle 66
4.3 Fabrication and measurement 69
4.4 Results and discussion 70
4.5 Conclusion 73

Chapter 5. Summary and Outlook 75

5.1 Thesis conclusion 76
5.2 Outlook 76

Bibliography 79

Biography 91

Abstract

The integration and portability of terahertz systems is vital for practical applications in sensing and communications. In recent years, a substrateless silicon platform based on effective-medium-cladded waveguides has emerged as a promising pathway for realising diverse active and passive components monolithically combined for terahertz integrated systems. This platform is realised using high-resistivity silicon that has exceptionally low loss to terahertz waves. On the basis of the effective medium concept, a subwavelength hole array created into such a silicon slab results in a homogeneous material with a refractive index lower than that of solid silicon. As a consequence, controlling the array configuration yields a high contrast of refractive indices between a solid silicon waveguide core and cladding made of effective medium, while entailing design flexibility for various components. Inheriting characteristics from its constituting high-resistivity silicon, the platform has demonstrated remarkably low attenuation in broad bandwidth. Within this platform, diverse passive components can be created, such as filters, waveguide crossings, 2D horn antennas, or frequency- and polarisation-division multiplexers. However, this platform is yet still constrained by the absence of tunable components, thereby limiting its potential for a broader range of applications.

This thesis focuses on the development of efficient tunable terahertz components on the substrateless silicon platform for applications requiring sensing, switching, and modulation. One contribution involves, a series of disk resonators that are integrated onto the substrateless silicon platform to achieve a high-Q factor. Photoexcitation of selected areas of the silicon-based platform populates free carriers, resulting in the switchability of the resonance. Leveraging this photoexcitation effect, integrated disk resonators are employed to introduce switching functionality. The proposed switch achieves low insertion loss and directional switching capabilities. Moreover, the switch is monolithically integrated with a Luneburg lens on the same platform to function as a beam switching antenna.

In terahertz communications, achieving efficient control over the modulator of terahertz waves is beneficial. We have proposed the integration of a photonic crystal cavity and a dipole resonator into the substrateless silicon platform to create an optically tunable terahertz modulator. This modulator has shown enhanced modulation depth with high efficiency and low required optical power.

The proposed tunable components on the substrateless silicon platform showcase the potential to serve various functions, including sensing, switching, wave routing, and modulation. This contributes to a promising pathway for the development of future terahertz integrated systems.

Originality Declaration

I certify that this work contains no material which has been accepted for the award of any other degree or diploma in my name, in any university or other tertiary institution and, to the best of my knowledge and belief, contains no material previously published or written by another person, except where due reference has been made in the text. In addition, I certify that no part of this work will, in the future, be used in a submission in my name, for any other degree or diploma in any university or other tertiary institution without the prior approval of the University of Adelaide and where applicable, any partner institution responsible for the joint award of this degree.

I give permission for the digital version of my thesis to be made available on the web, via the University's digital research repository, the Library Search and also through web search engines, unless permission has been granted by the University to restrict access for a period of time.

25 October 2023

Signed

Date

Acknowledgments

First and foremost, I would like to express my deepest gratitude to my supervisors Prof. Withawat Withayachumnankul and Prof. Christophe Fumeaux, who gave me an opportunity to pursue my Ph.D.

Prof. Withayachumnankul graciously welcomed me as a Ph.D. candidate even though I had little background in applied electromagnetics back in 2019. He patiently taught and guided me at every step of my research. His extensive knowledge and experience in terahertz technology proved invaluable in shaping my research and nurturing my scholarly development. He has provided me with numerous opportunities to enhance my collaborative research and teaching capabilities through his RF course. He was also incredibly generous with his time even on weekends to assist me with any questions I had. I deeply appreciate that he was always there when I needed guidance. Without his support and encouragement, I would not have been able to succeed in pursuing my Ph.D. journey and gaining research experience. I am deeply grateful for the privilege of having him as my principal supervisor.

I sincerely and profoundly acknowledge the invaluable guidance and unwavering support of my esteemed co-supervisor, Prof. Fumeaux. His mentorship has been instrumental in shaping my academic journey and research endeavours. He is an outstanding scholar in electromagnetics. With his profound knowledge in electromagnetics, he has been generously and patiently shared his wealth of knowledge with me in the realm of electromagnetics. His kindness and selfless dedication to students will forever serve as a source of inspiration for me. He is like a father figure who consistently encourages and guides me on the right path throughout my Ph.D. journey. I am profoundly appreciative to have him as co-supervisor.

I would also like to take this opportunity to express my gratitude to Dr. Rajour, Ako Sharath Sriram, and Prof. Sharath Sriram from the Functional Materials and Microsystems Research Group and The Micro Nano Research Facility at RMIT University in Melbourne for their invaluable assistance in fabricating the High-Q disk resonators and optical modulator samples. I would also like to express my gratitude to Mr. Jacky He and Dr. Gloria Qiu from ANFF-NSW, Research and Prototype Foundry, The University of Sydney for their assistance in fabricating the terahertz switches and switching beam antennas. I would also like to convey my special thanks to Dr. Andy Boes for providing the laser and microscope camera to facilitate the completion of my experiments.

Throughout my Ph.D. journey, I have been fortunate to receive abundant support from scientists and experts across various disciplines. Their assistance was indispensable in ensuring the successful completion of my degree. Here, I would like to specially thanks Mr. Danny Di Giacomo, Mr. Bradon Pullen, Mr. Alban O'Brien, and Mr. Norio Itsumi form the school workshop for their contributions to fabrications. Additionally, I extend appreciation to the school and the faculty for their support during my candidature, specifically recognising Prof. Nelson Tansu, Ms. Charlotte Juhasz, and Mr. David Bowler.

I am also thankful for my colleagues in both the Terahertz Engineering Laboratory and the Applied Electromagnetics Group at the University of Adelaide, Dr. Daniel Headland, Dr. Wendy S. L. Lee, Dr. Weijie Gao, Dr. Mohamed Shehata, Dr. Xiaolong You, Dr. Xiaojing (Alex) Lv, Dr. Shengjian (Jammy) Chen, Dr. Nghia Nguyen Trong, Dr. Siti Nailah Mastura Zainarry, Dr. Quoc Hung Dang, Dr. Purna Bdr Samal, Dr. Xiaoyang Yin, Ms. Yuan (Grace) Yuan, Mr. Mingxiang (Stephen) Li, Mr. Harrison Lees, Mr. Bryce Chung, Ms. Linxi Chen, Mr. Sakib Quader, Ms. Mariam Mohammed, Mr. Miantong Sun, Mr. Chung Yin Tam, Mr. Patrick Joseph Bartley, Mr. Tianchang Ma. Special thanks go to Mr. Harrison Lees for his support, and assistance in CST simulation, Python programming, terahertz switch measurement, and paper writing throughout my candidature. In addition, I am grateful to Mr. I-Ting (Andy) Lin for taking good care of me, providing support, and encouraging me throughout my Ph.D. journey.

My appreciation goes to the University of Adelaide, Faculty of Sciences, Engineering and Technology, and School of Electrical and Mechanical Engineering for providing me Full-fee Scholarship, ECMS Divisional Scholarship, Frank Perry Travel Scholarship, and ARC Grant Funded Short Term Scholarship. The financial support I received has enabled me to successfully pursue and complete my Ph.D. degree, as well as participate in international conferences to present my research work. Additionally, I am thankful to the Adelaide Graduate Research School for providing the necessary conveniences to successfully complete the Ph.D. program.

Last but not least, my endless appreciation goes to my mother and sister for their unconditional love and support in all my pursuits. Thank you for all that you have provided me. Without the support of both of you, my current achievements would not have been possible.

Publications

Journals

Dechwechprasit-P., Lee-H., Headland-D., Fumeaux-C., and Withayachumnankul-W. (2023). 1-to-N Terahertz Integrated Switches Enabling Multi-beam Antennas, *Optica*, **10**(11), pp. 1551-1558.

Dechwechprasit P., Ako-R. T., Sriram-S., Fumeaux-C., and Withayachumnankul-W. (2023). Terahertz disk resonator on a substrateless dielectric waveguide platform, *Optics Letters*, **48**(17), pp. 4685-4688.

Conferences

Dechwechprasit-P., Fumeaux-C. and Withayachumnankul-W.. (2022). Resonant cavities based on substrateless dielectric waveguide platform for terahertz integrated systems, *TENCON 2022 - 2022 IEEE Region 10 Conference (TENCON)*, Hong Kong, Hong Kong. (Invited).

Dechwechprasit-P., Fumeaux-C. and Withayachumnankul-W.. (2022). Integrated disk resonator on substrateless dielectric waveguide platform for terahertz switch applications, *47th International Conference on Infrared, Millimeter and Terahertz Waves (IRMMW-THz)*, Delft, Netherlands.

Dechwechprasit-P., Fumeaux-C. and Withayachumnankul-W. (2021). Integrated resonant cavities on substrateless terahertz dielectric waveguide platform, *46th International Conference on Infrared, Millimeter and Terahertz Waves (IRMMW-THz)*, Chengdu, China.

Tantisatirapong-S, Dechwechprasit-P., Senavongse-W and Phothisonothai-M. (2017). Time-frequency based coherence analysis of red and green flickering visual stimuli for EEG-controlled applications, *9th International Conference on Knowledge and Smart Technology (KST)*, Chonburi, Thailand.*

DECHWECHPRASIT-P, PHOTHISONOTHAI-M. AND TANTISATIRAPONG-S. (2016). 9th Biomedical Engineering International Conference (BMEiCON), *9th International Conference on Knowledge and Smart Technology (KST)*, Laung Prabang, Laos.*

Note: Articles with an asterisk are not directly relevant to this thesis.

List of Figures

1.1 Terahertz region . . . 3
1.2 Wireless communication technologies . . . 5
1.3 Atmospheric attenuation . . . 5
1.4 Microwave-inspired waveguides . . . 7
1.5 Terahertz photonic crystal waveguides and associated passive components 8
1.6 Substrateless dielectric waveguide . . . 9
1.7 Existing passive components based on substrateless dielectric waveguide platform . . . 11
1.8 Schematic of disk resonator . . . 12
1.9 Existing disk resonators . . . 13
1.10 Various types of split-ring resonator (SRRs) . . . 14
1.11 Photonic crystal cavity geometry . . . 15
1.12 Simulated transmission profiles of photonic crystal cavity . . . 15
1.13 Terahertz photonic crystal cavity . . . 16
1.14 Integration of metamaterials with semiconductors for optical tuning modulators . . . 17
1.15 Optically tunable terahertz modulators based on 2D materials . . . 19
1.16 Electrically tunable terahertz modulators based on metamaterials . . . 20
1.17 Electrically tunable terahertz metamaterials based on graphene plasmonics 21
1.18 Electrical tuning gate-controlled terahertz metasurfaces . . . 22
1.19 Tunable graphene-based and 2DEG-based guided waves integration via electrical tuning . . . 23

2.1 Integrated high-Q terahertz disk resonators on substrateless dielectric waveguide platform . . . 30
2.2 Fabricated samples . . . 33
2.3 Measurement setup with a fabricated Clad Disk A . . . 33

2.4 Measured normalised transmission profiles of all samples 34

2.5 Normalised transmission amplitude and phase profiles of Clad Disks A, B, and Unclad Disk 35

2.6 Q-factors of the existing spherical resonators, disk resonators, and this work at terahertz frequencies 36

2.7 Photoexcitation measurement setup 37

2.8 Normalised experimental transmission profiles of Clad Disk B under different levels of LED pump power 38

2.9 Normalised simulated reflection profiles of Clad Disk B under unpumped and 19 mW pump power 38

2.10 Measured transmission level of Clad Disk B on resonance at 276.2 GHz against optical fluence 39

3.1 Terahertz 1-to-2 switch using an integrated disk resonator on substrateless dielectric waveguide platform 45

3.2 Simulated transmission and reflection profiles of the 1-to-2 switch in two states, i.e., neutral and pump state 48

3.3 Fabricated 1-to-3 switch for the three-channel device and optical excitation measurement setup 49

3.4 Simulated instantaneous field distributions of the 1-to-3 switch for the three-channel device 50

3.5 Simulated and measured transmission and reflection profiles of the 1-to-3 switch for the three-channel device 52

3.6 Luneburg lens design 54

3.7 Characteristics of the Luneburg lens 56

3.8 Multi-beam switching with the 1-to-3 switch 57

3.9 Simulated and measured radiation patterns of the three-port switched beam at 276.98 GHz 58

4.1 Terahertz amplitude modulator using an integrated dipole resonator and a photonic crystal cavity on substrateless dielectric waveguide platform 65

4.2 Simulated maximum field distributions for four different structures in two states at 275 GHz 68
4.3 Fabricated modulator 69
4.4 Optical excitation measurement setup 70
4.5 Simulated and measured transmission profiles of the proposed terahertz amplitude modulator 71
4.6 Measured transmission of the terahertz amplitude modulator with offset optical excitation 72
4.7 Simulated and measured normalised transmission profiles of the photonic crystal cavity without the dipole 72

List of Tables

2.1 Relative permittivity and dimensions for different designs 31
2.2 Parameters for photoexcitation 37

3.1 Normalised transmission coefficient of the 1-to-3 switch at 276.1 GHz . . 51

Chapter 1

Introduction

THE terahertz spectrum lies in between the microwave and infrared frequency regimes. This portion of spectrum has promising potential in several areas, including communications, sensing, imaging, and spectroscopy. The recent development and demonstration of terahertz integrated systems have indicated the indispensable role played by tunable terahertz components in enabling a wide range of applications within the field. This chapter presents a background knowledge on terahertz technologies, existing terahertz waveguides, substrateless dielectric waveguide platforms, resonant cavities, and tunable integrated structures, along with an outline of the thesis.

1.1 Terahertz technology

Terahertz waves refer to electromagnetic waves at frequencies from 0.1 to 10 THz, which is the spectrum range situated between the microwave and infrared bands, as shown in Fig. 1.1. The terahertz region is also broadly referring to the entire range of the submillimeter-wave (sub-MMW) band that fills the frequency range between 300 GHz and 3 THz. Terahertz waves have shown unique characteristics including non-ionising radiation, strong penetration into non-conducting materials, and the capability of supporting high data rates due to wide bandwidth. These properties are promising for a comprehensive range of applications such as sensing, non-invasive imaging, high-speed communications, radar, security, non-destructive testing, and biomedicine.

However, the terahertz frequency range has traditionally been underutilised owing to a lack of efficient transmitters and detectors. One of the main difficulties with generating and detecting terahertz radiation is the lack of suitable materials that can operate effectively in this frequency range. Additionally, terahertz radiation is absorbed by water vapour, which combined with the lack of efficient sources, makes it difficult to transmit over long distance. Therefore, one primary research topic is to develop sources that can effectively generate terahertz radiation. Leveraging laser-based technologies, the development of photonic terahertz wave generation through optical-to-terahertz signal conversion has gradually filled up the terahertz gap. One remarkable approach involves using ultrafast lasers, particularly femtosecond lasers, to generate terahertz waves through optical-to-terahertz conversion, utilising nonlinear optical materials, photoconductors, and photodiodes (Nagatsuma, 2011).

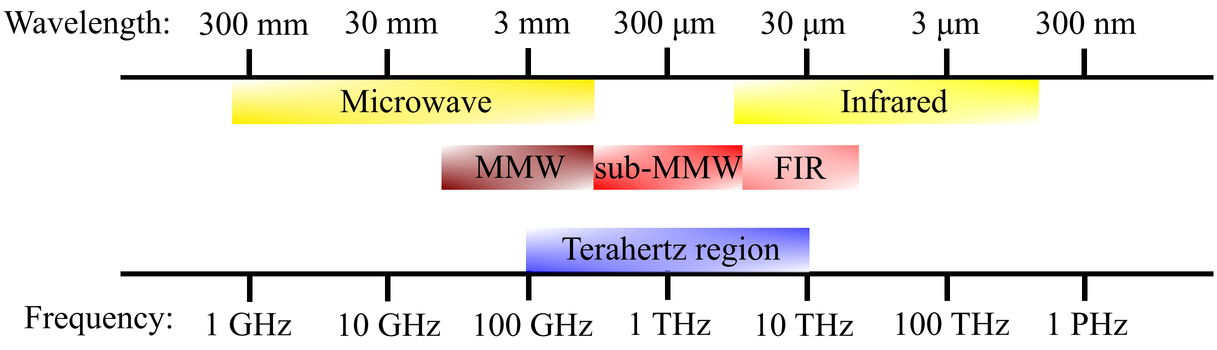

Figure 1.1. Terahertz region. The terahertz frequency band is located between the microwave and infrared regions.

Laser-based technologies open up the development of terahertz applications including spectroscopy, imaging, and communications. Particularly terahertz time-domain spectroscopy (THz-TDS), is used for material characterisation by determining the absorption coefficient and refractive index of the materials of interest. In addition, terahertz waves have shown their usefulness for detection and inspection of biological molecules, tissues, and pharmaceuticals for biomedical imaging and sensing. While the development of photonic terahertz wave generation through optical-to-terahertz signal conversion has significantly contributed to bridging the terahertz gap, it is essential to acknowledge the concurrent efforts from electronic-based technologies. These endeavours involve the development of transistor technologies capable of reaching the terahertz frequency range. Notably, technologies utilising silicon-based platforms, such as CMOS, SiGe, and III-V-based transistors, have demonstrated substantial progress in generating terahertz power. The continuous enhancement of $f_{\max}$ in these electronic devices can reach frequencies beyond 1 THz (Urteaga *et al.*, 2017; Schroter and Pawlak, 2018) with further increase projected in the future (Arabhavi *et al.*, 2022; Whitaker *et al.*, 2023).

Recently, there has been an increasing bandwidth demand from network applications, such as mobile services, high-resolution video downloads, ultra high definition video data, internet of things (IoT) devices, and 6G communications. In order to keep up with the rich multimedia requirements, a higher data rate in wireless communications is indispensable. To achieve such high data rates, the use of electromagnetic waves at terahertz frequencies is promising due to the extremely large available bandwidth (Nagatsuma *et al.*, 2016). In wireless communications technologies, the data rate is theoretically related to the carrier frequency as shown in Fig. 1.2. A terahertz channel has shown the potential to achieve data rates of up to 1 Tbit/s over several kilometers of distance (Koenig *et al.*, 2013).

In terms of enabling technologies, the development at terahertz frequencies is most practical with the incorporation of semiconductor electronic devices and integrated circuits (Nagatsuma, 2011). However, the practicality of terahertz applications is challenging due to the strong atmospheric attenuations (Nagatsuma, 2011), scattering losses, and material losses (Withayachumnankul *et al.*, 2018; Schneider *et al.*, 2012; Nagatsuma *et al.*, 2016). As shown in Fig. 1.3, the atmospheric attenuation of electromagnetic waves is 1 dB/10 m at 500 GHz. On the other hand, the scattering loss arises from dust, haze, and rain in the path of propagation, while material losses are primarily from ohmic losses and dielectric substrate losses in the transceivers (Withayachumnankul *et al.*, 2018).

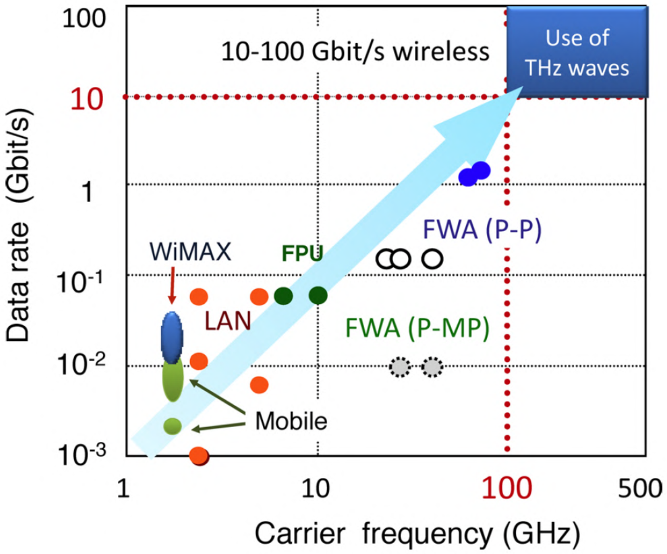

Figure 1.2. Wireless communication technologies. Relationship between data rate and carrier frequency. Adopted from Nagatsuma (2011).

In recent years, terahertz technology has undergone a shift in focus from primarily being a laboratory-based spectroscopy tool to developing terahertz integrated systems for practical applications in sensing, imaging, and communications. To achieve this goal despite the challenge of atmospheric attenuation, integrated platforms with highly

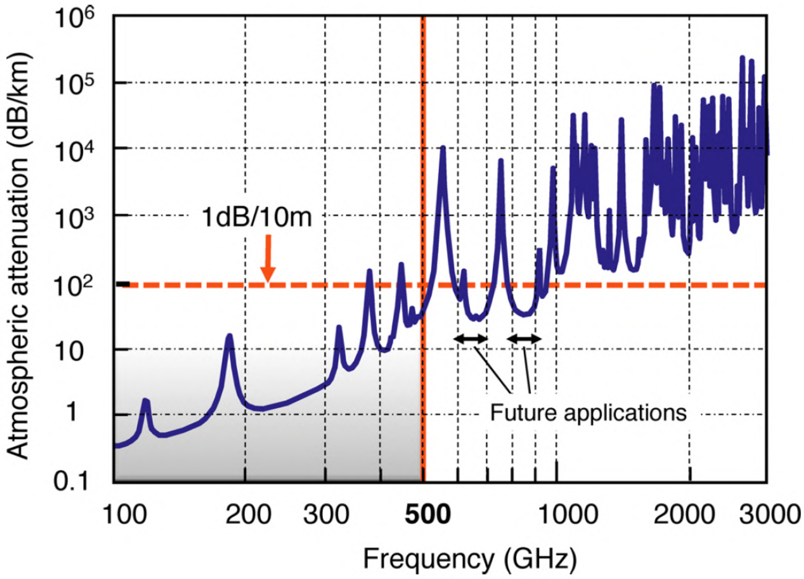

Figure 1.3. Atmospheric attenuation. Atmospheric attenuation of terahertz waves above 100 GHz. Adopted from Nagatsuma (2011).

efficient waveguides, along with integrated tunable components are necessary. These elements play crucial roles in enabling the advancement and implementation of terahertz technology for various practical applications.

1.2 Existing terahertz waveguides

Efficient integrated waveguides are essential components for terahertz integrated systems, as they are the most basic element in an integrated platform. The characteristics of guided wave propagation in a medium are influenced by several factors including frequency, waveguide structure, as well as the properties and behaviour of the surrounding media. This section gives an overview of existing terahertz waveguides categorised into microwave-inspired and photonics-inspired waveguides.

1.2.1 Microwave-inspired waveguides

At terahertz frequencies, conventional microwave-inspired waveguiding platforms have been implemented in the past, including as microstrip lines (Zakaria *et al.*, 2010; Murano *et al.*, 2016), rectangular hollow waveguides (Ding *et al.*, 2017), and substrate-integrated waveguides (SIW) (Bozzi *et al.*, 2011). A microstrip line comprises a thin conducting strip placed on top of a dielectric substrate backed by a ground plane, as illustrated in Fig. 1.4(a). The strip and ground plane serve as the transmission line, while the substrate, along with the air above it, acts as dielectric cladding. Microstrip lines demonstrate the capability to effectively support a quasi transverse electromagnetic (TEM) mode, resulting in minimal dispersion and wide bandwidth, along with a customisable interface for active devices (Pozar, 2011). However, despite their advantages, microstrip waveguides also present a challenge in the form of a significant transmission losses at high frequencies. These losses are caused by ohmic losses in the metal and dielectric losses in the substrate. In contrast, a rectangular hollow waveguide exhibits lower loss because the majority of wave energy propagates through the air when compared to microstrip lines. The low loss of rectangular waveguides has facilitated the development of terahertz components, such as bandpass filters (Ding *et al.*, 2017), however these waveguides are rather bulky 3D structures and therefore are not integrable.

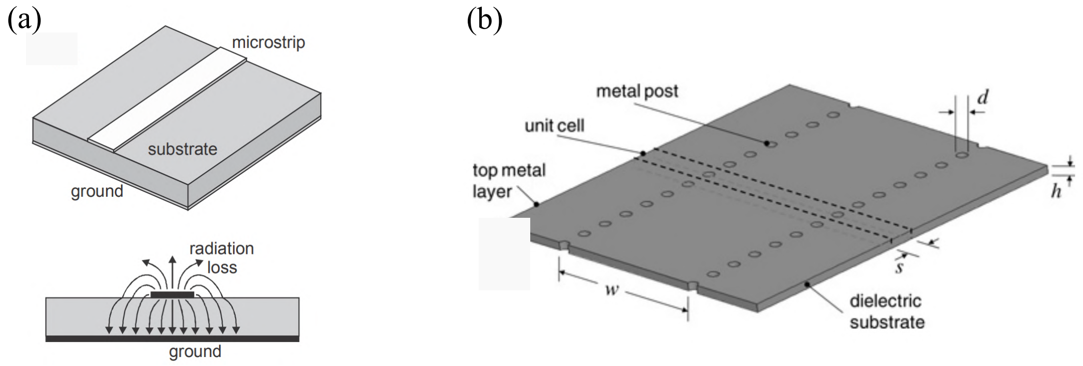

Figure 1.4. Microwave-inspired waveguides. (a) Microstrip lines. Adopted from Zakaria *et al.* (2010), and (b) Substrate-integrated waveguides (SIW). Adopted from Bozzi *et al.* (2011).

Substrate-integrated waveguides (SIWs) fall under the category of planar waveguides. To confine the waves, these waveguides employ two rows of metallic cylinders (Bozzi *et al.*, 2011) or metalised air holes (Wu *et al.*, 2021) embedded in a metal-cladded dielectric substrate, as shown in Fig. 1.4(b). In this way, they exhibit a dispersion behaviour similar to rectangular waveguides, resulting in narrower bandwidths compared to microstrip lines. However, the SIWs are characterised by lower losses at frequencies above 400 GHz and are also capable of supporting multiple modes (Wu *et al.*, 2021), enhancing their versatility for diverse terahertz applications. It is essential to note that SIWs share similar issues with microstrip lines, involving metal and dielectric losses at terahertz frequencies.

1.2.2 Photonic-inspired waveguides

All-dielectric waveguides, such as rectangular dielectric waveguides (Malekabadi *et al.*, 2014), silicon-on-insulator (SOI) waveguides (Amarloo *et al.*, 2018), and photonic crystal waveguides (Tsuruda *et al.*, 2015; Headland *et al.*, 2019), have served as an inspiration for structures guiding terahertz waves, owing to their absence of ohmic losses. Theoretically, terahertz dielectric waveguides share some similarities with optical dielectric waveguides, including their fundamental guiding mechanism. For terahertz waves, recent studies have proposed dielectric rectangular waveguides based on high-resistivity silicon that has exceptionally low loss at terahertz frequencies. This type of waveguides consists of a single dielectric rod (Malekabadi *et al.*, 2014). Facilitated by low loss material, dielectric rectangular waveguides have been utilised as interconnection components for on-chip communications. However, the inherent limitations of a bare waveguide pose challenges in achieving integrated systems, given its absence of structural support and the ability to accommodate additional components.

SOI waveguides are commonly employed in photonic integrated circuits due to their unique optical properties (Jalali *et al.*, 1998). The compatibility of SOI waveguides with standard complementary metal-oxide-semiconductor (CMOS) fabrication processes allows for seamless integration with other electronic and photonic devices on the same silicon chip (Jalali *et al.*, 1998). However, the required supporting substrate has a significant impact on the dielectric loss at terahertz frequencies (Lee *et al.*, 2001).

To realise an integrated platform with low loss and a simple structure, an all-dielectric photonic crystal waveguide has been proposed. Photonic crystal waveguides are periodic structures with bandgap properties that prohibit waves at certain frequencies from propagating through the crystal (Meade *et al.*, 2008). These waveguides possess distinct advantages, such as strong light confinement due to the presence of bandgaps. The use of intrinsic silicon and the absence of substrate lead to low-loss wave guidance with attenuation of less than 0.1 dB/cm (Tsuruda *et al.*, 2015; Yu *et al.*, 2019b). Based on this platform, various passive components have been proposed such as Luneburg lens (Headland *et al.*, 2018) and photonic crystal waveguide (Headland *et al.*, 2019), as illustrated in Fig. 1.5. However, photonic crystal waveguides exhibit relatively narrow bandwidths and pronounced in-band dispersion, which is attributed to the inherent phenomenon of photonic bandgaps.

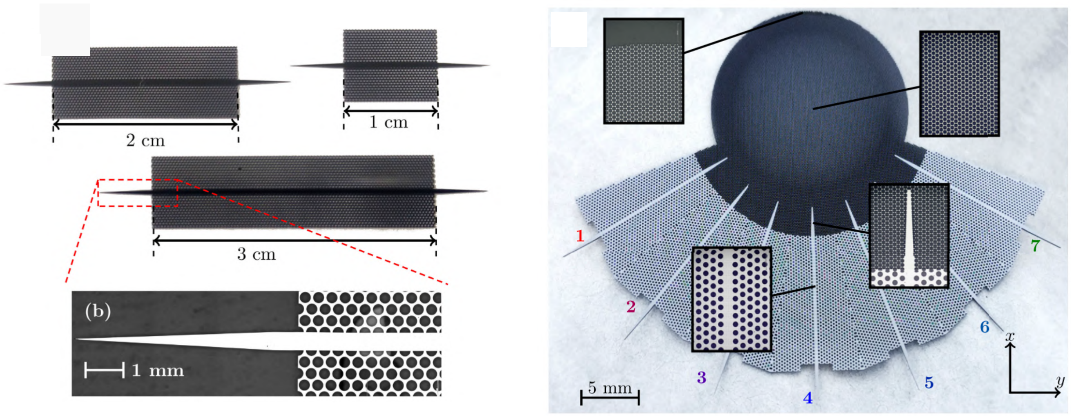

(a)

(b)

Figure 1.5. Terahertz photonic crystal waveguides and associated passive components. (a) Photonic crystal waveguide. Adopted from Headland *et al.* (2019), and (b) Luneburg lens antenna. Adopted from Headland *et al.* (2018).

1.3 Substrateless dielectric waveguide platform

Silicon is a promising candidate for creating waveguide structures due to its excellent mechanical properties and low loss. Silicon micromachining is an ideal technique for developing waveguide components in the terahertz range. A silicon-micromachined waveguide is fabricated using deep reactive-ion etching (DRIE), a dry etching technique that employs plasma to create high-aspect-ratio structures in bulk silicon (Alonso-del Pino *et al.*, 2019). Recently, a remarkable achievement of a terahertz integrated platform has been demonstrated based on effective-medium-cladded waveguides. This platform has been reported to achieve low loss, low dispersion, and broadband operation (Gao *et al.*, 2019, 2020). It holds significant promise as a potential candidate for realising both passive and active components in terahertz integrated systems. The platform is exclusively constructed using high-resistivity silicon with a relative permittivity ϵ_{Si} of 11.68 and a loss tangent of 3×10^{-5}. In this platform, a solid waveguide core is structurally surrounded by an in-plane effective medium, consisting of a subwavelength hole array that creates a lower effective permittivity, as shown in Fig. 1.6. The effective medium cladding allows wave confinement in the solid core through total internal reflection. In this way, we term the device a substrateless dielectric waveguide platform, where the silicon layer acts as wave channels and does not function as a substrate supporting some waveguiding structure above it. This platform can support both

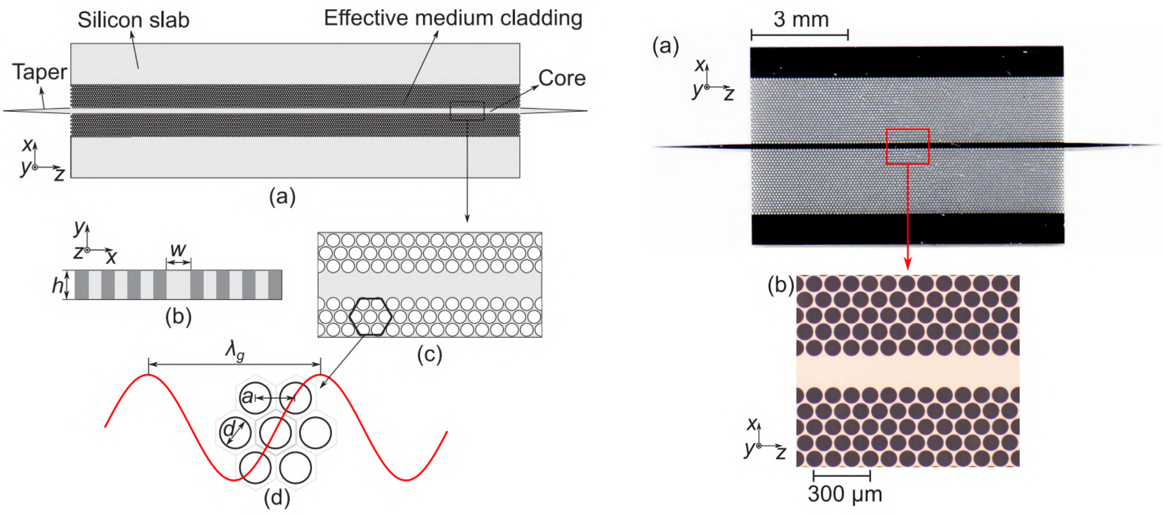

(a) (b)

Figure 1.6. Substrateless dielectric waveguide. (a) Waveguide structure, and (b) Fabricated waveguide. Adopted from Gao *et al.* (2019).

fundamental dielectric waveguide modes, i.e. E^x_{11} and E^y_{11} modes, and demonstrates an impressive record of extremely low attenuation. These modes propagating within this platform exhibit an average loss of 0.075 dB/cm from 220 to 330 GHz for the E^x_{11} mode, while the E^y_{11} mode has an average loss of 1.225 dB/cm from 220 to 260 GHz and 0.135 dB/cm from 260 to 330 GHz (Gao *et al.*, 2020). This platform has demonstrated the ability to achieve lower transmission losses compared to conventional microwave-inspired and photonic-inspired waveguides. The absence of metal and substrate in this platform and the use of an effective medium cladding that behaves as a homogeneous material, as opposed to a dispersive bandgap material, contribute to its improved performance.

This platform has demonstrated its capability to accommodate various passive components, such as filters (Gao *et al.*, 2021b), 2D horn antennas (Liang *et al.*, 2021), waveguide crossings (Lees *et al.*, 2021), and frequency- and polarisation-division multiplexers (Headland *et al.*, 2021b; Gao *et al.*, 2021a), as illustrated in Fig. 1.7. The effective medium concept confers a degree of freedom associated with the properties of the cladding to design and control terahertz transmission. In a study conducted by Gao et al., they utilised the effective medium cladding to realise a Bragg grating filter, as depicted in Fig. 1.7(a), achieving a passband insertion loss below 1.5 dB (Gao *et al.*, 2021b). Furthermore, this platform was shown to be also adaptable for a planar horn antenna, as shown in Fig. 1.7(b), which supported two linear polarisations in the WR-3 band. The antenna achieved an impressive efficiency of almost 100%, owing to the negligible dissipation of the silicon material (Liang *et al.*, 2021). To enable dense circuitry, a waveguide crossing was introduced by Lees *et al.* (2021), as seen in Fig. 1.7(c). Such a waveguide can achieve a low insertion loss of less than 1 dB with an average crosstalk level of −39 dB across 220 to 330 GHz, accommodating both in- and out-of-plane fundamental modes.

Moreover, this platform has facilitated the development of frequency- and polarisation-division multiplexers, as illustrated in Fig. 1.7(d)–(e) (Headland *et al.*, 2021b; Gao *et al.*, 2021a). The frequency multiplexers have demonstrated the capability to accommodate data rates of up to 48 Gbit/s using an on/off keying modulation scheme at the operating frequency of 350 GHz (Headland *et al.*, 2021b). Additionally, the polarisation-division multiplexers exhibit high efficiency, wide bandwidth, and a high polarisation extinction ratio (Gao *et al.*, 2021a). Finally, due to its versatile capabilities and potential for practical system integration, the silicon substrateless dielectric waveguide platform has emerged as a promising candidate for terahertz integrated systems, offering potential to support a wide range of applications in sensing, imaging, and communications.

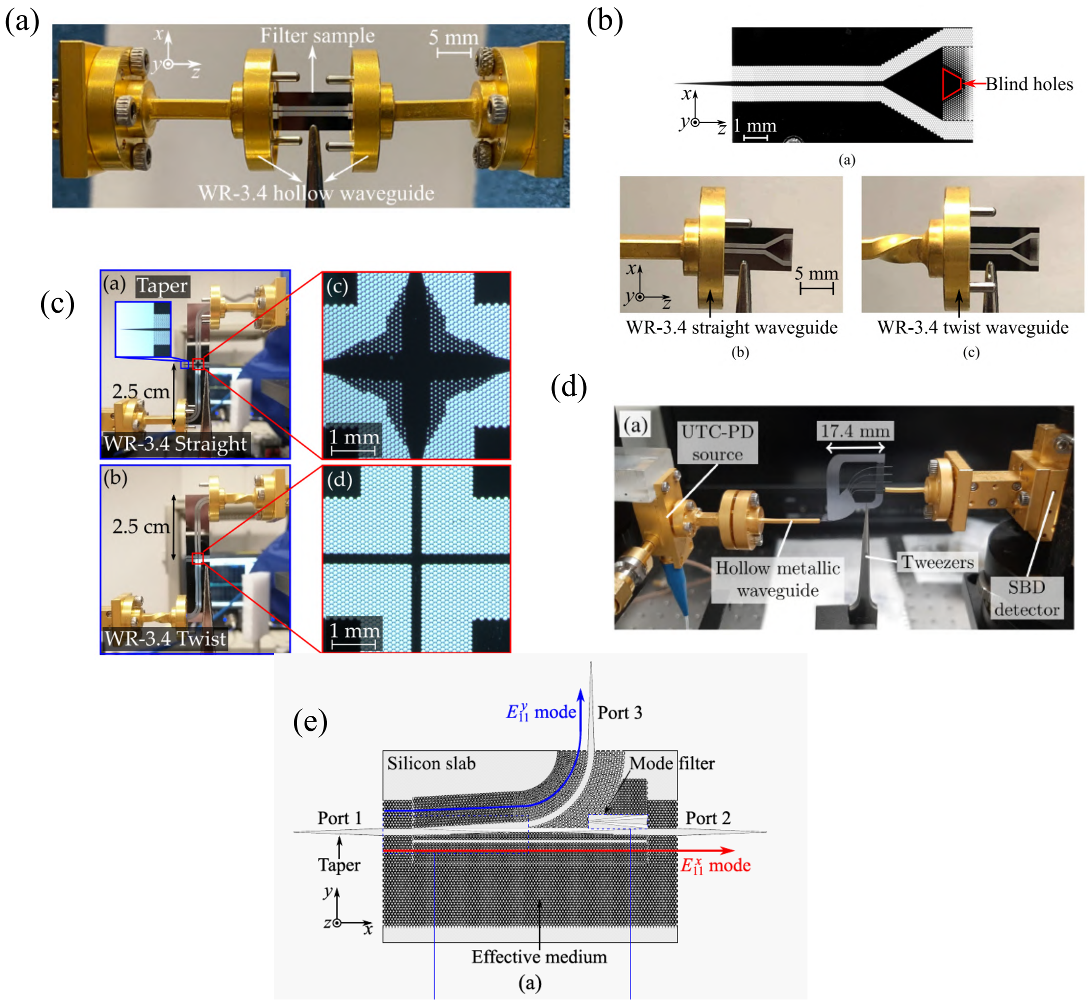
(a)
Filter sample
5 mm
WR-3.4 hollow waveguide
(b)
Blind holes
1 mm
(a)
5 mm
WR-3.4 straight waveguide
(b)
WR-3.4 twist waveguide
(c)
(c)
(a) Taper
2.5 cm
WR-3.4 Straight
(b)
2.5 cm
WR-3.4 Twist
(c)
1 mm
(d)
1 mm
(d)
(a)
UTC-PD source
17.4 mm
Hollow metallic waveguide
Tweezers
SBD detector
(e)
E^y_{11} mode
Port 3
Silicon slab
Mode filter
Port 1
Port 2
Taper
E^x_{11} mode
Effective medium
(a)

Figure 1.7. Existing passive components based on substrateless dielectric waveguide platform. (a) Effective-medium-clad Bragg grating filter. Adopted from Gao *et al.* (2021b), (b) 2D horn antennas. Adopted from Liang *et al.* (2021), (c) Waveguide crossings. Adopted from Lees *et al.* (2021), (d) Frequency-division multiplexers. Adopted from Headland *et al.* (2021b), and (e) Polarisation-division multiplexers. Adopted from Gao *et al.* (2021a).

1.4 Integrated terahertz resonators

In general, the resonance effect of terahertz waves can be achieved using various type of resonators, such as disk resonators, metallic resonators, and photonic crystal cavities. These techniques operate based on the principles of wave confinement. In principle, integrating these resonators into a dielectric waveguide can be exploited for diverse terahertz applications, such as sensing, switching, and modulation.

1.4.1 Disk resonators

Disk resonators operating in high-order modes are also known as whispering gallery resonators, while disk resonators operating in low-order modes are known as dielectric resonators. They are a class of micro- or nano-scale devices that have drawn significant attention in the field of photonics. In a specific mode of a disk resonator, light is trapped and confined at the boundary of the disk, forming circulating standing waves along its perimeter, as illustrated in Fig. 1.8(a). The resonance frequencies of the disk resonator can be determined based on the circumference of the disk and the effective refractive index of the surrounding medium. In disk resonators, the quality factor or Q-factor play a crucial role in determining the sensitivity of devices used in sensing, communications, and material characterisation. The Q-factor is determined by the ratio of the stored energy in the disk resonator to the energy lost per radian of oscillation cycle. The Q-factor is related to the 3-dB bandwidth of the resonance ($f_{3\mathrm{dB}}$) and the resonant frequency f_r and can be expressed by the following equation:

$$Q = \frac{f_r}{\Delta f_{3\mathrm{dB}}} \, . \tag{1.1}$$

To realise such resonator devices, a disk resonator is integrated alongside a waveguide. The working principle of integrated disk resonators is determined by the evanescent coupling of terahertz waves between a disk resonator and an access waveguide, as depicted in Fig. 1.8(b). The transmission of such an integrated disk resonator can be derived as follows (Kuo *et al.*, 2006)

$$H(\theta) = \frac{\tau - \alpha e^{-i\theta}}{1 - \alpha\tau e^{-i\theta}} \, , \tag{1.2}$$

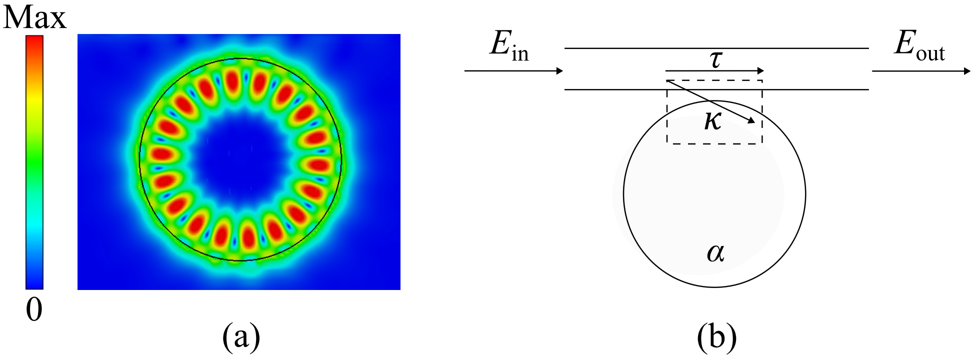

(a)

(b)

Figure 1.8. Schematic of disk resonator. (a) Simulated instantaneous field distributions of the disk resonator. (b) Genetic geometry for waveguide and disk resonator coupling, i.e. κ : coupling constant, τ : transmission constant, and α : loss per circulation.

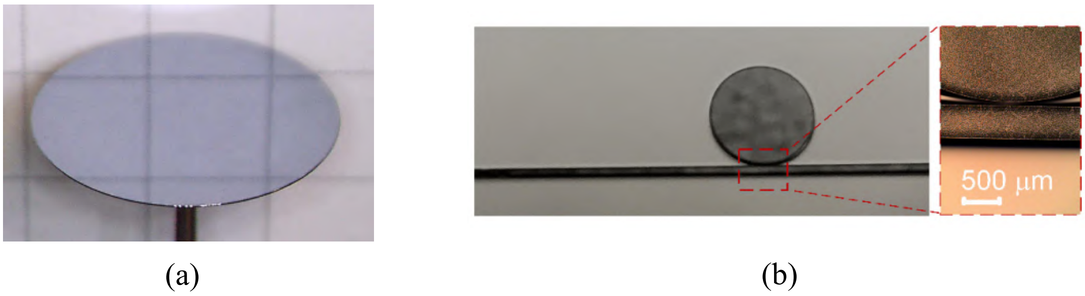

(a) (b)

Figure 1.9. Existing disk resonators. (a) Silicon disc microresonators. Adopted from Vogt *et al.* (2020), and (b) Disk cavity. Adopted from Xie *et al.* (2018).

where τ represents the transmission constant between the disk resonator and the waveguide, α is the sum of all losses including radiation loss and material absorption loss, and θ is the round-trip phase shift. It is important to note that at resonance, i.e., $\theta = 0$, the transmission $H(\theta)$ becomes 0 when $\alpha = \tau$. This condition is referred to as critical coupling (Darmawan and Chin, 2006). If $\alpha < \tau$, the resonance is undercoupled, while if $\alpha > \tau$, the resonator is overcoupled. If the losses are suppressed, disk resonators can achieve a very high Q-factor, typically ranging from hundreds to thousands in the terahertz frequency operation. Furthermore, the resonance of disk resonators made of silicon can be tuned on/off by photoexcitation, that results in photoexcited carriers that are lossy for terahertz waves.

Recently, Vogt et al. in 2020, demonstrated high Q-factor silicon disc microresonators, as shown in Fig. 1.9(a) (Vogt *et al.*, 2020). These resonators achieved a high Q-factor by increasing the disk diameter, which effectively reduced radiation loss. However, it is worth noting that these resonators operated in free-space and had a large volume compared to the operation wavelength, making them less suitable for integrated systems. To realise an integrated platform, a disk cavity and waveguide was integrated on top of a slab (Xie *et al.*, 2018), as illustrated in Fig. 1.9(b). However, the system experienced a low Q-factor of 201 owing to the scattering loss and coupling loss.

1.4.2 Metallic resonators

In the terahertz regime, metallic resonators are promising candidate for manipulating and controlling electromagnetic waves, owing to their distinctive electromagnetic properties. These resonators are commonly fabricated from metals in different geometries, including rectangular, circular, and cylindrical shapes. Various types of subwavelength

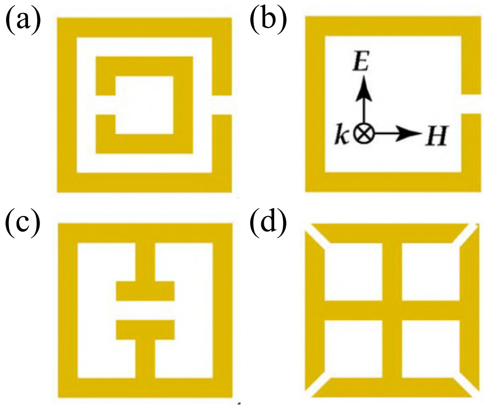

Figure 1.10. Various types of split-ring resonator (SRRs). (a) Double SRR, (b) Single SRR, (c) eSRR, and (d) Four-fold rotational-symmetry eSRR. Adopted from Withayachumnankul and Abbott (2009).

metallic resonators have been proposed based on thin wires, split-ring resonators (SRRs), inductive-capacitive (LC) resonators, etc. (Withayachumnankul and Abbott, 2009). At terahertz frequencies, the responses are commonly demonstrated with planar split-ring resonators with different shapes, as illustrated in Fig. 1.10.

The planar SRRs typically electrically couple to waves propagating in a direction perpendicular to the plane of the SRR. In double SRRs as seen in Fig. 1.10(a), when the polarisation is aligned with the gap, both a LC and a dipole resonances are observed. The presence of a higher relative permittivity in the substrate leads to a redshift in each resonance (Withayachumnankul and Abbott, 2009). Similar behaviour occurs in a single SRRs shown in Figure. 1.10(b), wherein the dipole resonance experiences an influence from the gap (Singh *et al.*, 2009). The LC resonators in Fig. 1.10(c)–(d), in contrast, exhibit a unique characteristic of favouring a purely electric response over a magnetic one. Additionally, the LC resonator, with four-fold rotational symmetry shown in Fig. 1.10(d) demonstrates insensitivity to polarisation (Padilla *et al.*, 2007).

1.4.3 Photonic crystal cavities

A photonic crystal cavity is a type of optical microcavity that is formed by introducing a defect in a photonic crystal. This results in an interaction between electromagnetic waves and confined electromagnetic modes in the cavity. The cavity modes can be defined based on bandgap characteristics (Joannopoulos *et al.*, 1995), and the length of the cavity (L), as shown in Fig. 1.11. The length of the cavity corresponds precisely to

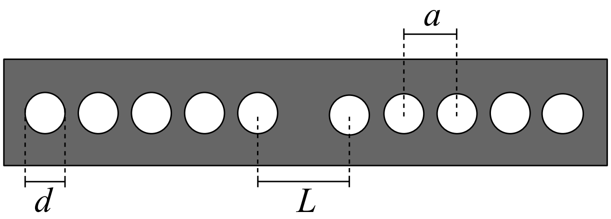

Figure 1.11. Photonic crystal cavity geometry. The period a is a half of the guided wavelength λ_g, and the design is further defined by the hole diameter d and the cavity length L.

a multiple of half the wavelength of the electromagnetic waves, yielding constructive interference and reflection. The Q-factor of a cavity mode can be controlled by adjusting the number of holes n_h between the cavity and waveguide, as a higher number of holes yields a higher Q-factor, as illustrated in Fig. 1.12. Due to their ability to confine strong electromagnetic waves within the cavities, this opens the door to a wide range of applications, including on-chip sensors and modulators.

In the study by Hanham *et al.* (2017), high-Q factor terahertz resonators were achieved by creating photonic crystal cavities within a suspended silicon rectangular waveguide, as shown in Fig. 1.13. The device exhibited strong sensitivity to light, as optical excitation resulted in the generation of electron-hole pairs when photons with energies greater than the bandgap of silicon were absorbed. This process increased conductivity and caused damping of the Q-factor of the resonance. These advantageous properties

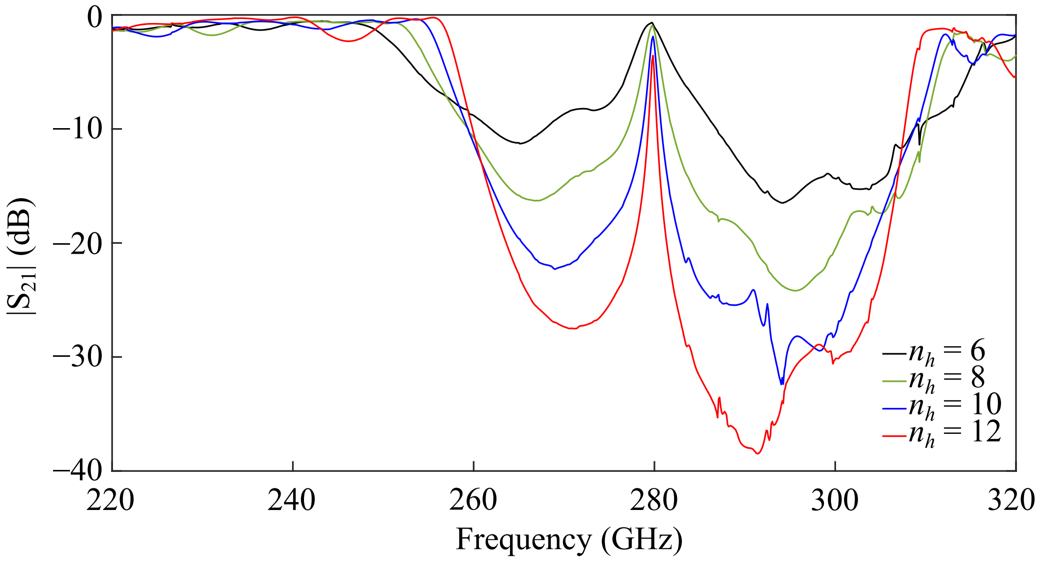

Figure 1.12. Simulated transmission profiles of photonic crystal cavity. As the number of holes n_h increases, a higher Q-factor can be achieved.

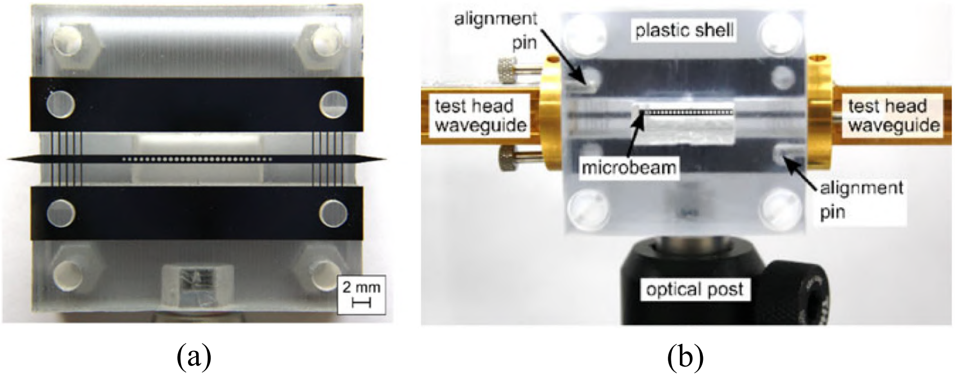

Figure 1.13. Terahertz photonic crystal cavity. (a) Microbeam photonic crystal resonators, and (b) Experimental set up with microbeam resonator sample. Adopted from Hanham *et al.* (2017).

demonstrate a robust light-matter interactions, enabling various applications such as switching, beam steering, and modulation to be achieved through this concept.

1.5 Tunable terahertz structures

The conductivity of semiconductors such as silicon (Si), gallium arsenide (GaAa), and germanium (Ge) can be tuned by modulating their free carrier density through optical or electrical excitation. For the realisation of tunable terahertz structures, such semiconductors can be integrated onto various types of photonic structures, including plasmonics, resonant cavities, photonic crystals, metasurfaces, and waveguides with cavities. This section presents an overview of terahertz modulators mainly existing in the form of free-space devices, rather than guided-wave devices, further categorised according to their tuning modality, namely optical or electrical.

1.5.1 Optical tuning

The use of optical excitation has a distinctive advantage in achieving rapid switching ranging from the microsecond to picosecond scale depending on the recombination time of photo-generated carriers. To achieve tunable control of free-space terahertz waves, various studies have extensively focused on the integration of metamaterials with semiconductors (Padilla *et al.*, 2006; Gu *et al.*, 2012; Okada and Tanaka, 2011; Xie *et al.*, 2013; Zhang *et al.*, 2015; Cheng and Liu, 2013; Lim *et al.*, 2018; Hu *et al.*, 2020b; Tan *et al.*, 2021; Lou *et al.*, 2021) and 2D materials (Srivastava *et al.*, 2017; Hu *et al.*, 2020a). Metamaterials consist of periodic subwavelength metallic structures that interact with both the electric and magnetic components of terahertz waves. These structures can exhibit a diverse range of resonances, including dipole, LC-type, Fano-type, and electromagnetically induced transparency (EIT)-like resonance. Consequently, integrating active materials into metamaterials enables resonance switching and modulation.

For instance, semiconductors such as Si, GaAs, Ge play a crucial role in terahertz switching. The primary demonstration of modulating transmission amplitude was proposed using a GaAs substrate (Padilla *et al.*, 2006), as illustrated in Fig. 1.14(a). This involved an array of copper split-ring resonators patterned on the substrate. The modulation was achieved at 0.56 THz through ultrafast light pumping at 800 nm (Padilla et al., 2006). However, the maximum carrier concentration in GaAs is on the order of 10^{18} cm^{-3}, limiting the conductivity modulation of materials at terahertz frequency (Cui *et al.*, 2019). Moreover, these modulators exhibit a narrow modulation range and high energy loss (Shcherbakov *et al.*, 2017). A silicon-based metadevice offers an alternative approach for achieving a higher modulation depth (Gu *et al.*, 2012), as described in the following. The unit cell comprising SRRs and cut wires with silicon islands within their gaps

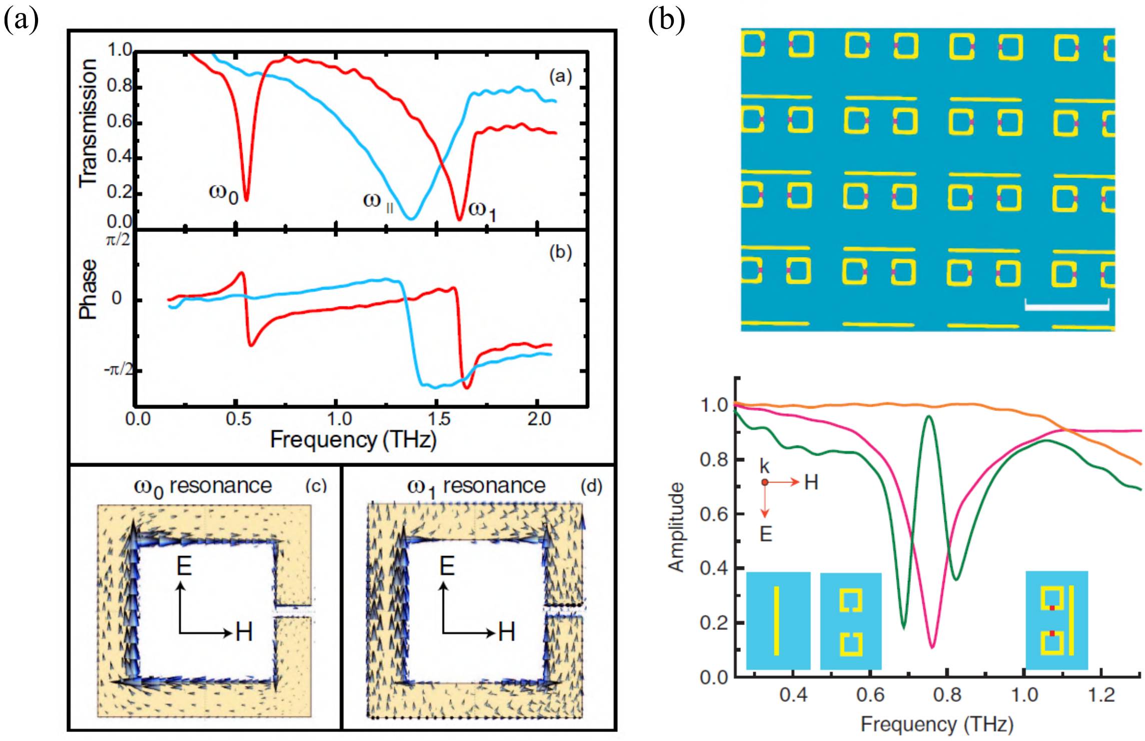

Figure 1.14. Integration of metamaterials with semiconductors for optical tuning modulators. (a) GaAs-based metadevices. Adopted from Padilla *et al.* (2006), and (b) Silicon-based metadevices. Adopted from Gu *et al.* (2012).

formed an EIT metamaterial. These unit cells were integrated onto a silicon-on-sapphire wafer, as shown in Fig. 1.14(b). The device achieved on/off EIT modulation at 0.74 THz through photoexcitation with an optical power of 1350 mW (Gu *et al.*, 2012). However, this device exhibits a narrow band of terahertz modulation, which restricts its suitability for applications requiring broadband operation. To achieve broadband modulation, silicon-based spatial terahertz modulators (Okada and Tanaka, 2011; Xie *et al.*, 2013) and quasi-optical terahertz devices (Zhang *et al.*, 2015; Cheng and Liu, 2013) have been proposed. However, these modulators require a significant optical pump power to achieve sufficient modulation depth, which limits the efficiency of integrated terahertz modulators. In addition, the modulation speed of these devices is limited by the recombination time of excited free carriers in silicon, which is approximately 1 ms.

To enhance modulation speed, germanium (Ge) has been introduced into terahertz tuning platforms due to its higher carrier mobility and shorter carrier lifetime compared to silicon. In Lim *et al.* (2018), a thin germanium film was integrated onto an array of asymmetric SRRs, enabling the realisation of Fano resonances. Optical excitation leads to an accumulation of free carriers in the germanium, bridging the capacitive gaps of the SRRs. As a result, the modulation depth of resonance transmission reached approximately 90% with a rapid recovery time of 17 ps under an optical pump power of 1200 mW. Higher modulation speed can be achieved by exploiting double photoactive layers (Hu *et al.*, 2020b), integrating a germanium strip onto symmetric metallic resonators (Tan *et al.*, 2021), or employing a germanium thin-film hybrid Fano metasurface under dual-stimulus (Lou *et al.*, 2021). However, a fundamental limitation of these Ge-based devices often arises from the requirement of an external pump source with high power density exceeding 1000 μJ cm^{-2} to achieve the desired functionality. This characteristic poses challenges for their practical applications.

Recently, monolayer graphene was introduced as a promising two-dimensional (2D) material for achieving tunable terahertz modulators, owing to the absence of a bandgap. Various studies have proposed coating transition metal dichalcogenides, such as molybdenum disulfide (MoS_2) (Srivastava *et al.*, 2017) and tungsten diselenide (WSe_2) (Hu *et al.*, 2020a), on metamaterial resonant devices, as shown in Fig. 1.15. These modulators achieved a modulation depth of 100% at 0.82 THz (Srivastava *et al.*, 2017) and 43% at 0.78 THz (Hu *et al.*, 2020a) under optical pump fluences of 254 and 800 μJ cm^{-2}, respectively. However, these devices share a similar concern with semiconductors, involving the requirement for high optical pump power.

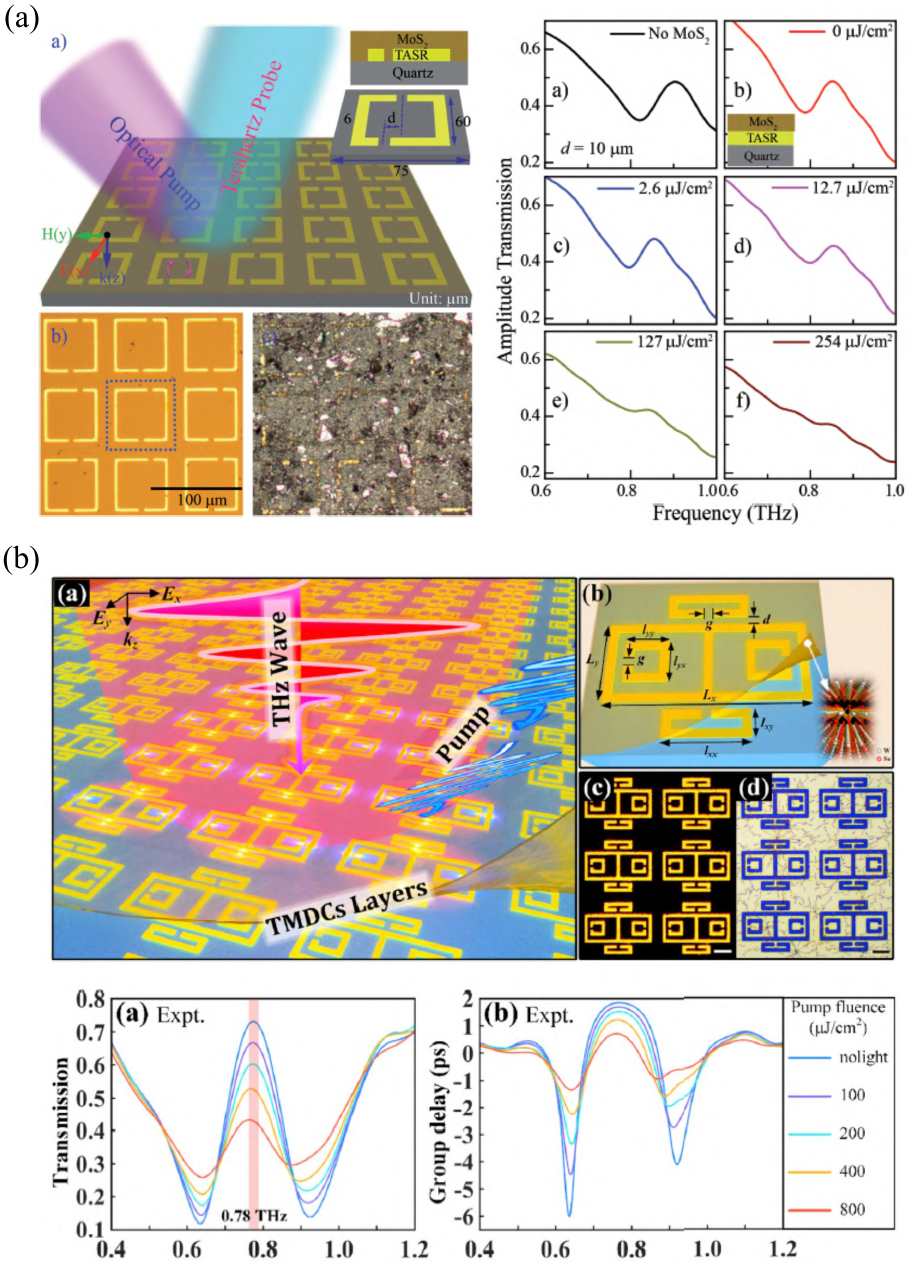

Figure 1.15. Optically tunable terahertz modulators based on 2D materials. (a) Ultrafast switching and modulation of the Fano resonances in MoS_2-coated metamaterials. Adopted from Srivastava *et al.* (2017), and (b) ultrafast switching and amplitude modulation based on WSe_2-functionalised metaphotonic devices. Adopted from Hu *et al.* (2020a).

1.5.2 Electrical tuning

Electrical tuning of terahertz devices offers an alternative for the manipulation of terahertz waves. By incorporating materials with tunable properties into designed structures, terahertz modulation can be achieved through electrical tuning. The primary technique involves the use of metamaterials or metasurfaces. The original work on free-space terahertz modulators was conducted based on an active metamaterial (Chen *et al.*, 2006). Applying gate voltages across the Schottky diode formed at the metal-semiconductor interface allowed for alteration of the carrier density within the n-doped GaAs layer, thereby manipulating the terahertz transmission, as illustrated in Fig. 1.16(a). The devices achieved a modultation depth of 50% at 0.72 THz. However, the maximum modulation speed of this device was limited to several kilohertz due to its large capacitance and resistance. With a similar mechanism, as shown in Fig. 1.16(b)–(c), higher modulation depths and speeds were achieved using metagratings (Huang *et al.*, 2016) and nanodisks (Forouzmand *et al.*, 2018).

The study conducted by Ju *et al.* (2011) demonstrated the tunability of the plasmon resonance in a graphene microribbon array by varying the applied gating voltage, as shown in Fig. 1.17(a). Following this study, diverse forms of graphene metastructures have been reported based on nanoresonators (Brar *et al.*, 2013). These plasmonic modulators have achieved tunable plasmon responses by employing gate-controlled mechanisms within the systems, as shown in Fig. 1.17(b). However, the absolute plasmon response of these devices is considerably weak for practical applications. This is due to the fact that graphene has a monolayer structure, resulting in its light interaction being significantly weaker than that of bulk materials. To address this challenge, graphene metasurfaces were introduced by Lee *et al.* (2012). By combining a graphene monolayer with an electric metasurface comprised of a hexagonal array of metal patches, as depicted in Fig. 1.18(a), efficient tuning of the entire resonance structures can be

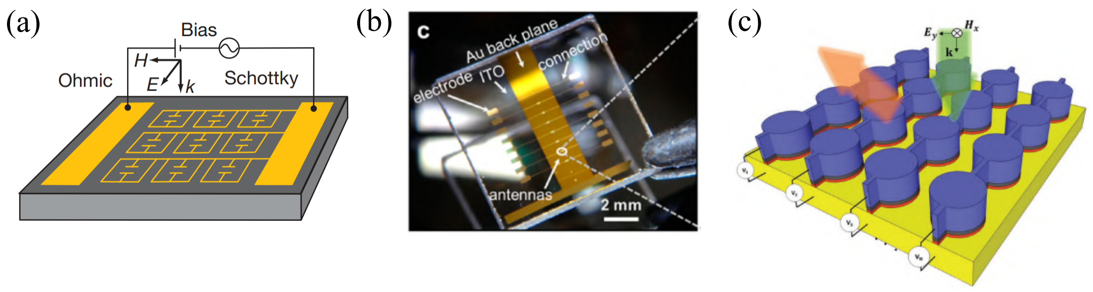

Figure 1.16. Electrically tunable terahertz modulators based on metamaterials. (a) Free-space modulator. Adopted from Chen *et al.* (2006), (b) gate-tunable conducting oxide metasurfaces. Adopted from Huang *et al.* (2016), and (c) optically active reflective metasurface with tunable phase modulator. Adopted from Forouzmand *et al.* (2018).

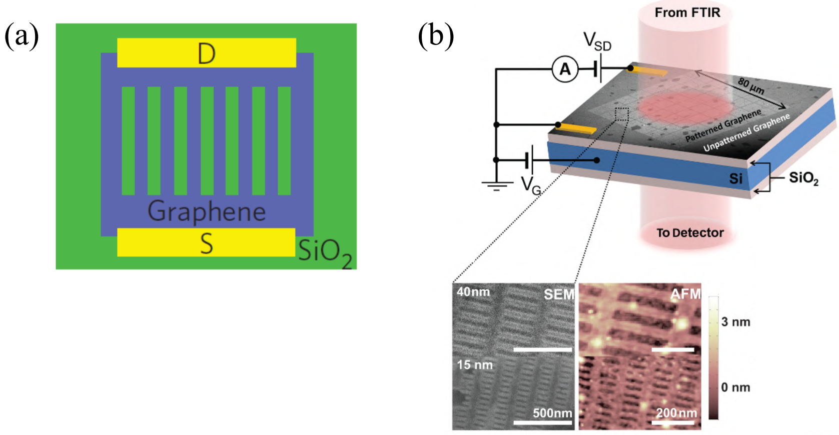

Figure 1.17. Electrically tunable terahertz metamaterials based on graphene plasmonics. (a) Graphene microribbon array. Adopted from Ju *et al.* (2011), and (b) graphene nanoresonators. Adopted from Brar *et al.* (2013).

achieved. This led to a modulation amplitude of 47% and a modulation phase of 32.2° at 0.86 THz. Inspired by this work, numerous studies have been conducted to achieve various features with graphene-based metasurfaces. These include the development of amplitude modulators (Kim *et al.*, 2018) and phase modulators (Dabidian *et al.*, 2016), as illustrated in Fig. 1.18(b)–(c), respectively. Nevertheless, these graphene metasurfaces had a restricted bandwidth and operated in free space, which limits their suitability and compatibility for terahertz integrated systems.

To this end, the integration of tunable graphene-based and a two-dimensional electron gas (2DEG) microstructures into a waveguide have recently been considered as a potential technique integrated systems (Mittendorff *et al.*, 2017; Singh and Sonkusale, 2017). As shown in Fig. 1.19(a), the terahertz modulator incorporated graphene on the silicon rib waveguide. As a result, a modulation depth of 50% was achieved with a speed of 2 kHz via the gate voltage varied between -35 and 35 V (Mittendorff *et al.*, 2017). To enhance modulation depth, a modulator utilising confined terahertz waves within a slot waveguide and a tunable 2DEG to regulate terahertz wave propagation was proposed (Singh and Sonkusale, 2017). As shown in Fig. 1.19(b), such a device achieved a modulation depth of 96% at 0.25 THz with an applied bias voltage of less than 2 V. Inspired by tunable 2DEG-based devices, a recent development demonstrated high-speed modulations using a metamaterial chip integrated into a waveguide (Zhao *et al.*, 2021). The modulation of such a device relies on the conversion of metamaterial resonant modes under applied gate voltages, leading to a modification of the waveguide mode,

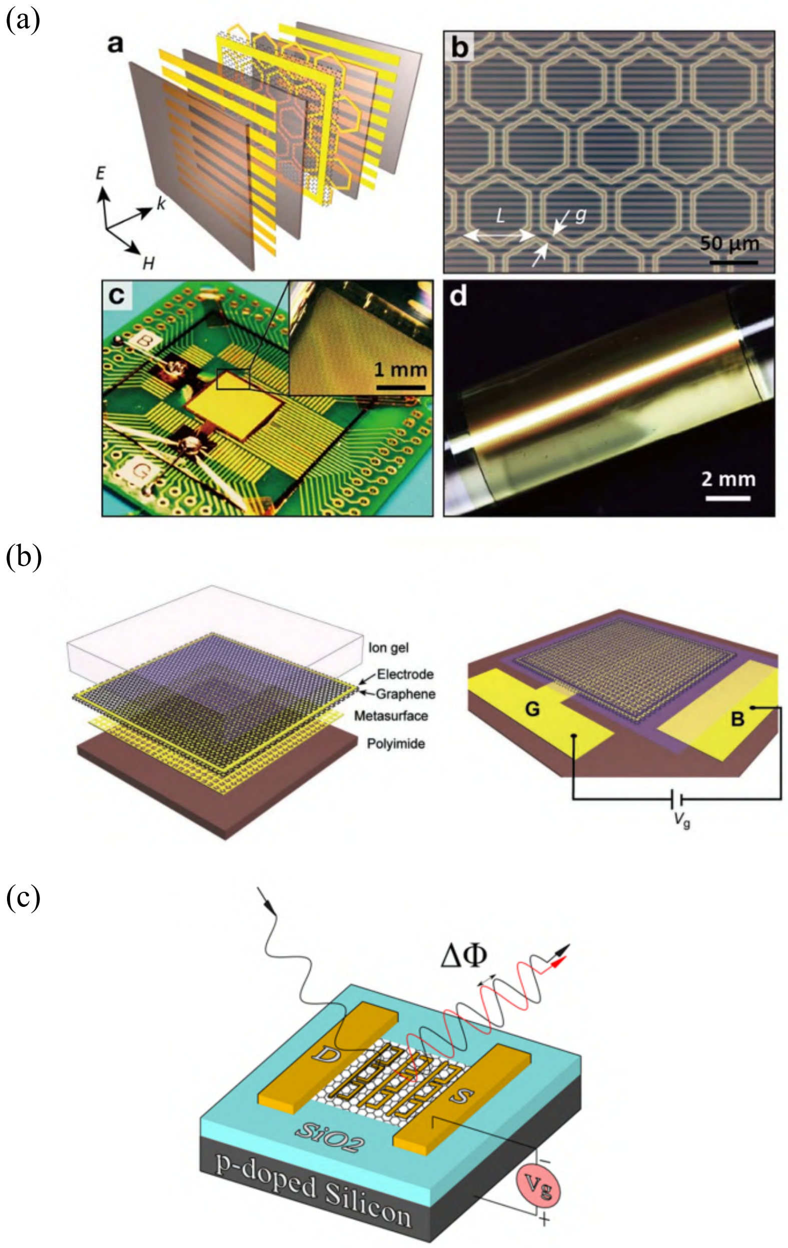
(a)
a
b
E
k
H
L
g
50 µm
c
d
B
G
1 mm
2 mm
(b)
Ion gel
Electrode
Graphene
Metasurface
Polyimide
G
B
V_g
(c)
ΔΦ
D
S
SiO2
p-doped Silicon
Vg
−
+

Figure 1.18. Electrical tuning gate-controlled terahertz metasurfaces. (a) Amplitude and phase modulation based on hexagonal graphene metamaterials. Adopted from Lee *et al.* (2012), (b) amplitude modulators. Adopted from Kim *et al.* (2018), and (c) phase modulators. Adopted from Dabidian *et al.* (2016).

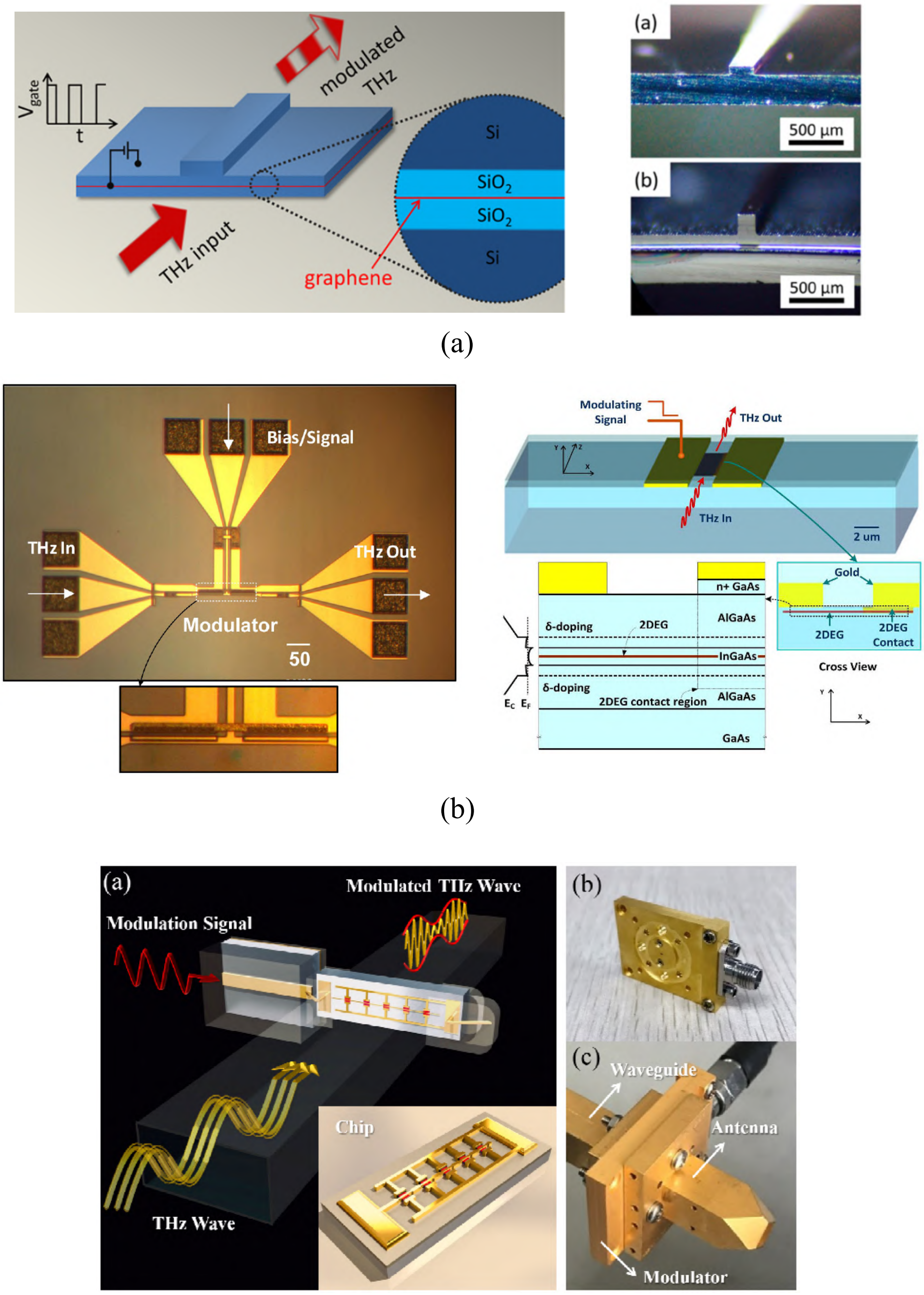
V_gate
t
modulated THz
THz input
Si
SiO₂
SiO₂
Si
graphene
(a)
500 μm
(b)
500 μm
Bias/Signal
THz In
THz Out
Modulator
50
Modulating Signal
THz Out
THz In
2 um
Gold
2DEG
2DEG Contact
Cross View
n+ GaAs
δ-doping
2DEG
AlGaAs
InGaAs
δ-doping
2DEG contact region
AlGaAs
GaAs
E_C E_F
(a)
Modulated THz Wave
Modulation Signal
THz Wave
Chip
(b)
(c)
Waveguide
Antenna
Modulator

(a)

(b)

(c)

Figure 1.19. Tunable graphene-based and 2DEG-based guided waves integration via electrical tuning. (a) Graphene-based waveguide-integrated terahertz modulator. Adopted from Mittendorff *et al.* (2017), (b) tunable terahertz slot waveguide. Adopted from Singh and Sonkusale (2017), and (c) terahertz modulator based on the control of metamaterial mode inside a waveguide. Adopted from Zhao *et al.* (2021).

as shown in Fig. 1.19(c). In the experimental demonstration, the resonance frequency was observed to shift from 0.250 THz to 0.353 THz. A modulation depth of up to 13.5 dB was achieved with a speed of up to 8 GHz. However, due to the behaviour of the metal resonators, this device exhibits a narrow bandwidth, which poses limitations for applications requiring broadband performance.

1.6 Thesis outline and original contributions

In this thesis, we present a series of tunable components integrated on the silicon substrateless waveguide platform. This thesis comprises five chapters, with Chapter 1 laying the foundation and providing the motivation and research background, while Chapter 5 presents a comprehensive conclusion and outlook for future directions. The three core chapters include the original research contributions, and brief outlines of these chapters are given in the following:

Chapter 2 introduces a series of integrated disk resonators built into the substrateless silicon waveguide platform to achieve high Q-factor with low radiation and dissipation losses. The effective medium concept provides a degree of freedom to adjust the effective permittivity of the cladding, enabling precise control over the Q-factor. Experimental results verify the ability to control the Q-factor, which is demonstrated up to 9416 at 274.4 GHz. In addition, these resonators show strong tunability of the resonance under moderate optical power. This content of this chapter was published in the 46th International Conference on Infrared, Millimeter and Terahertz Waves (IRMMW-THz) (Dechwechprasit *et al.*, 2021), and in *Optics Letters* (Dechwechprasit *et al.*, 2023a).

Chapter 3 explores the disk resonators as 1-to-N switches integrated into the substrateless silicon waveguide platform. These switches are controlled via photoexcitation using a low-power 658-nm laser focused on the disk resonator, allowing tuning of the resonance and inhibiting coupling into a crossing port. Experimental results demonstrate the low insertion loss of the proposed switch, attributed to the platform's low dissipation. Additionally, a potential application of the proposed switch with a Luneburg lens for implementing terahertz beam control is presented. A part of this chapter was published in the 47th International Conference on Infrared, Millimeter and Terahertz Waves (IRMMW-THz) (Dechwechprasit *et al.*, 2022), and in *Optica* (Dechwechprasit *et al.*, 2023b).

Chapter 4 introduces an integrated photonic crystal cavity into the substrateless silicon waveguide platform, with a dipole resonator placed in the middle of the cavity to implement a terahertz modulator. The integrated photonic crystal cavity enhances the interaction between photoexcited carriers and terahertz waves, while the dipole resonator further reduces the optical power required to modulate terahertz signals. Experimental results showcase the device's ability to achieve a modulation depth of 5.7 dB with a minimum insertion loss of 1.9 dB. A publication is under preparation.

Note: I am an author of all publications in this thesis, responsible for designing the devices, performing the measurements, analysing the results, and writing the reports.

Chapter 2

Terahertz disk resonator on substrateless waveguide platform

RESONANT cavities are fundamental to and versatile for terahertz integrated systems. So far, integrated resonant cavities have been implemented in relatively lossy terahertz platforms. This chapter presents a series of integrated disk resonators built into a low-loss substrateless silicon waveguide platform, where the resonances and associated Q-factor can be controlled via effective medium. The measurement results demonstrate that the Q-factor can reach up to 9146 at 274.4 GHz due to the low dissipation of the platform. Additionally, these resonators show strong tunability of the resonance under moderate optical power. These terahertz integrated disk resonators can be employed in sensing and communications.

2.1 Introduction

An all-silicon substrateless waveguide platform based on effective medium is a promising candidate for accommodating diverse active (Yu *et al.*, 2019a; Iwamatsu *et al.*, 2023) and passive components that collectively form terahertz integrated systems (Gao *et al.*, 2019). Potentially, a disk resonator can be integrated with this substrateless platform to induce resonance modes at specific frequencies. The performance of these integrated disk resonators is governed by evanescent coupling with an access waveguide and losses in the system. Recently, various terahertz resonant cavities were demonstrated, such as teflon ring resonators (Yuan *et al.*, 2019), silicon sphere resonators (Vogt and Leonhardt, 2017; Vogt *et al.*, 2018, 2019), disk cavities (Xie *et al.*, 2018), photonic crystal cavities (Yee and Sherwin, 2009; Hanham *et al.*, 2017; Yu *et al.*, 2018; Zhao *et al.*, 2022), topological cavities (Kumar *et al.*, 2022b), or microsphere and disk resonators (Vogt *et al.*, 2020; Vogt, 2022; Suresh *et al.*, 2023), and silicon ring resonator (Wang *et al.*, 2019). However, many of those resonators were not integrated but operated in free space and had a large volume compared to the operation wavelength (Yuan *et al.*, 2019; Vogt and Leonhardt, 2017; Vogt *et al.*, 2018, 2019, 2020; Vogt, 2022; Suresh *et al.*, 2023). This caused limits in the designability and portability. In contrast, in the case of integrated resonator structures (Xie *et al.*, 2018; Hanham *et al.*, 2017; Yu *et al.*, 2018; Zhao *et al.*, 2022; Kumar *et al.*, 2022b; Yee and Sherwin, 2009; Wang *et al.*, 2019), the Q-factors were limited by additional losses from the lossy substrates (Xie *et al.*, 2018), coupling and radiation losses (Hanham *et al.*, 2017; Yu *et al.*, 2018; Zhao *et al.*, 2022; Kumar *et al.*, 2022b; Yee and Sherwin, 2009; Wang *et al.*, 2019).

In this chapter, we present two different designs of disk resonators monolithically integrated with the substrateless dielectric waveguide platform. The resonators are held in place by an effective medium cladding that can be fine-tuned to alter the resonance Q factor. When this cladding is partially removed, a relatively high Q factor can be achieved from this platform. We also demonstrate that the resonance can be turned off under photoexcitation, leading to a low insertion loss of the waveguide. In the following, firstly the design and working principle of these disk resonators are described in Section 2.2. Section 2.3 presents the fabrication and measurement processes. Section 2.4 explains the measurement results with existing high-Q disk resonators. In Section 2.5, the photoconductive tuning of the resonance is demonstrated. Section 2.6 is the conclusion.

2.2 Design principles

As shown in Figs. 2.1(a)–(b), the proposed integrated terahertz disk resonator can be monolithically defined on the substrateless waveguide platform. The platform is made solely from high-resistivity silicon with a relative permittivity ϵ_{Si} of 11.68 and a loss tangent of 3×10^{-5} (Gao *et al.*, 2020). These resonators are designed to operate in the E_{11}^{x} mode with an in-plane polarisation. The structures are optimised with CST Microwave Studio 2021. In Fig. 2.1(a), the waveguide and the disk resonator are cladded by an effective medium. The cladding is partially removed for the disk in Fig. 2.1(b), but the effective medium remains between the disk and the waveguide for structural integrity, while the feasibility of the structure is enabled by the supporting frame (Headland *et al.*, 2020). Table 2.1 shows the design parameters of these proposed disk resonators. Clad Disks A and B are designed to exhibit the same resonance order around 274 and 276 GHz by tuning the disk radius r defined in Fig. 2.1(c). These first two disk resonators are to demonstrate controllability of the Q-factor via the effective medium, while the Unclad Disk resonator is designed with a larger disk diameter and most cladding removed to demonstrate a high-Q factor achievable with this design concept. The effective medium cladding is realised by periodically perforating the silicon slab with cylindrical air holes in a hexagonal lattice configuration. The period a is much smaller than the guided

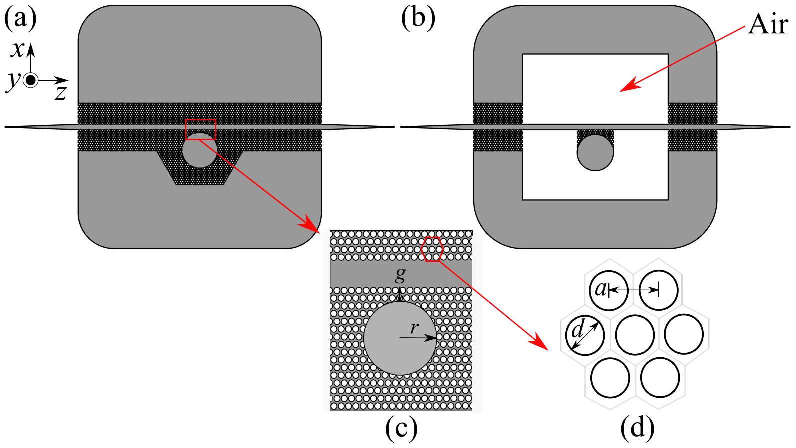

Figure 2.1. Integrated high-Q terahertz disk resonators on substrateless dielectric waveguide platform. (a) Effective-medium-clad disk design. (b) Unclad Disk design. (c) Coupling region of disk resonator with a radius r, and a separation g from the waveguide. (d) Hexagonal lattice of the effective medium cladding with perforation period a of 100 μm and an air hole diameter d of 90 μm. The unperforated silicon slab is for handling purposes, while the external tapers are for mode transition between the sample and the feeding hollow waveguides in measurements.

Table 2.1. Relative permittivity and dimensions for different designs.

	Perforation period	Hole diameter	Disk radius	Separation	Effective relative permittivity	Resonance order
	a (μm)	d (μm)	r (μm)	g (μm)	$(\epsilon_x = \epsilon_z, \epsilon_y)$	M
Clad Disk A	100	85	727	85	3.37, 4.68	9
Clad Disk B	100	90	737	108	2.75, 3.84	9
Unclad Disk	100	93	2000	180	2.38, 3.30	25

wavelength to avoid photonic bandgap effects. This cladding allows wave confinement in the solid core through total internal reflection. The particular waveguide realisation considered here has a width of 225 μm and a thickness of 250 μm. The separation g between the waveguide and the disk is adjusted towards critical coupling (Darmawan and Chin, 2006).

The Q-factor and coupling strength of these resonators can be controlled by changing the effective permittivity tensor of the cladding. The homogenised relative permittivity of the effective medium can be obtained using Maxwell-Garnett effective medium theory (Choy, 2015). These relative permittivities can be expressed as follow:

$$\epsilon_x = \epsilon_z = \epsilon_{\mathrm{Si}} \frac{(\epsilon_0 + \epsilon_{\mathrm{Si}}) + (\epsilon_0 - \epsilon_{\mathrm{Si}})\zeta}{(\epsilon_0 + \epsilon_{\mathrm{Si}}) - (\epsilon_0 - \epsilon_{\mathrm{Si}})\zeta} , \tag{2.1}$$

$$\epsilon_y = \epsilon_{\mathrm{Si}} + (\epsilon_0 - \epsilon_{\mathrm{Si}})\zeta , \tag{2.2}$$

where ϵ_0 and ϵ_{Si} are the relative permittivity of the air and silicon, respectively, while ζ represents the fill factor of the air volume in silicon. For a hexagonal lattice, the fill factor can be calculated as $(\pi d^2)/(2\sqrt{3}a^2)$, where d is the air hole diameter and a is the period of the lattice as shown in Fig. 2.1(d). The homogenised relative permittivities are shown in Table 2.1. By changing the effective permittivity of this platform, the coupling strength between the disk resonator and core waveguide is changed. Specifically, a low relative permittivity of the claddings results in extended evanescent waves and thus enhanced coupling strength between the waveguide and the disk, and the energy is well trapped within the disk which results in low radiation loss and a high Q factor. In contrast, a higher relative permittivity of the claddings leads to higher radiation loss and weak coupling strength of the disk resonator. This leads to a decrease in the Q factor. The customisable cladding permittivity, therefore, adds a degree of freedom in designing resonators for different purposes.

2.3 Fabrication and measurement

To validate the concept, the designs in Table 2.1 are fabricated by photolithography, and dry etching processes as shown in Fig. 2.2. Firstly, a 2.4 µm thick silicon dioxide (SiO_2) layer is grown on both sides of a double sided polished, 250 µm thick, 4-inch intrinsic silicon wafer with resistivity $>$10 kΩ-cm and $< 100 >$ orientation (Wet/Dry Thermal Oxidation Furnace - CTR125 - Expertech). The waveguide layout is transferred on both sides of the SiO_2 coated silicon wafer by a maskless photolithography process (MLA150 Maskless Aligner - Heidelberg Instruments) followed by dry etching of SiO_2. In order to etch through the 250 µm thick silicon wafer with such high aspect ratio, we etched from both sides of the patterned wafer. A specialised Oxford recipe dedicated for high etching rate of about 2.5 µm /min is employed using Inductive coupled plasma deep reactive ion etching (ICP-DRIE) (Deep Silicon Etching - PlasmaPro 100 Estrelas - Oxford). Finally, the residual photoresist and the SiO_2 mask are stripped off by Piranha and HF etch, respectively.

The measurements are conducted using a Keysight vector network analyser with VDI WR-3.4 extension modules spanning 220–330 GHz. As shown in Fig. 2.3, the samples under test are fed by straight WR-3 hollow flangeless waveguides with inserted tapered ends for the measurement of transmission coefficients, $|S_{21}|$. During the measurement, the samples are fixed onto the holder at the unperforated silicon slab. Evaluation of the transmission coefficient requires a reference measurement for normalisation. In this regard, we have also fabricated on the same wafer a series of straight reference waveguides with similar cladding configurations as the proposed designs in Table 2.1 in the absence of the disk resonator, as shown in Fig. 2.2(d).

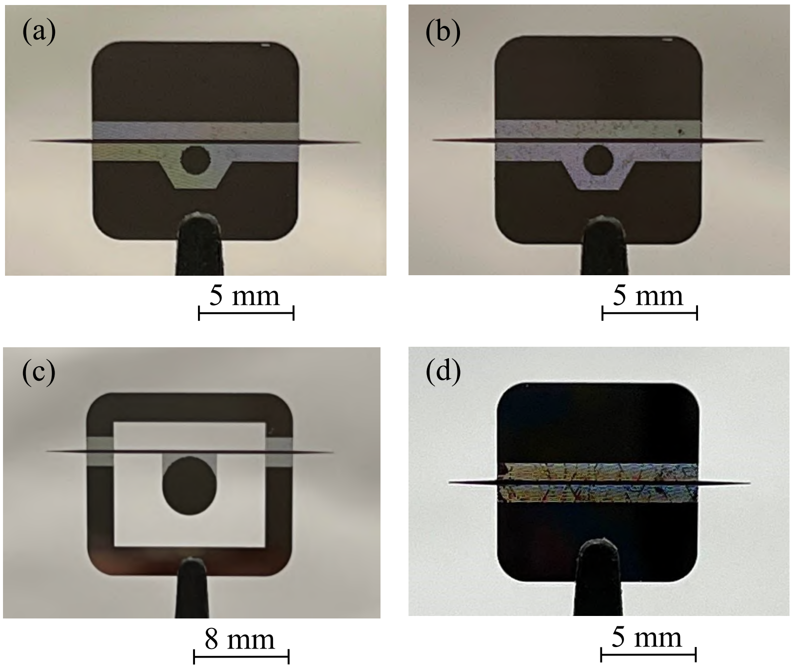

Figure 2.2. Fabricated samples. (a)-(b) Clad Disks A and B. (c) Unclad Disk resonator. (d) Straight waveguide as a reference.

2.4 Results and Discussion

Figure 2.4 shows the measured normalised transmission profiles $|S_{21}|$ of Clad Disks A, B, and Unclad Disk resonator. A Q-factor is extracted from the fitted model in Eq. (2.3) and determined based on the 3-dB bandwidth as follows: $Q = f_r/\Delta f_{\mathrm{3dB}}$, where f_r is the resonance frequency and Δf_{3dB} is the 3-dB bandwidth transmission. As shown in Fig. 2.4, the transmission profiles indicate a resonance behaviour associated with

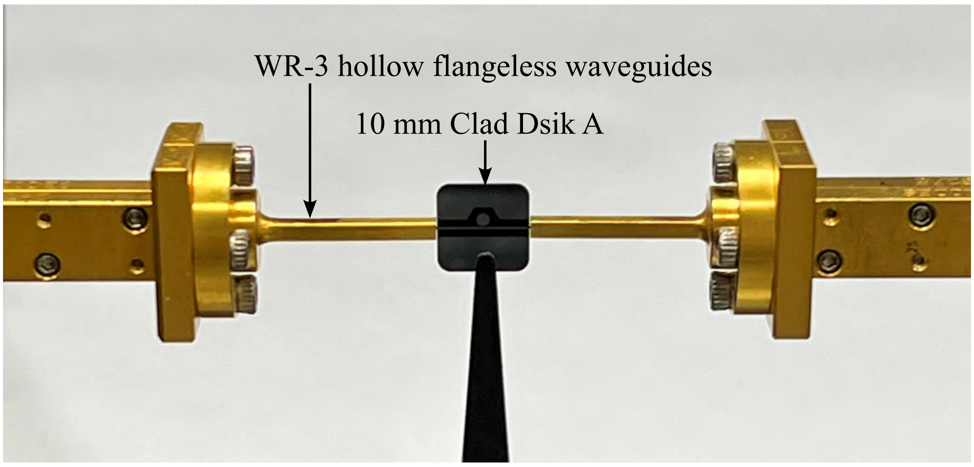

Figure 2.3. Measurement setup with a fabricated Clad Disk A.

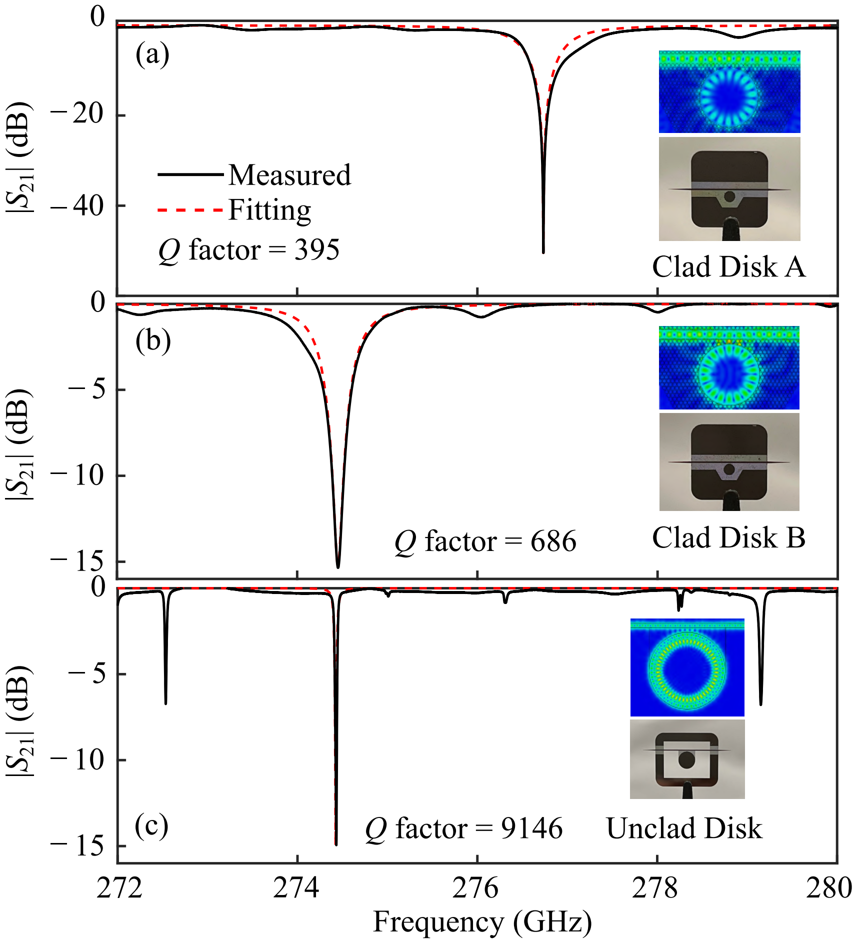

Figure 2.4. Measured normalised transmission profiles of all samples. Q-factors are extracted from the fitted model from Eq. (2.3). (a)-(b) Clad Disks A, B. (c) Unclad Disk resonator. The insets show the resonance modes and fabricated samples.

confined energy in the disk resonators. Clad Disks A and B show that changing the effective permittivity tensor of the claddings allows for controlling the coupling strength and the Q-factor. The measured results of Clad Disks A and B indicate that higher Q-factor are achieved with lower relative permittivity of the cladding. On the other hand, Unclad Disk resonator shows the highest Q-factor due to a larger disk radius and a stronger contrast between the disk and the surrounding that lower the radiation loss. This unclad version can achieve high Q-factors of up to 9146 at a frequency of 274.4 GHz. Additionally, the intrinsic Q-factors of these designs are calculated using an eigenmode analysis in CST Microwave Studio. The intrinsic Q-factor is determined as a function of the disk radius and primarily accounts for the radiation and dissipation losses of the disk itself without the presence of the coupling waveguide. The simulation results yielded intrinsic Q-factors of 795, 1832, and 11930 for each respective design.

To further evaluate the experimental data, coupled mode theory (Okamoto, 2021) is applied here to analyse the exchange of power between the waveguide and the resonator. According to the coupled mode theory, the complex response of a resonance system can be expressed as follows:

$$H(\theta) = \frac{\tau - \alpha e^{-i\theta}}{1 - \alpha\tau e^{-i\theta}}, \tag{2.3}$$

where τ is the coupling between the disk resonator and the waveguide, α is the round-trip loss factor, and θ is the round-trip phase shift. When $\alpha = \tau$, the transmission is zero at the resonance, i.e. $\theta = 0$, and this condition is called critical coupling. For $\alpha < \tau$, the resonator is undercoupled, while if $\alpha > \tau$, the resonator is overcoupled.

In general, the measured amplitude and phase align well with the theoretical model as shown in Fig. 2.5. The model confirms that Clad Disks A, B, and Unclad Disk resonator are near to the critical coupling, i.e., $\alpha \approx \tau$. Those α and τ that are extracted from Fig. 2.5 indicate that the effective-medium cladding can effectively control the coupling transmission τ and internal loss α parameters.

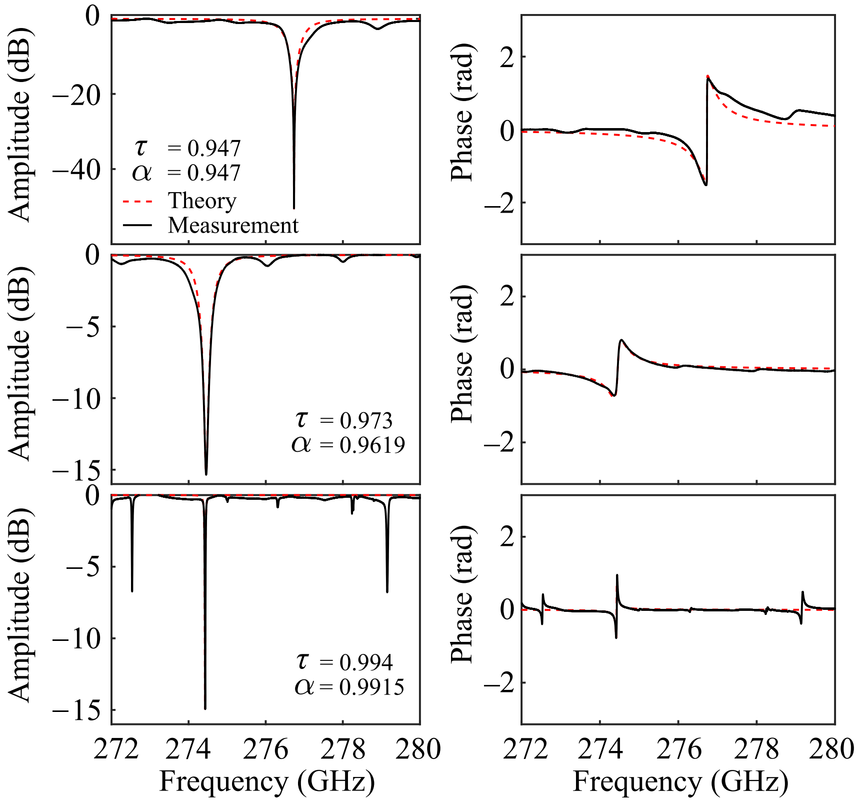

Figure 2.5. Normalised transmission amplitude and phase profiles of Clad Disks A, B, and Unclad Disk. The dashed lines are theoretical fits obtained from Eq. (2.3).

For other integrated resonators (Xie *et al.*, 2018; Hanham *et al.*, 2017; Yu *et al.*, 2018; Zhao *et al.*, 2022; Kumar *et al.*, 2022b; Yee and Sherwin, 2009; Wang *et al.*, 2019), the additional losses from the lossy substrate, coupling loss, and radiation loss limit the Q-factors. Those other disk resonators can achieve a high Q-factor by dramatically increasing the diameter to decrease the radiation loss or adjusting the thickness of the disk resonator to reduce the losses from the substrate (Vogt *et al.*, 2020; Xie *et al.*, 2018). In contrast, some other high-Q terahertz spherical and disk resonators are not integrated structures and operated in free space (Yuan *et al.*, 2019; Vogt and Leonhardt, 2017; Vogt *et al.*, 2018, 2019; Vogt, 2022; Suresh *et al.*, 2023). These designs have limited degrees of freedom to control the coupling strength and cannot be used in integrated systems. Figure 2.6 compares the Q factors between this work and the existing designs at terahertz frequencies. Our designs show relatively high-Q factors comparable to those of non-integrated resonators.

2.5 Photoconductive tuning of the resonance

Photoconductive tuning of the resonance is demonstrated with Clad Disk B. The measurement system involves an optical train to illuminate the inner edge of the disk

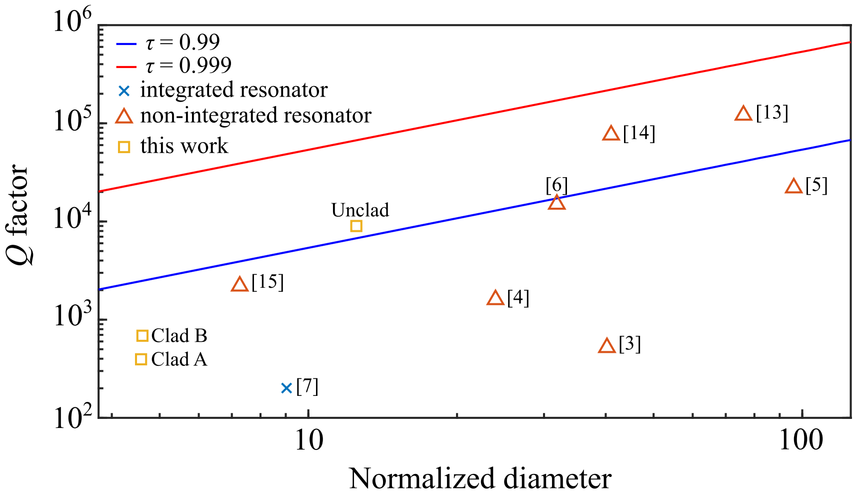

Figure 2.6. Q-factors of the existing spherical resonators, disk resonators, and this work at terahertz frequencies. The normalised diameter is utilised for fair comparison of resonators at different resonance frequencies where $d_{\text{norm}} = dn_m/\lambda_0$, with the disk diameter d, the refractive index of the medium n_m, and free space wavelength λ_0. The coupling baselines between the disk resonator and the waveguide τ, are obtained from (Yariv, 2002) where $Q = \pi n_m^2 d/[(1-\tau^2)\lambda_0]$.

Table 2.2. Parameters for photoexcitation. Measured wavelength (λ), absorption coefficient of silicon (α) (Green and Keevers, 1995), penetration depth ($\delta_p = 1/\alpha$), measured spot size (w_0) at $1/e^2$, power (P), and optical fluence (F).

	λ (nm)	α ($\times 10^3$ cm^{-1})	δ_p (µm)	w_0 (mm)	P (mW)	F (W/m^2)
Red	630	3.27	3.1	1.008	19	23895
Green	535	7.45	1.3	1.096	8	8488
Blue	465	19.1	0.5	2.590	19	3615

resonator as shown in Fig. 2.7. A high-sensitivity CCD line camera, Thorlabs LC100, is used to measure the optical spot size, and the spectrometer is used to measure the wavelength in this configuration. We tune the resonance by using different high-power LEDs, i.e., red, green, and blue. The corresponding wavelengths, the absorption coefficients (Green and Keevers, 1995), the penetration depths, and the measured spot sizes are shown in Table 2.2.

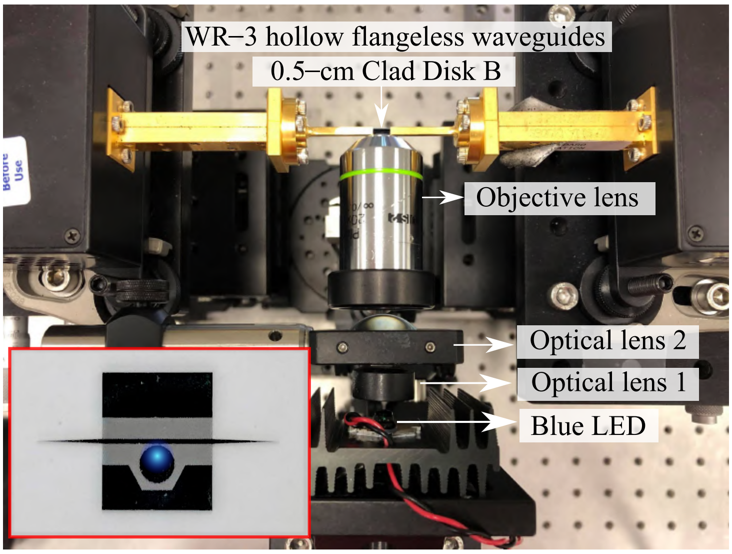

Figure 2.7. Photoexcitation measurement setup. Optical lenses 1 and 2 have focal lengths of 15.0 mm and 25.4 mm, respectively. The objective lens has an effective focal length of 9.0 mm. The inset shows the pumped region.

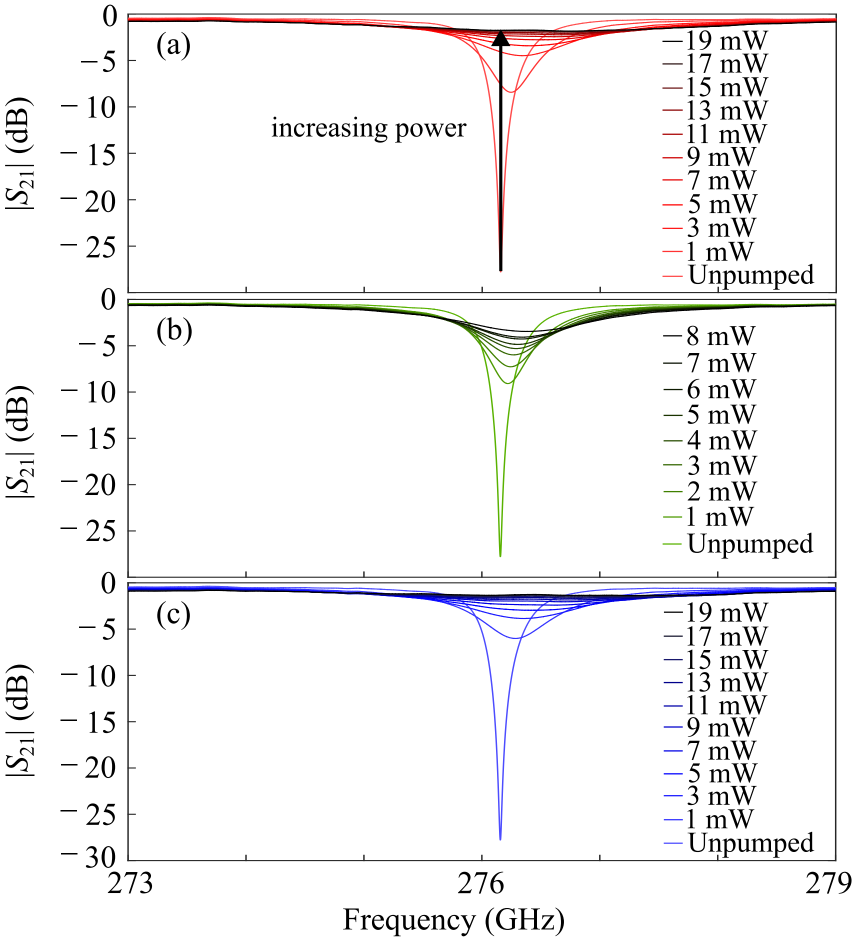

Figure 2.8. Normalised experimental transmission profiles of Clad Disk B under different levels of LED pump power. A straight waveguide is used as a reference for normalisation. (a) Red LED. (b) Green LED. (c) Blue LED.

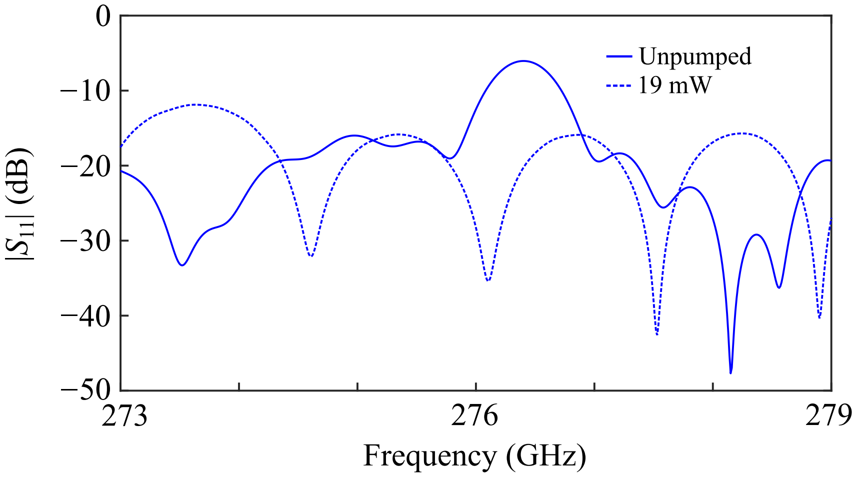

Figure 2.9. Normalised simulated reflection profiles of Clad Disk B under unpumped and 19 mW pump power.

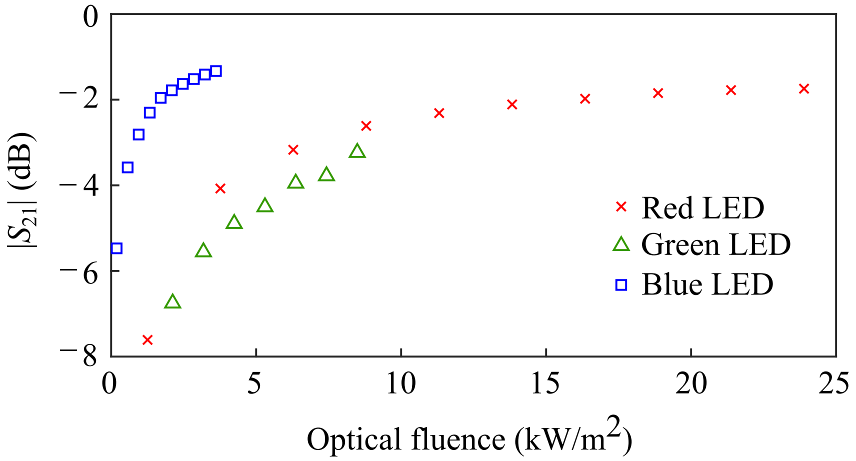

Figure 2.10. Measured transmission level of Clad Disk B on resonance at 276.2 GHz against optical fluence.

Figure 2.8 depicts the normalised transmission profiles of Clad Disk B under different levels of the LED pump power. The maximum transmission is −1.331 dB at 276.2 GHz for the blue LED with 19 mW power, and as such, a 26 dB modulation depth can be achieved. The resonance frequency shift observed in Fig. 2.8 is due to larger absorption at lower frequencies (Heyes *et al.*, 2014), leading to a damping effect on the low-frequency wing of the resonance. The effect manifests as a resonance shift. Furthermore, the index change resulting from thermal variation is negligible during the measurement. In addition, the simulated reflection coefficients show an average return loss of under 10 dB, indicating effective energy trapping within the disk at 276.2 GHz without causing significant reflection in both states, as shown in Fig. 2.9. The normalised transmission coefficient profiles at 276.2 GHz under illumination with different optical fluences are shown in Fig. 2.10. The transmission level gradually increases with an increase in the optical fluence since the optical excitation results in excessive free carriers in silicon. This leads to enhanced conductivity, which dampens the resonance. Blue light is the most effective in modulation due to the higher absorption coefficient and larger spot size as shown in Table 2.2. The experiments clearly demonstrate that an integrated disk resonator yields a strong modulation depth by photoconductive tuning.

2.6 Conclusion

Silicon integrated disk resonators have been realised on the substrateless dielectric waveguide platform. The platform enables a strong resonance behaviour due to the very low absorption of silicon at terahertz frequencies. The experimental results show that changing the relative permittivity of the cladding allows for controlling the radiation loss and thus the Q-factor. An optical excitation results in free carriers in silicon, hence leading to enhanced conductivity that damps the resonance. This proposed integrated terahertz disk resonators can be used as a building block to serve various terahertz applications such as sensing, switching, multiplexing, and modulation. This contributes to a promising pathway for future terahertz integrated systems.

Chapter 3

1-to-N Terahertz Integrated Switches Enabling Multi-beam Antennas

IMPLEMENTING terahertz circuits and system designs relies on integrating reconfigurable devices such as switches, to fulfill a critical role in controlling and manipulating the flow of terahertz signals on the chip. Although there have been several demonstrations of on-off switching in the terahertz range, no demonstrations of 1-to-N switching exist. This pronounced lack of dynamically reconfigurable routing has severely limited the achievable complexity of terahertz systems. To address this, we propose 1-to-N switches made of cascaded disk resonators integrated into a substrateless silicon waveguide platform. A single switch can be controlled via photoexcitation using a low-power 658-nm laser focused onto the disk resonator, turning off the resonance and inhibiting coupling into a crossing port. The measurement results demonstrate that the proposed switch has low insertion loss, which can be attributed to the inherently low dissipation of the platform. The proposed 1-to-2 switch achieves a maximum insertion loss of 1.2 dB, and the maximum extinction ratio of the switch is 16.1 dB with 1.5 GHz of bandwidth. Furthermore, a 1-to-3 switch is monolithically integrated together with a Luneburg lens in order to project each of its output ports to a different far-field direction, and thereby translate the switching operation into a form of reconfigurable beam control for future applications.

3.1 Introduction

In recent years, extensive research has been conducted on terahertz variable attenuators, also known as on-off switches (Hanham *et al.*, 2017; Liu *et al.*, 2022; Kumar *et al.*, 2022a,c; Li *et al.*, 2016; Karimi *et al.*, 2023), that are operated via photoexcitation (Hanham *et al.*, 2017; Liu *et al.*, 2022; Kumar *et al.*, 2022a,c; Li *et al.*, 2016) and short-circuiting (Karimi *et al.*, 2023). Various terahertz variable attenuators have been proposed based on photonic crystal cavities (Hanham *et al.*, 2017), topological photonic waveguides (Liu *et al.*, 2022; Kumar *et al.*, 2022a,c), and hybrid graphene plasmonic waveguides (Li *et al.*, 2016). Some of these attenuators and switches rely on changing the properties of a material through photoexcitation, enabling the control of terahertz wave propagation. These devices only suppress the transmission of terahertz waves and do not facilitate directional switching (Hanham *et al.*, 2017; Liu *et al.*, 2022; Kumar *et al.*, 2022a,c; Li *et al.*, 2016; Karimi *et al.*, 2023). There has been one example of a 1-to-2 switch in the literature, using a T-junction power splitting switch implemented into a parallel-plate waveguide. These switches are operated by electrically actuated liquid metal components to switch between the two output arms of the power splitter (Reichel *et al.*, 2018). However, a parallel-plate waveguide is also an intrinsically multi-mode structure as it supports infinitely many in-plane propagating modes, which is a pronounced disadvantage from the perspective of signal integrity.

In this chapter, we introduce terahertz 1-to-N switches that utilise integrated disk resonators on a substrateless silicon waveguide platform. The switches operate through photoexcitation with visible light, allowing the resonance to be turned off. In Chapter 3, we presented the design and simulation of a 1-to-2 switch based upon photoexcitation (Dechwechprasit *et al.*, 2022), and here we incorporate an additional waveguide coupler that enables guided waves to be routed to one of the two output ports. The performance of this platform relies on the balance between system losses and the evanescent coupling of light with an access waveguide, to achieve what is known as critical coupling (Darmawan and Chin, 2006). An advantage of this scheme is that multiple 1-to-2 switches can be cascaded to realise 1-to-N switches, and we demonstrate this principle with a 1-to-3 switch. In the following, firstly the operation of the proposed integrated terahertz 1-to-2 switch is presented in Section 3.2. Section 3.3 explains the fabrication and measurement processes. The optically controlled routing of the proposed switch is experimentally verified in Section 3.4. In Section 3.5, one possible application of this terahertz switch is demonstrated, where a 1-to-3 switch is monolithically integrated together with an effective medium-based gradient-index Luneburg lens to achieve beam switching.

3.2 Design and principle of operation

As shown in Figs. 3.1(a)–(c), the proposed integrated terahertz 1-to-2 switch can be monolithically defined on a substrateless waveguide platform with a disk resonator in combination with two coupling waveguides. The output ports include the "bar" port or Port 2 and the "cross" port or Port 3, and this switch is designed to operate in the E_{11}^{x} mode with in-plane polarisation. The platform is made solely of high-resistivity silicon with a relative permittivity ϵ_{Si} of 11.68 and a loss tangent of 3×10^{-5} (Dai *et al.*, 2004). The effective medium cladding is defined by periodically perforating the silicon slab with cylindrical air holes in a hexagonal lattice configuration, as shown in Fig. 3.1(c), with the perforation period much smaller than the shortest guided wavelength $\lambda_{\mathrm{g,h}}$ over the operating frequency range. Waveguiding is enabled through total internal reflection, which is facilitated by the contrast in the relative permittivities between the solid core and the cladding. The homogenised relative permittivity of the effective medium can be obtained according to the Maxwell-Garnett effective medium theory (Subashiev and Luryi, 2006; Choy, 2015), yielding ϵ_x, ϵ_y, and ϵ_z of 2.75, 3.84, and 2.75, respectively.

The proposed switch operates by photoexcitation that utilises the optical fluence from a red laser to control the conductivity of the disk at the top surface and the edge far from the waveguides as shown in Fig. 3.1(b). The location is selected to avoid interfering with the terahertz waves propagating along the waveguides. The structure functions as a 1-to-2 switch by using photoexcitation above the bandgap energy of silicon at 1.12 eV, i.e. a wavelength shorter than 1107 nm, to turn on and off the resonance for terahertz waves. Under photoexcitation, photogenerated carriers in silicon can induce changes in permittivity and conductivity. These alterations impact the overall dielectric constant and result in an increased loss tangent of silicon, resulting in an increased absorption of terahertz waves. The switch operates in two states. In the neutral state, with the laser off, waves from Port 1 couple into the disk resonator, resonate and couple out via the second waveguide to Port 3. In the pump state, with the laser on, optical excitation results in excessive free carriers in silicon, leading to enhanced conductivity that affects the cavity resonance and inhibits terahertz resonance coupling to the disk (Dechwechprasit *et al.*, 2022). Consequently, the terahertz wave from Port 1 is transmitted to output Port 2,

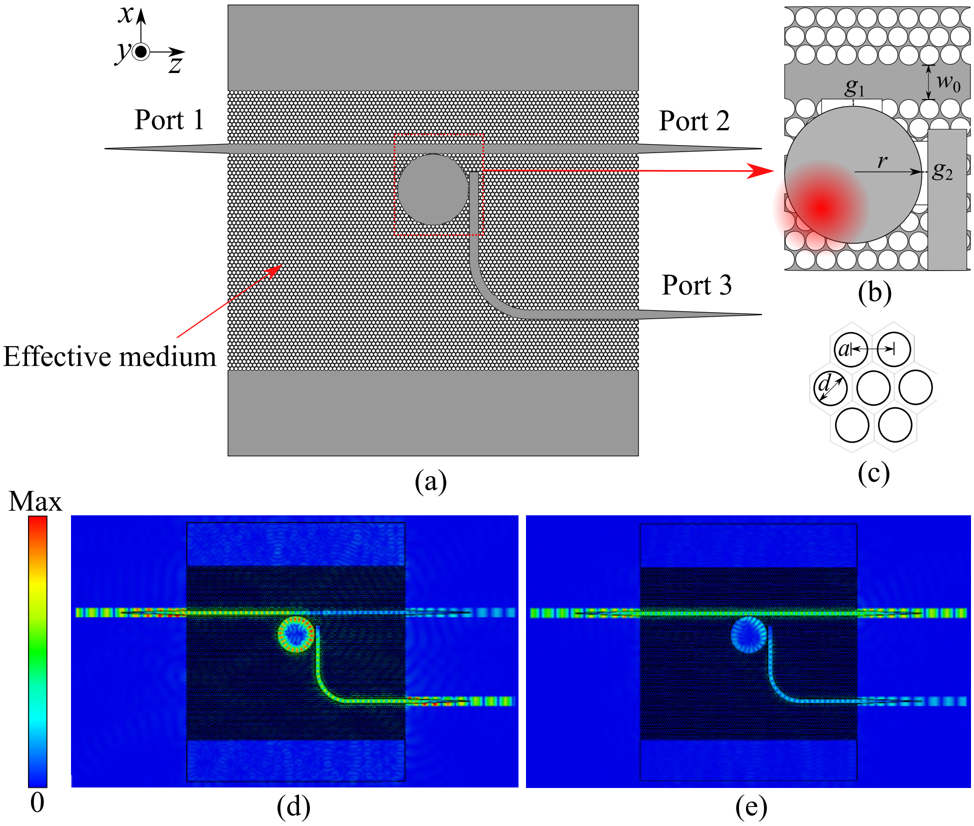

Figure 3.1. Terahertz 1-to-2 switch using an integrated disk resonator on substrateless dielectric waveguide platform. The waveguides with a width w_0 of 225 µm are built into a free-standing wafer with a thickness of 250 µm. (a) Top view, the unperforated silicon slab is for handling purposes, while the taper structures are for mode transition between the sample and the feeding hollow waveguides in measurements. The dimensions of the terahertz 1-to-2 switch are 10 mm in width and length. (b) Coupling region of disk resonator with a radius r of 863 µm and a separation from the waveguide g_1 and g_2 of 20 µm. The red dot is a pumping area of the red laser. (c) Hexagonal lattice of the effective medium cladding with perforation period a of 100 µm and an air hole diameter d of 90 µm. (d) and (e) Simulated instantaneous field distributions are plotted in linear scale at 275 GHz for the neutral and pumped switch resonator, respectively.

while the resonant coupling to Port 3 through the disk is suppressed. To further visualise this concept, the simulated instantaneous field distributions presented in Figs. 3.1(d) and 3.1(e) indicate that the wave transmission channel can be controlled by optical excitation. The operation bandwidth is obviously limited by the bandwidth of the resonator, to be demonstrated in Section 3.3.

In order to investigate the principle of operation of the switch, it is necessary to model the photoexcitation of carriers at the edge of the disk resonator. During optical excitation, when photons with energies greater than the bandgap of the silicon are absorbed, electron-hole pairs are generated, yielding a higher conductivity, i.e., higher absorption of terahertz waves, and damping the Q-factor of the resonance. To model the influence of the optical excitation, we initially calculate the optical fluence F to determine the carrier concentration N_e in the pumped silicon as follows (Sasao and Monnai, 2020):

$$F = \frac{P(1-R)}{A}\,, \tag{3.1}$$

$$N_\mathrm{e} = \frac{F\lambda_\mathrm{laser}}{hc}\,, \tag{3.2}$$

where R is the power reflection coefficient at the air-silicon interface, P is the power spectrum density of the red laser, A is the pumped silicon area, h is Planck's constant, c is the speed of light in vacuum, and λ_laser is the wavelength of the red laser. Next, the plasma frequency ω_p, and collision frequency γ are determined by the carrier concentration N_e and the carrier mobility μ_e, which is related to concentration via an empirical model (Baccarani and Ostoja, 1975), as follows (Heyes *et al.*, 2014):

$$\omega_\mathrm{p} = \sqrt{\frac{N_\mathrm{e}e^2}{\epsilon_0 m_\mathrm{eff}}}\,, \tag{3.3}$$

$$\gamma = \frac{e}{m_\mathrm{eff}\mu_\mathrm{e}}\,, \tag{3.4}$$

where $e = 1.602 \times 10^{-19}$ C is the elementary charge, $\epsilon_0 = 8.854 \times 10^{-12}$ F/m is the vacuum permittivity, and $m_\mathrm{eff} = 0.26m_0$ is the carrier effective mass, with $m_0 = 9.109 \times 10^{-31}$ kg denoting the electron mass. Now the real part of the conductivity $\sigma_\mathrm{r}(\omega)$ can be derived as (Chen *et al.*, 2010):

$$\sigma_\mathrm{r}(\omega) = \frac{\epsilon_0\omega_p^2\gamma}{\omega^2+\gamma^2}\,, \tag{3.5}$$

where ω is the angular frequency. Here, it is assumed that a significant accumulation of photocarriers occurs within the electroabsorption region at high powers, resulting in high absorption, i.e., higher conductivity. Accordingly, the Q-factor of the resonance can be tuned by controlling the real part of the conductivity of silicon under optical excitation as follows (Hanham *et al.*, 2017):

$$Q \approx \frac{\omega\epsilon_0\epsilon_\mathrm{Si}}{\sigma_\mathrm{r}(\omega)\rho}\,, \tag{3.6}$$

where ϵ_Si is the silicon relative permittivity, and ρ is the dielectric filling factor describing the proportion of electric energy stored inside the dielectric material relative to the total electric energy stored in the system.

To validate the switch concept, a 1-to-2 switch is simulated using CST Microwave Studio. In the pump state, the pumped silicon region is represented by a Drude model with the plasma and collision frequencies extracted from Eqs 3.1 and 3.4. The pumped silicon layer can be assumed to be homogeneous with a thickness equal to the penetration depth of the pump laser. In this case, a 658-nm red laser is employed to control the resonance of the disk. At this wavelength, the absorption coefficient (Green and Keevers, 1995), and the penetration depth are 2.70×10^3 cm^{-1} and 3.7 μm, respectively. The pumped area is circular with a diameter of 1.4 mm.

The simulation results for two states are shown in Fig. 3.2(a)–(c). In the neutral state, the transmission from Port 1 to Ports 2 and 3 is -12.3 dB at 275 GHz and -1.2 dB, respectively. This result shows a 3-dB bandwidth terahertz transmission of 1.5 GHz. In contrast, by applying optical excitation onto the disk resonator, the resonance is turned off and the wave is transmitted to Port 2. The normalised transmission coefficient at Port 2 is -0.9 dB, and -17.3 dB at Port 3, as shown in Fig. 3.2(b) and 3.2(c). The extinction ratio between the on/off state at Port 2 and Port 3 is 11.4 dB and 16.1 dB, respectively. In both switching states, the reflection coefficient is around -16.0 dB at 275 GHz, as shown in Fig. 3.2(a) which indicates that the switch does not cause high reflection. The insertion losses in the systems are caused by coupling loss and radiation loss from the disk resonator. The coupling loss is due to the limited coupling region imposed by the fabrication process, while the radiation loss is caused by the curvature of the disk. Therefore, Figure 3.2(b) and (c) show the inhibition of the resonance with optical pump power, which confirms that the Q-factor of the disk resonator is affected by the associated photo-induced high conductivity in the silicon (Dechwechprasit *et al.*, 2023a). In addition, the bandwidth of the on/off switch is related to the Q-factor as follows:

$$Q = \frac{f_r}{\Delta f_{3\mathrm{dB}}}, \tag{3.7}$$

where f_r is the resonance frequency and $\Delta f_{3\mathrm{dB}}$ is the 3-dB bandwidth transmission. A higher Q factor corresponds to a narrower bandwidth, while a lower Q factor results in a wider bandwidth. To achieve a wider bandwidth in this design, cascading disk resonators with the same resonance frequencies can increase the overall bandwidth (Schwelb and Frigyes, 2003). However, it is important to note that each additional disk resonator introduces additional coupling and radiation losses, which in turn result in higher insertion loss.

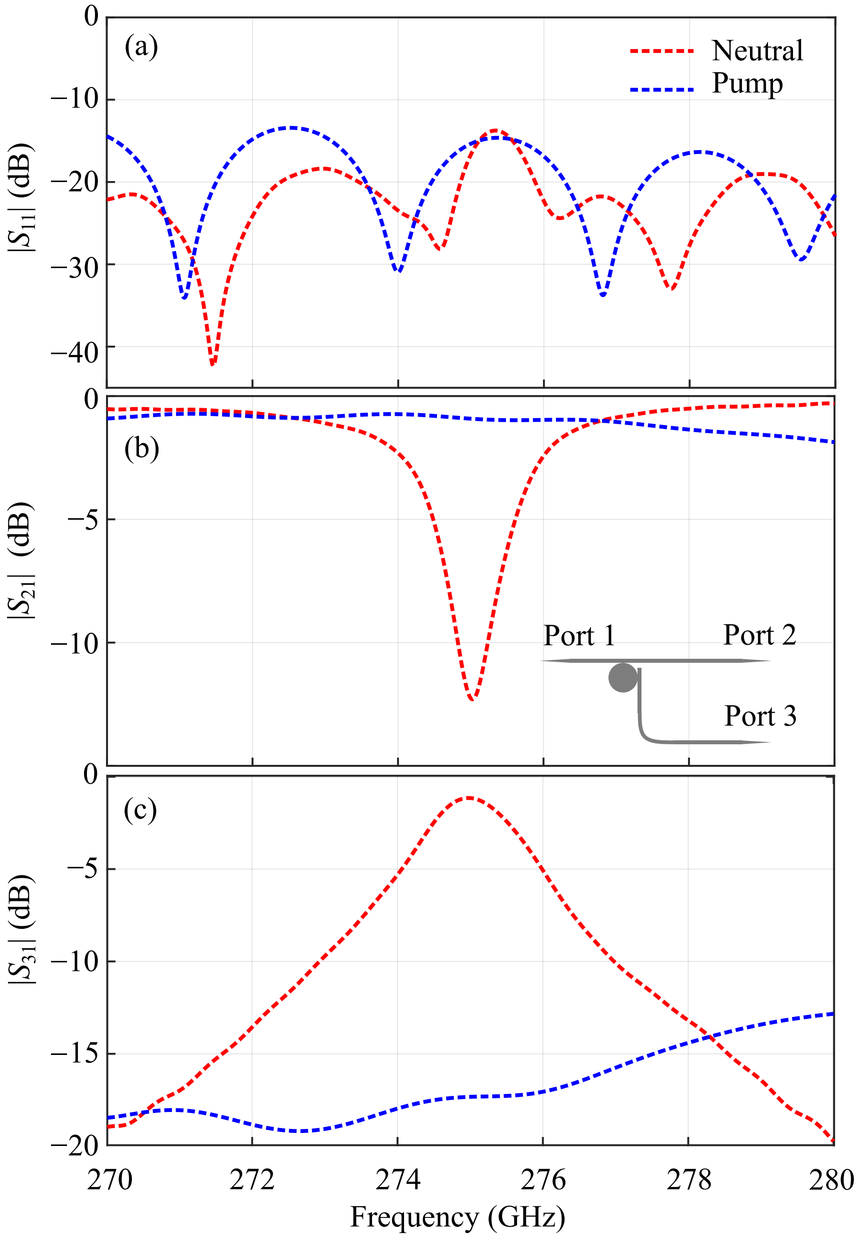

Figure 3.2. Simulated transmission and reflection profiles of the 1-to-2 switch in two states, i.e., neutral and pump state. (a) Reflection coefficients. (b) Transmission between Port 1 and Port 2. (c) Transmission between Port 1 and Port 3. Drude parameters for the photoexcited silicon are $\omega_{\mathrm{p}} = 2\pi(1.6 \times 10^{14})$ rad/s and $\gamma = 2\pi(8.0 \times 10^{12})$ 1/s (Dechwechprasit *et al.*, 2022).

3.3 Fabrication and measurement

To experimentally validate the switch concept, a 1-to-3 switch design has been fabricated as shown in Fig. 3.3(a). The sample is made from a 4-inch intrinsic float-zone silicon wafer with a thickness of 250 µm and a resistivity of >10 kΩ-cm. The fabrication process is similar to that described in Section 2.3. The device has dimensions of 20.8×12.5 mm^2,

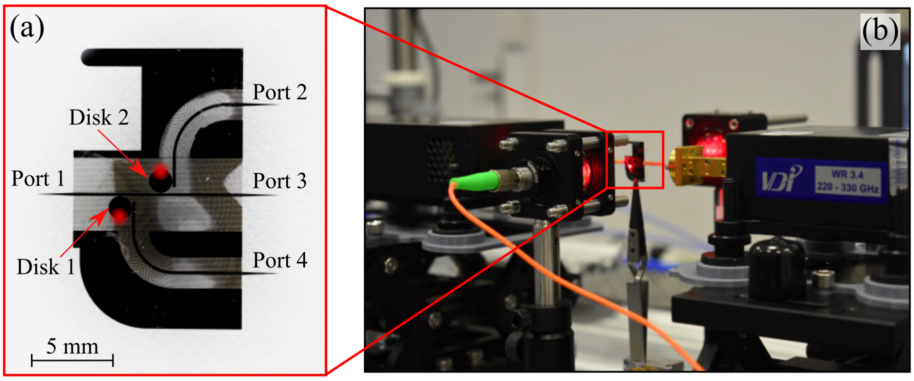

Figure 3.3. Fabricated 1-to-3 switch for the three-channel device and optical excitation measurement setup. (a) Fabricated sample with the pumped region for 1-to-3 switch. (b) Full optical excitation setup. Optical lenses 1 and 2 have focal lengths of 25.4 mm and 30.0 mm, for Disk 1 and Disk 2, respectively. The two fibre collimators have focal lengths of 18.24 mm with a wavelength of 633 nm, and the two red lasers have a centre wavelength of 658 nm.

with a minimum distance of approximately 5 mm between the output ports to accommodate the necessary bending radius and the coupling with a rectangular waveguide during measurement. Furthermore, to prevent crosstalk between the cascaded disk resonators, a minimum clearance between the disks of approximately 1 mm is required. For larger values of the output ports, the area would increase proportionally.

The measurements setup of the 1-to-3 switch are similar to that provided in Section 2.3 for measuring the transmission and reflection coefficients of the sample in each port. The measurements are performed with two ports on the VNA. To demonstrate the switch operation, the measurement system involves an optical train set up to illuminate the edge of the disk resonator as shown in Fig. 3.3(b). A red laser pigtail fibre diode module with a centre wavelength of 658 nm is connected to a fibre collimator with a focal length of 18.24 mm at a wavelength of 633 nm. The collimator is used to collimate the red light from the source to an optical lens 1, which has a focal length of 25.4 mm. The light is focused on the edge of Disk 1 to control the resonance of the disk. For Disk 2, an optical lens 2 with a focal length of 30.0 mm is used. As described in the previous section, switching on the laser damps the resonance and thus the coupling into the coupled port. The $1/e^2$ spot size measured by a Thorlabs LC100 line camera is 1.26 mm. The maximum pump power of the red laser is 40 mW, yielding an average optical fluence of 32000 $\mathrm{W/m^2}$ in its main beam. Furthermore, a reference measurement is acquired for normalisation purposes using a straight waveguide.

3.4 Demonstration of terahertz switches

The operation of the 1-to-3 switch can be described by three operating states, as summarised in Table 3.1. In the neutral states, there is no optical excitation for both resonators. The waves from input Port 1 are coupled into Disk 1 on resonance and coupled out via the second waveguide to Port 4, as shown in the electric-field distribution in Fig. 3.4(a). In the pump states, there are two settings that can be achieved using two optical excitations. In the first pump state, Disk 1 is under optical excitation suppressing transmission from Port 1 to Port 4. As such the waves can be transmitted from Port 1 to Port 2 through Disk 2, as shown in Fig. 3.4(b). In the last state, both resonators are under optical excitation. This results in the waves from Port 1 being transmitted to Port 3 or ”the middle port” because the resonances of the two disk resonators are turned off, as shown in Fig. 3.4(c). Thus, the resonance coupling to Ports 2 and 4 through the first and second disks is suppressed.

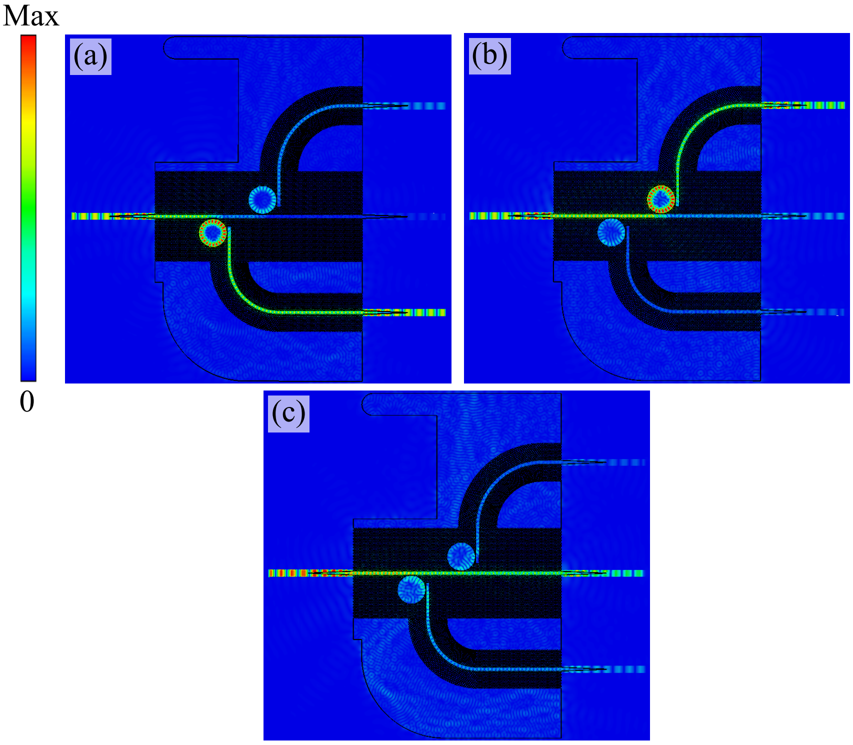

Figure 3.4. Simulated instantaneous field distributions of the 1-to-3 switch for the three-channel device. (a) Both Disks light off. (b) Disk 1 light on, Disk 2 light off. (c) Both Disks light on.

In general, the simulated and measured results presented in Fig. 3.5 agree well. Discrepancies between simulations and measurements can be attributed to several factors,

Table 3.1. Normalised transmission coefficient of the 1-to-3 switch at 276.1 GHz.

	Laser 1	Laser 2	Port 2 (dB)	Port 3 (dB)	Port 4 (dB)
No optical excitation	Off	Off	−13.54	−24.23	−1.78
Disk 1 pumped	On	Off	−3.28	−18.05	−17.37
Both Disks pumped	On	On	−17.02	−2.94	−18.79

including fabrication tolerances and misalignment. These tolerances can result in non-ideal coupling, as previously discussed in the results of the 1-to-2 switch. Discrepancies observed in $|S_{11}|$ are relatively large due to its weak power level. The working resonance frequency of the 1-to-3 switch differs from that of the 1-to-2 switch due to the fabrication tolerance of the disk resonator diameter, which mainly controls the resonant frequency. From the measured results in Fig. 3.5(a)-(l), the normalised transmission coefficient of the 1-to-3 switch at 276.1 GHz is listed in Table 3.1. These results indicate that the energy is effectively coupled to one of the output ports.

Practically, the insertion loss in this system is not only caused by the coupling loss and radiation loss of the disk but also the losses from unavoidable leakage to pumped resonators and non-operating ports. In practical implementation, it is challenging to completely suppress the resonance coupling into the disk resonator under optical excitation. The disk resonators can effectively damp the resonance only after the coupling event. More specifically, the resonator can only exhibit its desired frequency-selective behaviour after coupling thereto has already occurred, which is the origin of the unavoidable increase in insertion loss in the case of a pumped resonator. The leakage to non-operating ports occurs due to the non-ideal coupling of the disk resonator caused by fabrication limitations and tolerances in the separation gap. These can be observed in Fig. 3.4(a)-(c) and are verified by the measurement results, which demonstrate some remaining transmitted power at inactive ports as shown in Fig. 3.5. The switching speed of this 1-to-3 switch depends on the recombination time of photoexcited carriers in the silicon, typically around 1 ms, resulting in a switching speed of approximately 1 kHz (Kannegulla *et al.*, 2015). It is for this reason that we term the device a “switch,” and not a “modulator,” which would require a far higher switching speed. After all, these experimental results verify the proposed 1-to-3 switch concept. Each resonator can

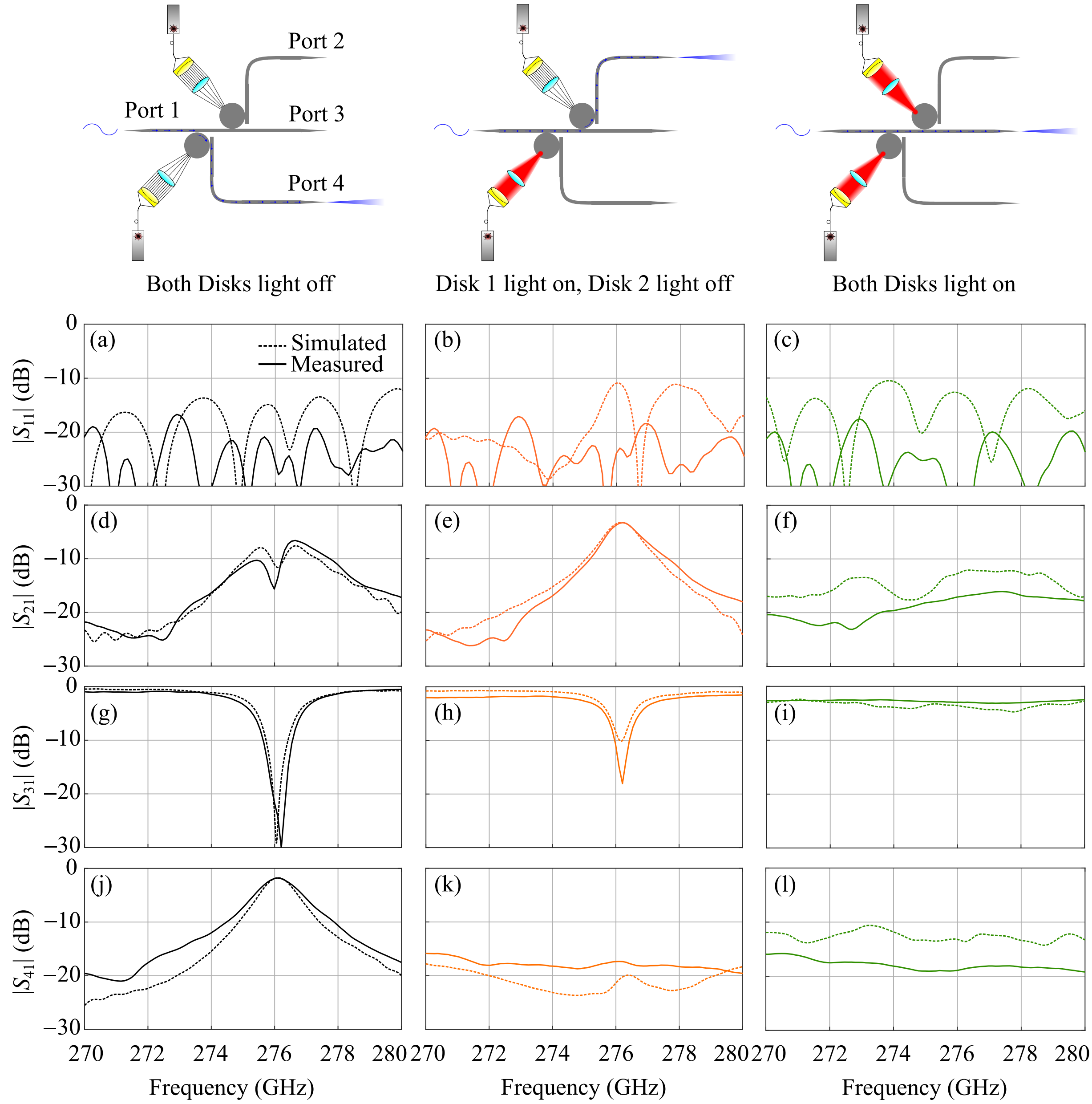

Figure 3.5. Simulated and measured transmission and reflection profiles of the 1-to-3 switch for the three-channel device. (a)–(c) Simulated and measured reflection coefficients of three operating states at Port 1. (d)–(l) Simulated and measured transmission coefficients of three operating states at Port 2, Port 3, and Port 4.

operate individually, enabling independent control of each unit channel. However, it is worth noting that cascading multiple disk resonators leads to increased insertion loss.

3.5 Multi-beam switching with integrated antenna

Here we demonstrate the integration of the 1-to-3 switch with an integrated Luneburg lens to realise discrete beam steering without mechanical actuation. The Luneburg lens is a gradient index (GRIN) structure which maps a point source at the circumference to a far-field direction diametrically opposed to the location of the source. This mapping functionality makes it uniquely suited to realising angular beam-steering so long as the feed point can be adjusted. Previously, an all-silicon Luneburg lens was demonstrated with high gain and efficiency (Headland *et al.*, 2018), but did not incorporate any switching mechanism, and so each far-field direction was accessed by a separate input port. Thus, whilst the multiple feeds were characterised, true beam steering was not demonstrated. Now, with the proposed switches we can perform an illustratory example of beam steering based on this principle.

A detailed procedure for the design of an all-silicon Luneburg lens is outlined in Ref. (Headland *et al.*, 2018), but for completeness, we include a brief overview. To achieve the desired focal mapping, we employ a radially symmetrical modal index profile defined by the equation (Headland *et al.*, 2018),

$$\alpha = n\frac{r}{r_{\max}}\,, \tag{3.8}$$

$$n(\alpha) = \begin{cases} n_0\left(\sqrt{1+\sqrt{1-\alpha^2}}\right)\exp(-\Omega(\alpha))\,, & \text{if } \alpha \leq 1\,, \\ n_0 & \text{if } \alpha > 1\,, \end{cases} \tag{3.9}$$

where

$$\Omega(\alpha) = \frac{2}{\pi}\int_{\frac{1}{n_0}}^{1}\frac{1}{r'}\arctan\left(\sqrt{\frac{1-\alpha^2}{(n_0 r')^2-1}}\right)dr'\,, \tag{3.10}$$

where α is the product of refractive index in a Luneburg lens antenna, n and normalised lens radius, n_0 is the modal index of the slab mode at the circumference, and $r_{\max}$ is the radius of the lens. To realise this profile, the previously described effective medium technique can be used to design the slab modal index at a single frequency by controlling the radius of the holes. For optimal matching, the index at the edge of the lens must be made as low as possible in order to match to free space, and this is why the hole radii are set to their maximum, i.e. 90% of the diameter, as shown in Fig. 3.6(b). The radius of the lens is a free-variable, and depends on the desired realised gain. Here, we set this radius to 5 mm.

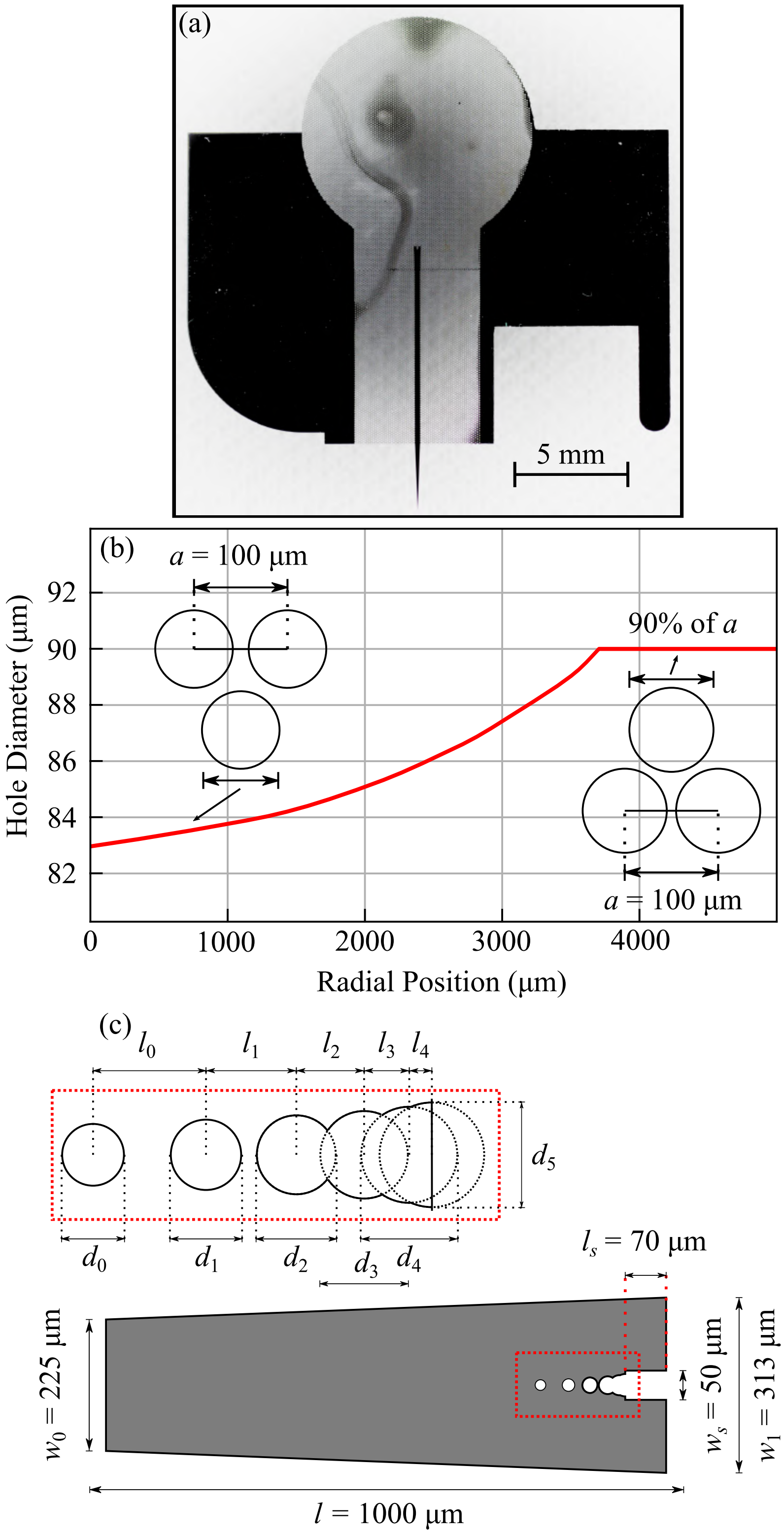
(a)
5 mm
(b)
$a = 100$ µm
90% of a
$a = 100$ µm
Hole Diameter (µm)
82
84
86
88
90
92
0
1000
2000
3000
4000
Radial Position (µm)
(c)
l_0
l_1
l_2
l_3
l_4
d_5
d_0
d_1
d_2
d_3
d_4
$l_s = 70$ µm
$w_0 = 225$ µm
$w_s = 50$ µm
$w_1 = 313$ µm
$l = 1000$ µm

Figure 3.6. Luneburg lens design. (a) Photograph of the fabricated single Luneburg lens for characterisation. (b) Radially dependent hole diameter profile used to realise the all-silicon Luneburg lens. (c) Parametric design of the optimised feed structure. In this case l_i is defined iteratively as $l_i = l_{i-1} + 10$ where $l_0 = 10$ µm and the hole diameter is a linear function varying between 32.8 µm and 48 µm.

In Ref.Headland *et al.* (2018), a tapered waveguide was used to feed the lens. However, this technique has limitations notably it is dispersive. More specifically, the taper reduces confinement, resulting in most of the power being distributed outside the core, occupying a wide area. Consequently, it becomes a poor approximation of a point source, and hence is unsuitable as feed for the Luneburg lens. In Ref.Headland *et al.* (2021a), this was addressed by introducing a compact gradient index feed based on a slot waveguide to feed a half-Maxwell Fisheye lens. This lens is also implemented with effective medium, so its feeding structure can straightforwardly be adapted to the Luneburg lens. Here we utilise this approach to feed the Luneburg lens. In Fig. 3.6(c), the parametric design of the feed is shown, comprised of two components, first a linear widening of the waveguide core, and second, a transition to a slot based on a gradient index transition. This design is then optimised to minimise the magnitude of the reflection coefficient $|S_{11}|$ obtained with a full-wave simulation of the single port Luneburg lens. The final parameters are shown in Fig. 3.6(c).

To characterise this antenna, the Luneburg lens with a single optimised port, shown in Fig. 3.6(a) is used. The sample is packaged inside a 3D-printed polylactic acid (PLA) mount and attached to a rotating stage for radiation pattern measurement. The antenna package is coupled to the WR3.4 waveguide output. The reflection coefficient, shown in Fig. 3.7(a) indicates reasonable alignment with simulations, with return loss far in excess of 10 dB. Then, using a rotating stage, a radiation pattern measurement in the E-plane is conducted and shown in Fig. 3.7(b). Next, another fabricated sample contains the 1-to-3 switch, with the corresponding output ports of the switches connected to 3 feeds surrounding the circumference of the Luneburg lens, giving the possibility for 3 discrete beams, arbitrarily selected at 0, 30, and -60 degrees as shown in Fig. 3.8(a). In theory, this scheme could be extended to many more feeds, though admittedly the optical feeding network becomes increasingly unwieldy. Nevertheless, this challenge can be overcome by employing an optical projector or spatial light modulator. The operation of the switched beam can be described as follows: when Disk 1 is not illuminated, the beam is steered to a 30° angle via Port 4. When Disk 1 is illuminated and Disk 2 is not, the beam is steered to a -60° angle via port 2. Finally, when both Disks 1 and 2 are illuminated, the beam is steered to a 0° angle via Port 3.

The switched-beam antenna is characterised by the experimental setup shown in Fig. 3.8(b). The radiation pattern measurements of the various switched beam states are conducted. The free-standing antenna is held with customised packaging and fed by a

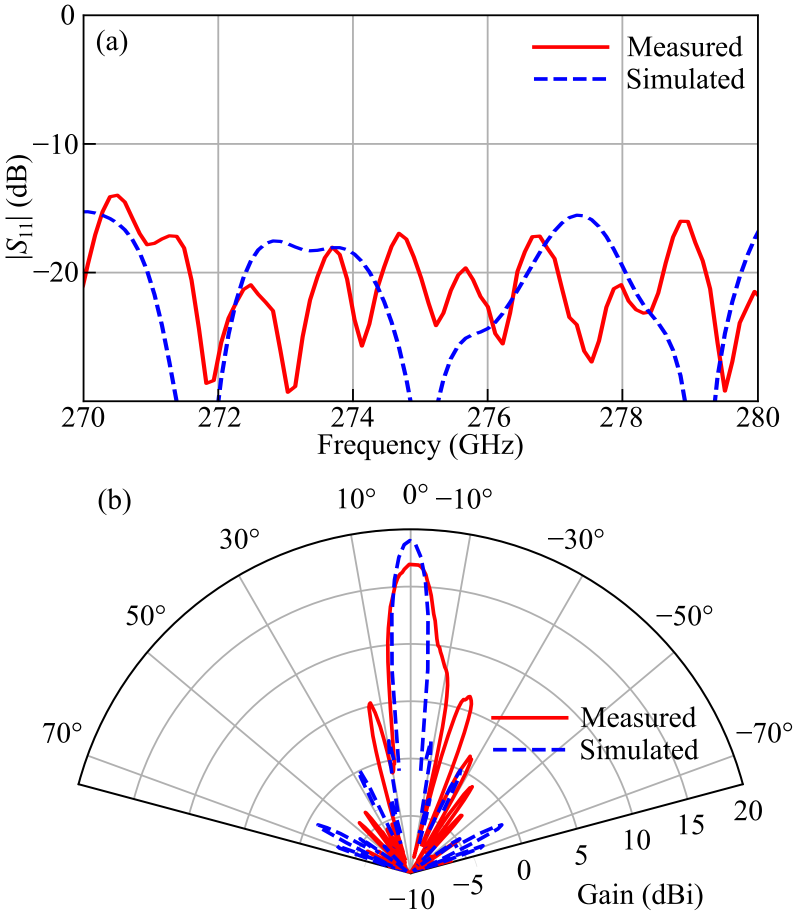

Figure 3.7. Characteristics of the Luneburg lens. (a) Simulated and measured reflection coefficients of the single feed Luneburg lens sample over the frequency range of interest. (b) Simulated and measured gain of the single feed Luneburg lens sample at 276.98 GHz.

straight WR-3 hollow flangeless waveguide. The radiation emitted by the Luneburg lens antenna propagates over a free-space distance of 220 mm, i.e., in the Fraunhofer far-field region, whereupon it is received by a WR-3-coupled diagonal horn antenna. In order to measure radiation patterns, the above process is carried out repeatedly over an angular range extending from −75° to 75° with 0.25° steps on an automated rotation stage. The results of this procedure for the switched beam with a three-port antenna are given in Fig. 3.9. The measured radiation patterns are shown at a working frequency of 276.98 GHz. As illustrated in Fig. 3.9(a)-(f), the measured and simulated beam profiles for both Disks in the neutral states show the expected 30° output Port 4, with a maximum gain of 15.8 dBi. In the case where Disk 1 is pumped, the beam is switched to a −60° angle output Port 2 with a maximum gain of 16 dBi. Finally, pumping both Disks allows to achieve a maximum gain of 14 dBi at 0° angle output Port 3. The results indicate that the radiation efficiency is primarily limited by the efficiency

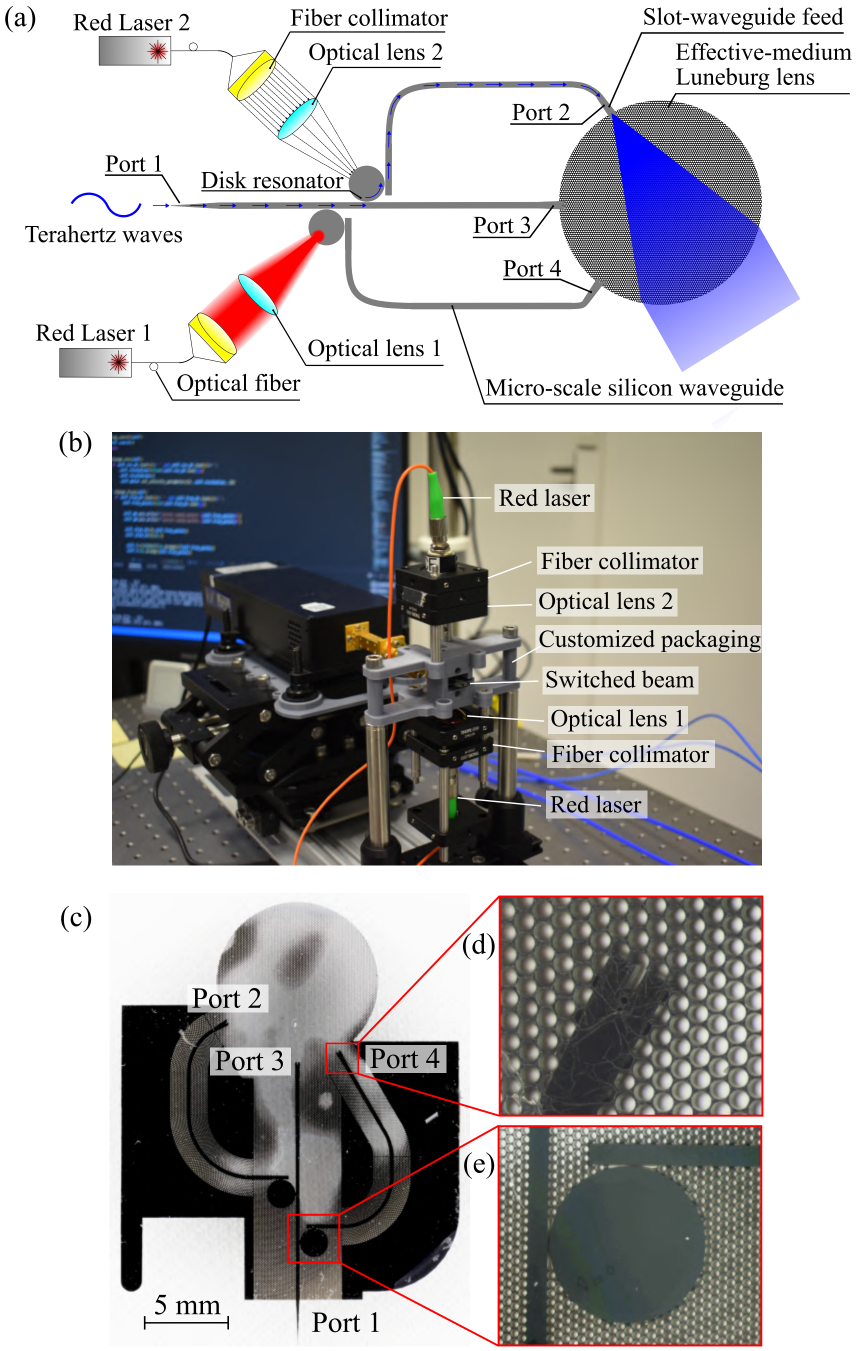
(a)
Red Laser 2
Fiber collimator
Optical lens 2
Slot-waveguide feed
Effective-medium
Luneburg lens
Port 2
Port 1
Disk resonator
Terahertz waves
Port 3
Port 4
Red Laser 1
Optical lens 1
Optical fiber
Micro-scale silicon waveguide
(b)
Red laser
Fiber collimator
Optical lens 2
Customized packaging
Switched beam
Optical lens 1
Fiber collimator
Red laser
(c)
Port 2
Port 3
Port 4
5 mm
Port 1
(d)
(e)

Figure 3.8. Multi-beam switching with the 1-to-3 switch. (a) Schematic illustration of the switched-beam antenna under optical excitation. (b) Photoexcitation measurement setup. Red laser pigtail fibre diode modules have a center wavelength of 658 nm with a maximum power of 40 mW. Optical lenses 1 and 2 have focal lengths of 25.4 mm and 18.24 mm, respectively. The customised packaging is for handling purposes and is not situated in proximity to electromagnetically relevant components. (c) Photograph of the fabricated switched-beam antenna for characterisation. (d) Micrograph of the tapered feed. (e) Micrograph of the disk resonator with access and coupling waveguides.

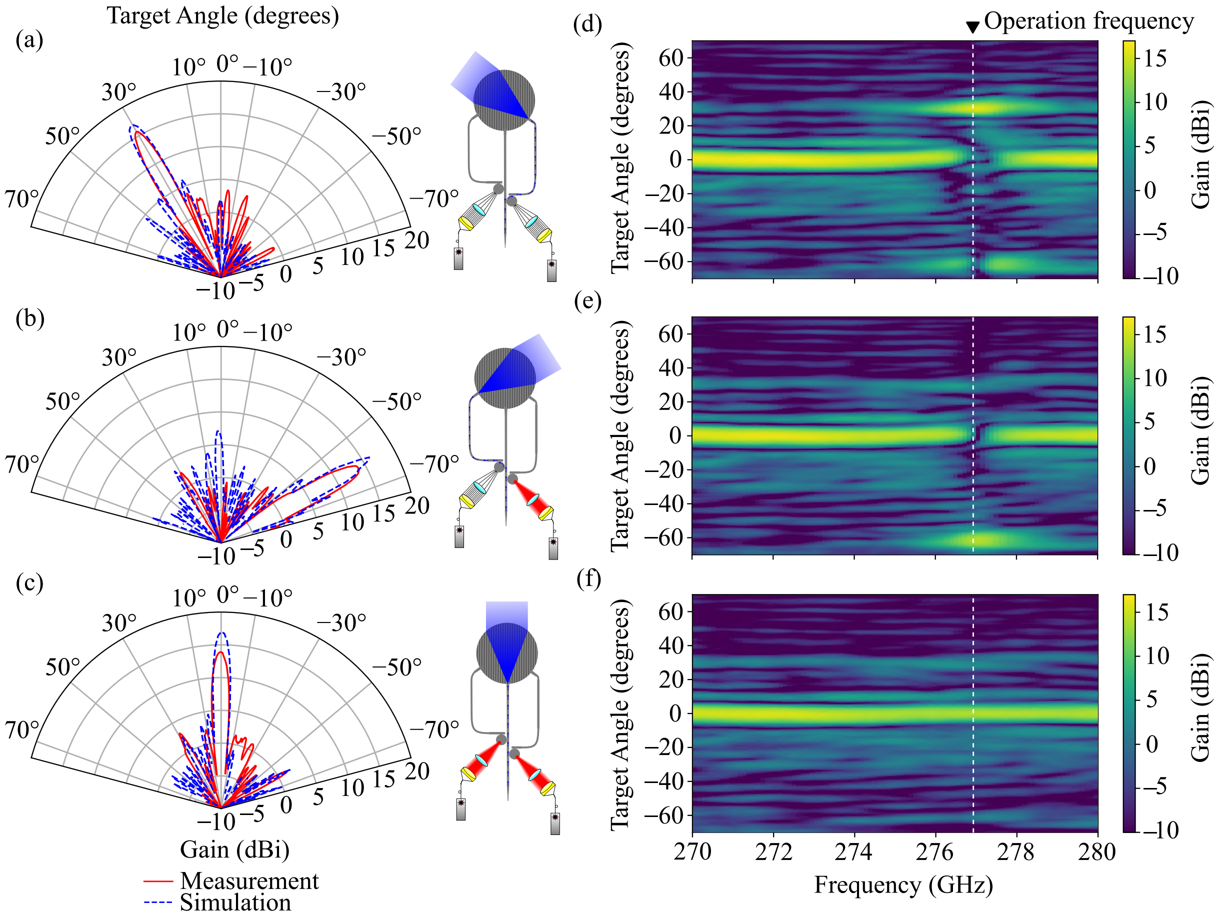

Figure 3.9. Simulated and measured radiation patterns of the three-port switched beam at 276.98 GHz. (a) Both Disks are in the neutral state for 30° output. (b) Disk 1 pumped for −60° output. (c) Both Disks are pumped for 0° output. (d)-(f) Measured radiation patterns of the three-port switched beam according to (a), (b), and (c), respectively.

of the cascaded switches. In addition to the main beams, sidelobes are observed in Fig. 3.9(a) and 3.9(b), and are caused by energy leakages from the disk resonator due to imperfect coupling of the energy into the selected disk resonator. These results successfully illustrate the switching of the beam to the desired angles, which validates the functionality of the integrated switch with the Luneburg lens, thereby emphasising its potential for facilitating a larger number of beams. Nonetheless, it is crucial to highlight that the use of multiple cascaded switches to achieve a larger number of beams leads to an unavoidable increase in insertion loss. From the measured results, the average loss per disk is 1.05 dB.

3.6 Conclusion

The concept of terahertz 1-to-N switches employing disk resonators has been realised on a substrateless dielectric waveguide platform. The proposed switch can operate under photoexcitation of the disk resonators, which direct energy into different output ports. The proposed device can achieve low insertion loss due to the inherent low loss of the platform itself. The experimental results show that a 1-to-3 switch can achieve an average insertion loss of 2.62 dB with a bandwidth of 1.50 GHz, while the respective maximum extinction ratio can reach 13.82 dB. The 1-to-3 switch on this platform has been integrated with a Luneburg lens to realise beam switching. The experimental results demonstrate the designed switched-beam functionality in three directions. This underscores the switching capability of multi-beam switching compared to traditional resonant antennas. These proposed switches can be used as a building block to serve various terahertz applications such as wave routing, beam steering, and photonic switching for sensing, imaging, and communications. This contributes to a promising pathway for future terahertz-integrated systems.

Chapter 4

Optically controlled terahertz modulators on substrateless silicon platform

A terahertz modulator is a crucial component for achieving high-speed communications. Most realised terahertz modulators have focused on wave manipulation in free space. They hardly fulfill the requirements for system-level compactness and miniaturisation. This chapter introduces an optically controlled terahertz modulator on a substrateless silicon platform. This modulator incorporates a dipole resonator and a one-dimensional photonic crystal cavity within the silicon platform. A synergy between these resonant structures enhances the sensitivity of the terahertz waveguide to optical disturbance, resulting in an enhanced modulation depth achieved with a limited optical excitation power. A modulation depth of approximately 5.7 dB is achieved at 273.8 GHz with an optical power of 0.5 mW. With a long carrier lifetime in silicon, the structure serves as a static proof of concept, with potential of improvement towards high-speed modulation. This proposed modulator topology holds significant promise for integration into terahertz systems, particularly for communications.

4.1 Introduction

The rapid growth in data traffic in wireless communications systems calls for terahertz technology as a solution for high-capacity point-to-point links. Within this context, a terahertz modulator emerges as a core device in terahertz communications systems. Numerous studies have been conducted on terahertz modulators operating in free-space environments. These modulators achieved modulation through optical or electrical tuning mechanisms. Optical modulation techniques utilise a strong interaction between lasers and semiconductors, such as silicon (Si) (Gu *et al.*, 2012; Okada and Tanaka, 2011; Xie *et al.*, 2013; Zhang *et al.*, 2015; Cheng and Liu, 2013), gallium arsenide (GaAs) (Padilla *et al.*, 2006), and germanium (Ge) (Lim *et al.*, 2018; Hu *et al.*, 2020b; Tan *et al.*, 2021; Lou *et al.*, 2021), to excite free carriers on metasurfaces, thereby modulating transmitted or reflected terahertz waves. Some realisations possessed a notable advantage in achieving rapid switching at the picosecond scale due to the exceptionally short recombination time of an underlying semiconductor (Smith *et al.*, 1981). However, these modulators required high optical pump power to effectively achieve signal modulation over a large surface area. An electric modulation technique relies on an electrical bias. Several electrically controlled free-space terahertz modulators were proposed (Chen *et al.*, 2006; Huang *et al.*, 2016; Forouzmand *et al.*, 2018; Ju *et al.*, 2011; Brar *et al.*, 2013; Lee *et al.*, 2012; Kim *et al.*, 2018; Dabidian *et al.*, 2016). However, all these metasurface-based electrically or optically excited modulators primarily operate in free-space, which constrains their integrability and compatibility within terahertz integrated systems.

To address this issue, terahertz guided-wave modulators have recently been demonstrated. These modulators rely on electrical modulation techniques. Applying an electrical bias changes the carrier concentration in materials (Rahm *et al.*, 2013), which in turn, affects the boundary conditions of the waveguide. This leads to modifications in the transmittance and reflectance of the guided terahertz waves. A few works have been experimentally demonstrated, including graphene incorporated on silicon rib waveguides (Mittendorff *et al.*, 2017), tunable two-dimensional electron gas microstructures within slot waveguides (Singh and Sonkusale, 2017), and metamaterial chip integrated into waveguides (Zhao *et al.*, 2021). However, there remains a critical need to enhance their modulation performance and interoperability with other components.

Recently, a substrateless silicon platform based on effective-medium-clad waveguides was introduced by Gao *et al.* (2019). This platform was designed specifically to support terahertz integration with high efficiency in broadband. Subsequently, various passive components were demonstrated in multiple studies including filters (Gao *et al.*, 2021b), 2D horn antennas (Liang *et al.*, 2021), waveguide crossings (Lees *et al.*, 2021), and frequency- and polarisation-division multiplexers (Headland *et al.*, 2021b; Gao *et al.*, 2021a). One important component that is still missing from this platform is a modulator.

In this chapter, an optically controlled terahertz amplitude modulator on this substrateless silicon platform is presented. The proposed modulator comprises an effective-medium-clad silicon waveguide, a dipole resonator, and a one-dimensional (1D) photonic crystal cavity. The modulator operates through photoexcitation with a 635 nm red laser. Localised optical excitation of the silicon waveguide causes photoinduced free carriers that change the transmission amplitude. The addition of resonant structures onto the waveguide increases sensitivity of the waveguide to optical disturbance and, as a result, can help enhance modulation depth. Section 4.2 presents the design and working principles, highlighting the enhanced sensitivity of the terahertz waveguide to optical excitation through the interaction of two overlapping resonances. In Section 4.3, the fabrication and measurement processes are presented, while various characteristics of the proposed terahertz modulator are discussed in Section 4.4, including transmission and modulation depth. Section 4.5 provides the conclusion.

4.2 Proposed design

4.2.1 Overview of the structure

Typically, guided terahertz waves on the substrateless dielectric waveguide platform are confined deep inside the 250 µm thick silicon core through total internal reflection (Gao *et al.*, 2019). As such, the effectiveness of modulating these waves through optical excitation is limited, as optical excitation changes the conductivity to the depth of only a few micrometers under the silicon surface. As a result, significant optical pump power is needed to illuminate a long waveguide to induce sensible modulation. On the other hand, narrowing the waveguide would push a larger fraction of the guided wave into the air, not aiding optical interaction either.

To address this, we propose a terahertz amplitude modulator comprising an effective-medium-clad silicon waveguide, loaded with a dipole resonator, and a 1D photonic crystal cavity as shown in Fig. 4.1. This modulator is designed for operation in the E_{11}^{x} mode with in-plane polarisation. The silicon waveguide is created from a monolithic

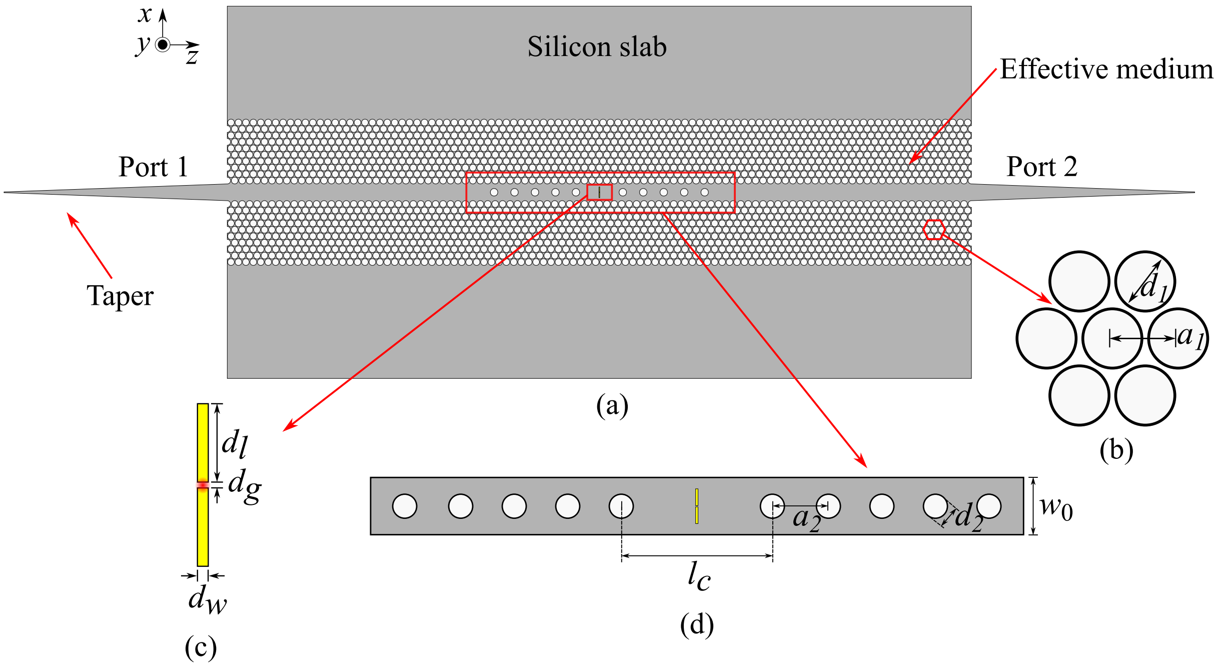

Figure 4.1. Terahertz amplitude modulator using an integrated dipole resonator and a photonic crystal cavity on substrateless dielectric waveguide platform. (a) The waveguide with a width w_0 of 225 µm is built into a high-resistivity silicon wafer with a thickness of 250 µm. The unperforated silicon slab is for handling purpose, while the taper structures are for mode transition between the sample and the feeding hollow waveguides in measurements. (b) The homogeneous claddings are made of a hexagonal lattice of through holes with perforation period a_1 of 100 µm and an air hole diameter d_1 of 90 µm. (c) The dipole resonator consists of 2 metallic patches each with a length d_l of 70 µm and width d_w of 10 µm, separated by a gap d_g of 5 µm, and it is located in the middle of the photonic crystal cavity. The red dot is the pumping area of the red laser. (d) The photonic crystal cavity design consists of air holes arranged in the middle of the waveguide, in two groups of 5 holes with a diameter d_2 of 100 µm, a period a_2 of 275 µm and a cavity length l_c of 630 µm.

silicon slab with a relative permittivity ϵ_{Si} of 11.68 and a loss tangent of 3×10^{-5} (Gao *et al.*, 2019). The claddings are made of air perforation arranged in hexagonal lattices as shown in Fig. 4.1(b) to realise an effective medium, yielding a permittivity contrast to the solid silicon core. The homogenised relative permittivity of the effective medium can be calculated using the Maxwell-Garnett effective medium theory, resulting in ϵ_x, ϵ_y, and ϵ_z values of 2.75, 3.84, and 2.75, respectively.

A planar dipole resonator consists of two thin metallic patches separated by a gap, denoted as d_g as seen in Fig. 4.1(c). The total length of the two dipoles is chosen to be half the wavelength of the targeted operation frequency. This dipole is deposited on top of the silicon core and can couple with in-plane-polarised guided terahertz waves. The design of the photonic crystal cavity incorporates five holes on each side with a diameter of 100 µm. These holes are arranged in the center of the waveguide with a period of 275 µm and a cavity length of 630 µm. The center of the cavity is co-located with the dipole resonator as shown in Fig. 4.1(d). Spectrally aligning the resonances of the metallic dipole and the cavity results in their strong coupling that enhances the sensitivity to optical excitation.

4.2.2 Modulation principle

In this context, we have demonstrated and observed the modulation performance of four different structures including a substrateless silicon platform, a dipole resonator, a 1D photonic crystal cavity, and a modulator combining dipole and photonic crystal cavity. In the neutral state, the red laser is off, resulting in no disturbance to normal operation of those structures. In contrast, in the pump state, the red laser is activated and focused on the silicon surface, resulting in the generation of free carriers within the silicon. In this work, the excitation location is chosen to be in the middle of the structure, with a spot size of 5 µm. This spot size is selected according to the dipole's gap design. The same location and spot size are utilised for fair comparison of modulation performance across different structures.

To validate the modulation concept, all the structure are simulated using CST Microwave Studio. A Drude model is employed to characterise the conductivity of the silicon under pumped power as follows:

$$\sigma_{\mathrm{r}}(\omega) = \frac{\epsilon_0 \omega_p^2 \gamma}{\omega^2 + \gamma^2} , \tag{4.1}$$

where ω is the angular frequency, ϵ_0 is the vacuum permittivity, while the plasma frequency ω_{p} and collision frequency γ depend on the carrier concentration and the carrier mobility. In the pump state, the pumped silicon region in the gap of the dipole is represented by a Drude model using the same plasma and collision frequencies as the setup presented in Chapter 3. The pumped silicon layer is assumed to be homogeneous with a thickness equal to the penetration of the pump laser. The pumped area is circular with a diameter of 5 µm.

We initially demonstrated the substrateless silicon waveguide with no additional structure in two states and observed terahertz transmission through the electric field distribution. In the neutral state, terahertz waves are transmitted from Port 1 to Port 2 with low insertion loss across the bandwidth, as shown in Fig. 4.2(a). In the pump state, optical excitation does not significantly affect terahertz wave transmission, as shown in Fig.4.2(b), allowing the terahertz wave to propagate from Port 1 to Port 2. This is because the conductivity is only changed to a depth of a few micrometers beneath the silicon surface, whereas guided terahertz waves are confined deep inside the silicon core. This suggest the need for a significantly higher optical pump power to effectively modulate the terahertz wave on this platform.

To avoid a significant optical pump power to illuminate a long waveguide, we have introduced a dipole resonator on the surface of the silicon core. In the neutral state, the dipole resonator is off resonance, and thus it behaves as a transparent element for terahertz waves. Consequently, the terahertz wave propagates through it without interaction, as shown in Fig. 4.2(c). In contrast, the optical excitation shorts the two arms of the dipole to tune the strip to a half-wavelength resonance. In this condition, the dipole resonator absorbs and reflects terahertz wave energy. However, the on-resonance dipole does not effectively modulate the terahertz wave, as shown in Fig. 4.2(d). This is because the maximum of the power density of the guided wave is deep in the waveguide core and as a result, the mode barely interacts with the dipole on the surface.

As an alternative, a photonic crystal cavity is implemented on the silicon waveguide by etching a linear hole array with a defect. It is designed to strongly confine and localise waves in the cavity at a targeted frequency. In the neutral state, the photonic crystal cavity causes a strong standing wave with its maximum amplitude within the cavity as shown in Fig. 4.2(e). This allows the wave at the resonance frequency to be transmitted from Port 1 to Port 2. In the pump state, the optical excitation alone is not sufficient to deactivate the resonance frequency of the cavity. This limitation arises because the strong standing wave extends over a larger area than the excitation spot size, resulting in minimal impact on the resonance transmission as shown in Fig. 4.2(f).

The previous considerations indicate that the dipole resonator, when combined with the photonic crystal cavity, has the potential to enhance the interaction with guided terahertz waves. In the neutral state, the terahertz wave that matches the cavity resonance propagates from Port 1 to Port 2, as shown in Fig. 4.2(g), due to the dipole resonator being off resonance and transparent to the terahertz wave. In contrast, in the pump state,

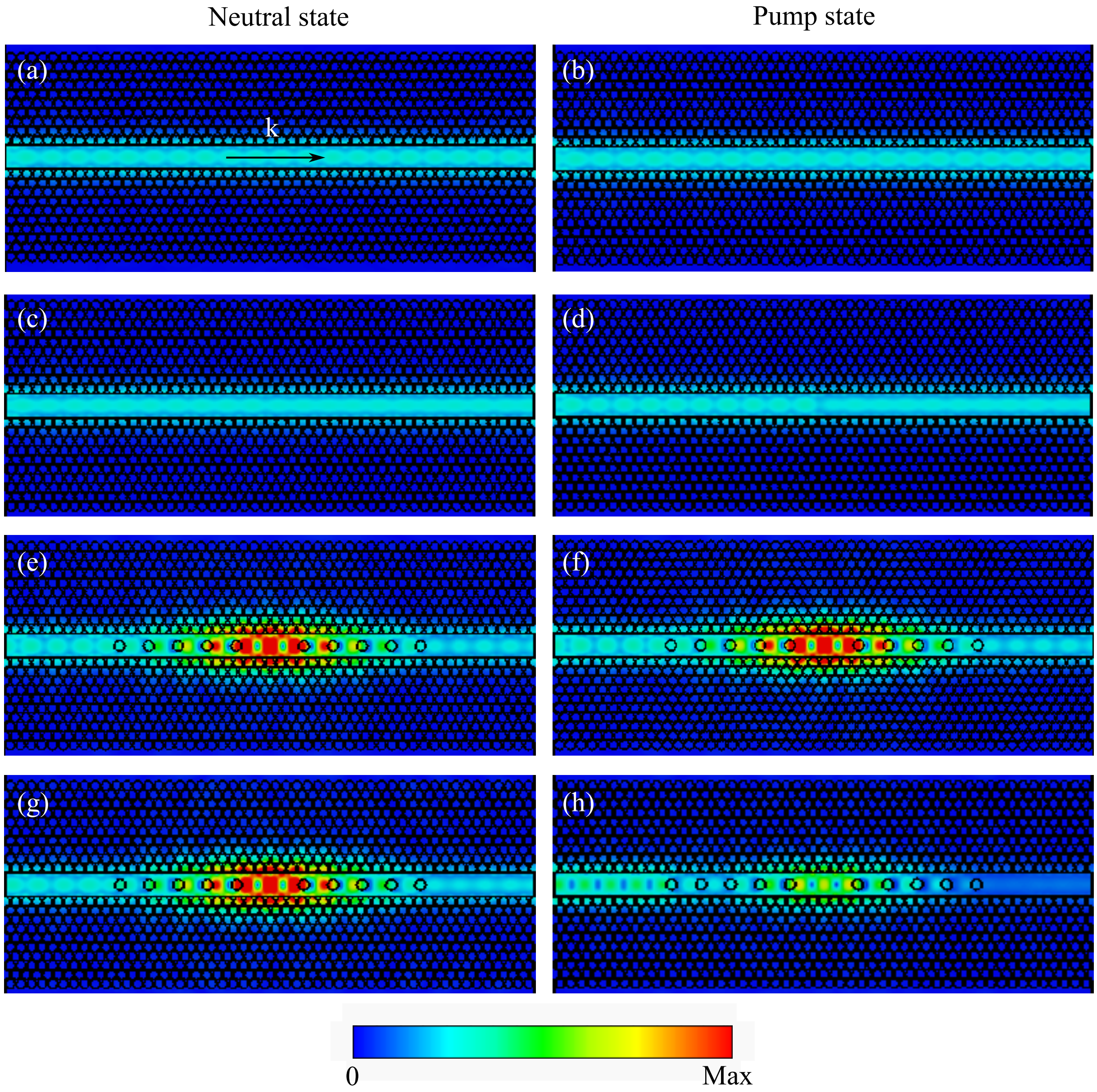

Figure 4.2. Simulated maximum field distributions for four different structures in two states at 275 GHz. (a)–(b) Waveguide. (c)–(d) Waveguide with dipole. (e)–(f) Waveguide with photonic crystal cavity. (g)–(h) Modulator. All plots share the same linear scale.

optical excitation brings the dipole resonator into resonance. This optically activated dipole then strongly interacts with the standing wave established by the photonic crystal cavity, and as a result, the transmission is largely inhibited as shown in Fig. 4.2(h). By employing this method, the terahertz wave modulation is greatly enhanced. Section 4.4 will investigates the effect of fabrication tolerances on the performance of this sensitivity-enhanced modulator.

4.3 Fabrication and measurement

To experimentally validate the modulator concept, a modulator design is fabricated as shown in Fig. 4.3. The sample is fabricated using a 4-inch intrinsic float-zone silicon wafer with a thickness of 250 μm and a resistivity of $>$10 kΩ-cm. The fabrication relies on photolithography, dry and wet etching processes. Firstly, a 2 μm thick silicon dioxide SiO_2 layer is deposited on both sides of the high resistivity silicon wafer. Then, the silicon wafer is patterned using a maskless photolithography process to selectively etch off the SiO_2 in the areas designated for the dipole resonator. Next, layers of Ti/Au with 20/200 nm are deposited and lifted off to realise the dipole resonator. To align and pattern both sides of the SiO_2-coated silicon wafer, a mask is utilised to define the cladding and tapers. The SiO_2 mask is then etched off to expose the underlying silicon. The process continues by dry etching through the high-resistivity silicon layer. Finally, a wet etch of the SiO_2 layer is performed using a 25% hydrofluoric acid solution to complete the fabrication process.

The evaluation of the proposed terahertz amplitude modulator is carried out using a setup similar to that described in Section 2.3. To demonstrate the modulation performance of the modulator, the measurement system involves a red laser operating at a centre wavelength of 635 nm. It is connected to a lensed optical fibre on a 3-axis microblock compact flexure stage, which is used to illuminate the gap of the dipole

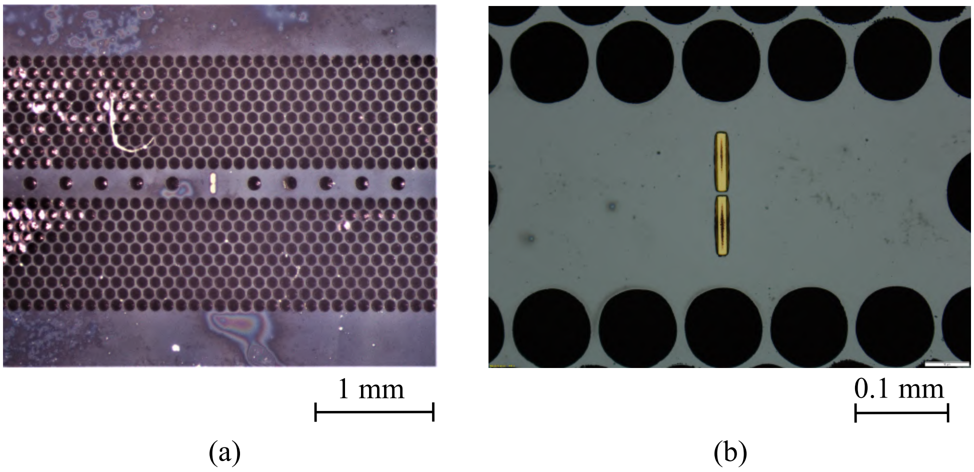

Figure 4.3. Fabricated modulator. (a) Terahertz modulator comprising of the dipole resonator and the photonic crystal cavity on the substrateless silicon platform. (b) Micrograph of the dipole resonator on the top of the waveguide core. The etched through holes of the platform are visible as white holes, while incomplete etching of 6 μm in device thickness results in the blind holes in (a).

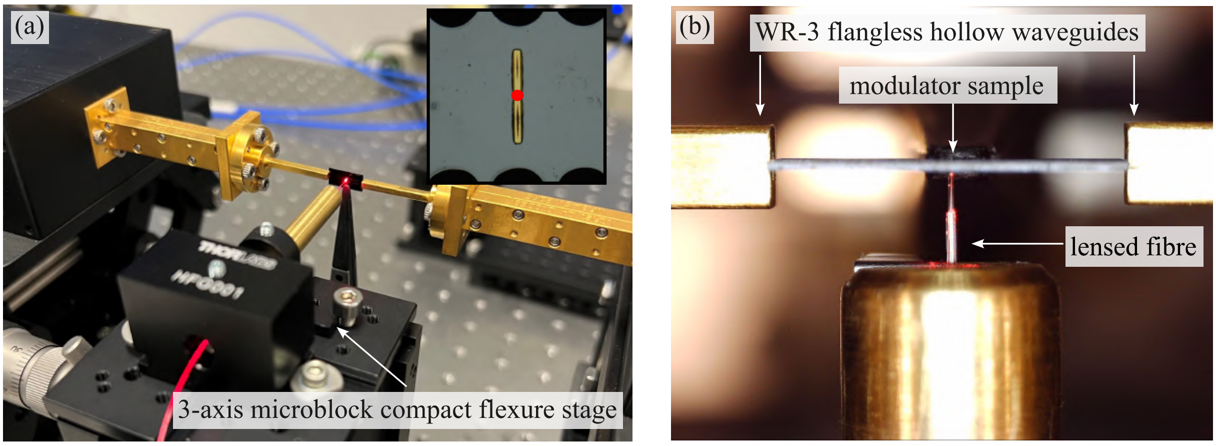
(a)
3-axis microblock compact flexure stage
(b)
WR-3 flangless hollow waveguides
modulator sample
lensed fibre

Figure 4.4. Optical excitation measurement setup. (a) Fabricated sample with the pumped position is at the gap of the dipole. (b) Zoom-in. A single mode 630 nm optical fibre with one large conical lensed tip produces an optical spot with a diameter of 5 ± 0.5 μm. The working distance of the lensed fibre is 20–24 μm. The stripped length of the lensed fibre is 10 ± 1.0 mm, with the other end connecting to an FC/APC connector.

resonator and control its resonance, as shown in Fig. 4.4(a). A microscope camera is used to observe the distance between the sample and the lensed optical fibre to achieve a spot size of 5 μm, as shown in Fig. 4.4(b). The red laser is operated at a maximum pump power of 0.5 mW, resulting in an average optical fluence of 2.54×10^6 W/m^2 within the 2.5 μm radius of the beam focus. The normalisation in this configuration uses a straight waveguide with the same length as the modulator.

4.4 Results and discussion

In general the simulated and measured results presented in Fig. 4.5 agree well. Discrepancies between simulations and measurements are attributed to fabrication tolerances related to incomplete etching and misalignment, which impacts the resonance frequency and the transmission coefficient. From the measured results in Fig. 4.5, in the absence of a red laser, the maximum normalised transmission coefficient reaches −1.9 dB, while under illuminations it decreased to −7.7 dB with 0.5 mW pump power. The modulation depth of the proposed terahertz modulator is around 5.7 dB at 273.8 GHz. The modulation depth of this proposed modulator can be further enhanced to achieve values in the range of 10 dB or higher by increasing the optical power. A stronger optical

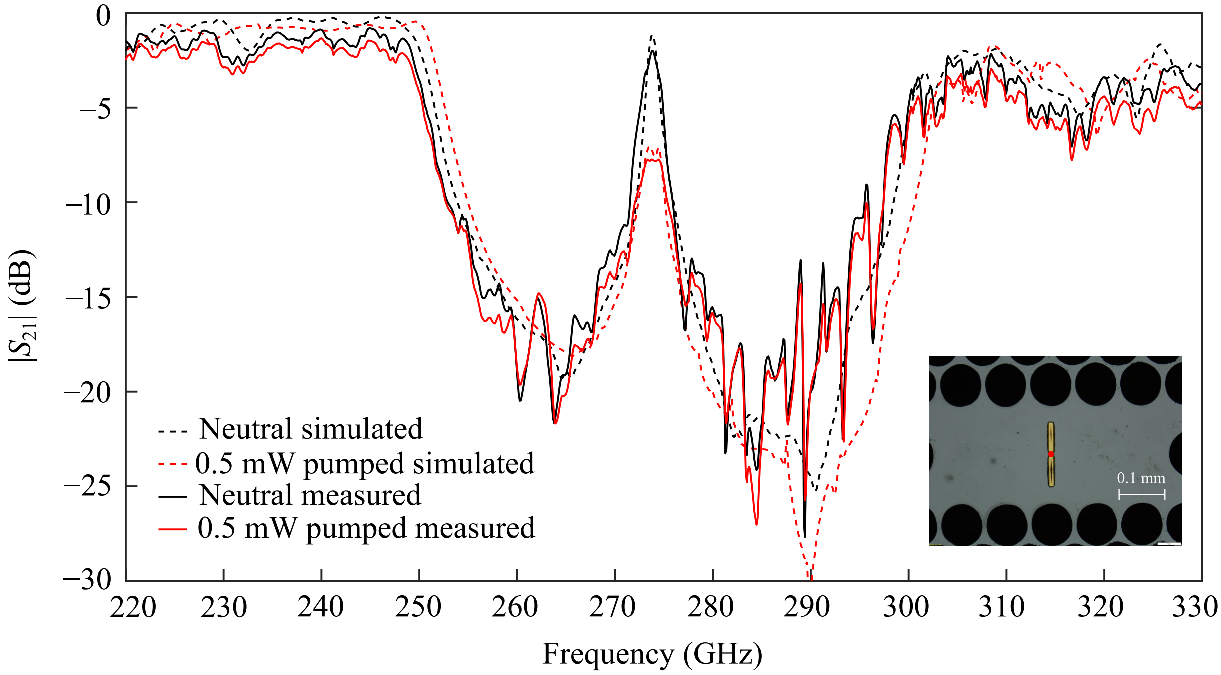

Figure 4.5. Simulated and measured transmission profiles of the proposed terahertz amplitude modulator. A straight waveguide is used as a reference for normalisation. The inset shows the fabricated sample with the pumped region.

fluence provides a higher concentration of photons in a given area, which can result in improved dipole performance, leading to a deeper modulation depth.

In addition, we have conducted several measurements to ensure precise focusing of the red laser on the dipole gap and to avoid the dipole arms and other areas within the cavity. The results, as shown in Fig. 4.6, indicate a stronger coupling and a larger modulation of the terahertz wave when the red laser is accurately focused on the dipole gap. Conversely, when the red laser deviates from the center in both the x and y directions, the modulation gradually decreases until it no longer affects the terahertz wave. This result also affirms the effectiveness of the design involving the dipole and cavity.

To further validate the effectiveness of the design, we fabricated and performed measurements on the photonic crystal cavity without the dipole resonator. The simulated and measured results presented in Fig. 4.7 agree well. The experimentally obtained normalised transmission coefficient of the cavity is −2.7 dB without the red laser. Upon optical excitation, the normalised transmission coefficient decreases to −3.4 dB under a 0.5 mW red laser pump power. This corresponds to a modulation depth of only 0.7 dB at

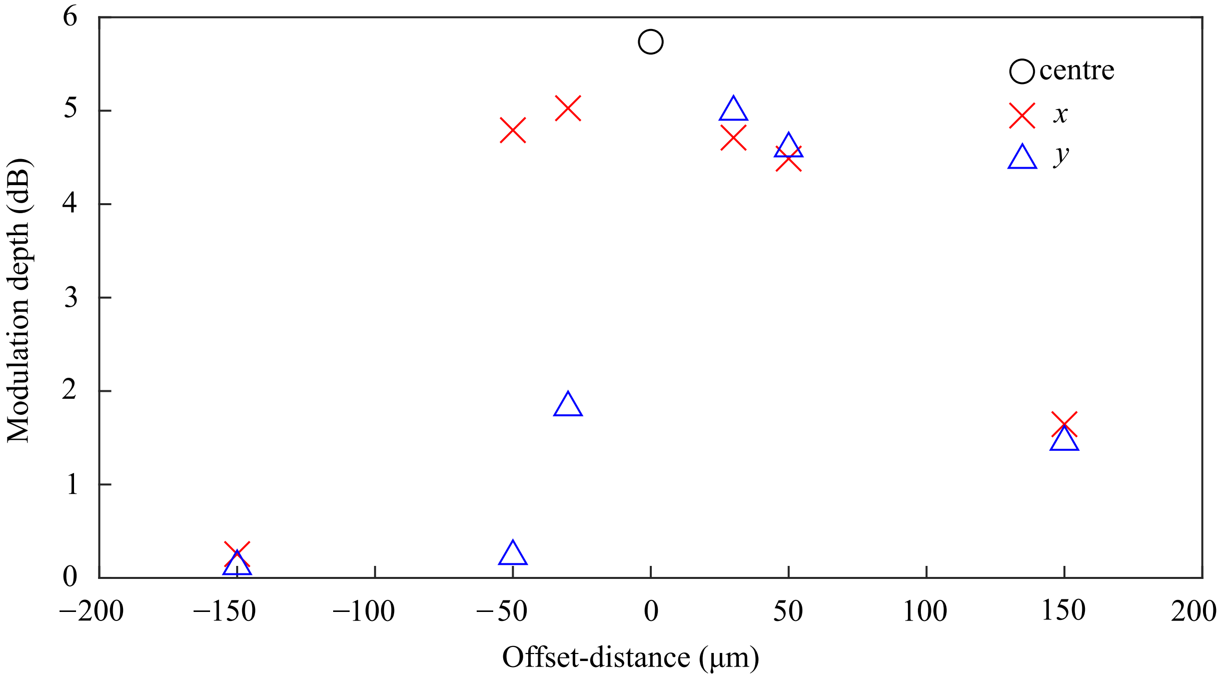

Figure 4.6. Measured transmission of the terahertz amplitude modulator with offset optical excitation.

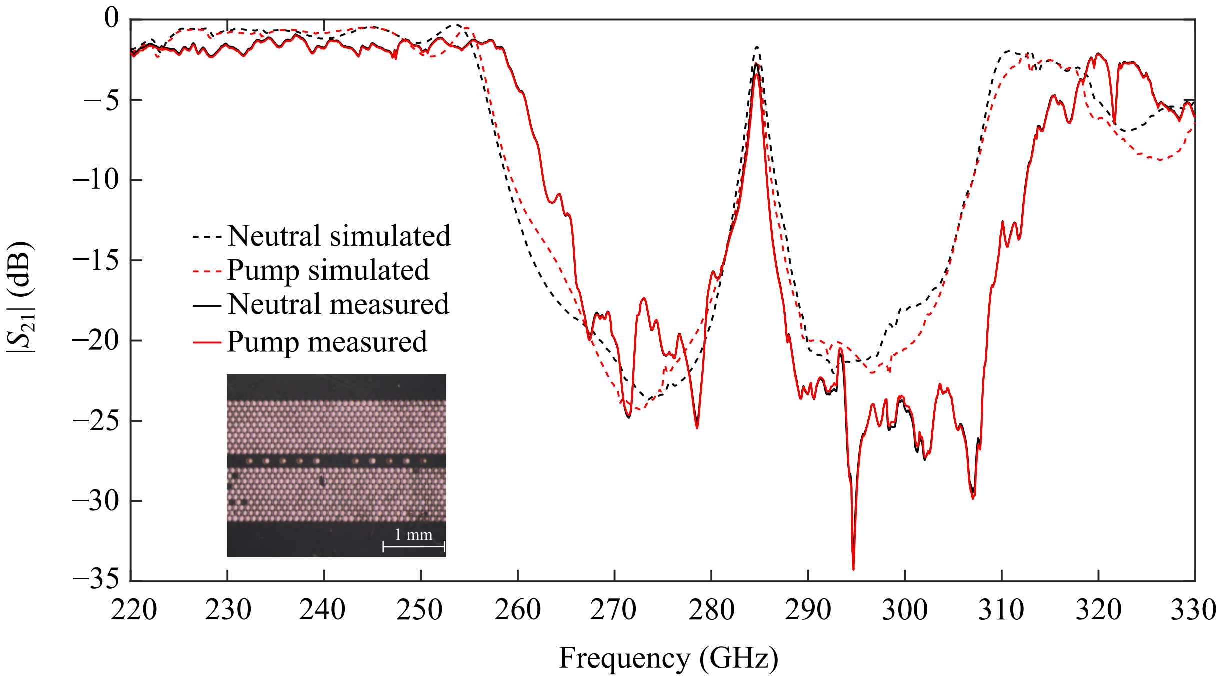

Figure 4.7. Simulated and measured normalised transmission profiles of the photonic crystal cavity without the dipole. The inset shows the fabricated sample.

284.7 GHz. These results confirms that the dipole is required to enhance the modulation sensitivity.

In term of modulation speed, the metallic dipole resonator itself casts a shadow around the photoexcited silicon and effectively causes a large gradient of carrier concentration. This gradient facilitates strong diffusion current that quickly removes photoexcited carriers from the gap. Thus, the modulation speed is not necessarily limited by the long carrier lifetime in silicon. The carrier lifetime and associated modulation speed can be further improved by local ion-implantation that introduces defect-mediated Shockley-Read-Hall (SRH) recombination in silicon to reach 8 ps carrier lifetime (Smith *et al.*, 1981; Hooper *et al.*, 2019), equivalent to a 3-dB modulation bandwidth of >40 GHz. The effect of ion implantation on insertion loss is expected to be minimal due to the deeply subwavelength doping area around the dipole's gap and will be investigated in the future.

4.5 Conclusion

A terahertz amplitude modulator has been realised by utilising an integrated dipole resonator and an photonic crystal cavity on the substrateless silicon platform. The proposed modulator operates by optical excitation that interferes with the resonance system. The synergy between the dipole resonator and the photonic crystal cavity that spatially and spectrally overlap yields a significantly enhanced modulation depth of 5.7 dB, accompanied by a low insertion loss of 1.9 dB. This enhancement is observed in comparison to the sole utilisation of the dipole resonator or the photonic crystal cavity on the same platform. Additionally, this enhanced modulation depth is achieved with a low requirement for pump power. Future work involves improving modulation speed by, e.g., ion implantation in silicon or incorporating a semiconductor with a fast recombination time in the dipole gap. This proposed modulator holds significant promise for the advancement of future terahertz communications systems.

Chapter 5

Summary and Outlook

THIS chapter concludes the work presented in this thesis. Chapter 1 has introduced the research background and motivations of this doctoral thesis, while the original research contributions have been detailed in Chapters 2 to 4, including the high-Q disk resonators, 1-to-N switches, and optically controlled terahertz modulators. The outlook for future developments on the proposed tunable terahertz components on substrateless silicon platform is presented in this chapter.

5.1 Thesis conclusion

This doctoral thesis focused on the development of efficient tunable terahertz components on the substrateless silicon platform for a wide range of applications including sensing, switching, and modulation. A series of integrated disk resonators built into the substrateless silicon waveguide platform to achieve high Q-factor have been proposed. The effective medium concept has demonstrated a degree of freedom to adjust the effective permittivity of the cladding, enabling fine-tuned control over the Q-factor. Photoexcitation of selected areas of the silicon-based platform results in the generation of free carriers, demonstrating strong tunability in resonance. Based on this effect, integrated disk resonators that introduce switching functionality have been developed and presented. To enable beam switching, the integration of a switch with a Luneburg lens on the same platform has been performed. In order to enhance the sensitivity of signal modulation on the substrateless silicon waveguide platform, the modulator combining a dipole resonator and a photonic crystal cavity into the platform has been proposed. The proposed modulator operates by photoexcitation that interferes with the resonance system. All of these tunable terahertz components on the substrateless silicon platform exhibit high efficiency and functionality.

These components can be monolithically integrated with a wide array of other devices, such as transceivers, antennas, and analog signal processing units. The incorporation of high-Q disk resonators alongside signal processing units can enhance sensitivity and improve the quality of terahertz signal detection within the system. Furthermore, the integration of 1-to-N switches into terahertz transceiver systems enables beam steering and the establishment of agile communications links. Optical modulators integrated into the terahertz transceiver system facilitate signal modulation. These integrations collectively enhance and optimise the terahertz system for various applications in sensing and communications.

5.2 Outlook

The achievements in this thesis provide building blocks for the conceptualisation and development of more advanced functionalities of terahertz integrated systems in the future. In addition to this thesis, this section suggests further opportunities to improve and expedite the adoption of the proposed concepts. These research areas include high-speed modulators, attenuators, and graphene modulators.

High-speed modulators

High speed modulators are critical for high capacity communications. One of the primary objectives of this doctoral thesis was to provide a proof-of-concept design for a terahertz modulator with high modulation depth and speed. Enhancing its modulation speed can be achieved through techniques such as ion implantation in silicon or the incorporation of a semiconductor with a fast recombination time in the dipole gap. To this end, it is necessary to investigate the modulation speed of the modulator for future use in terahertz communications systems.

Terahertz attenuators

In terahertz applications, achieving precise control over the attenuation of terahertz wave is beneficial. One possible approach to realising an optically tunable attenuator on the substrateless silicon waveguide platform involves the incorporation of a slotline waveguide and Vivaldi couplers. This design can maximise the interaction between terahertz waves and photoexcited carriers across a broadband spectrum. The slotline waveguide not only allows seamless integration with other components but also offers broadband operation. As a result, future work will focus on investigating and experimentally assessing the design and its performance.

Graphene modulators

Graphene modulators offer a broad bandwidth operation in the terahertz frequency range, relying on electrical modulation mechanisms. Graphene is an alternative material for high-speed modulation due to its unique electrical and optical properties, which allow for rapid changes in signal intensity. A graphene modulator can be realised by introducing a graphene sheet in a slotline integrated onto the substrateless silicon waveguide platform. This modulator adopts a slotline structure to raise the guided waves to the surface for strong interaction with the graphene sheet. The electrical tunability of a single-layer graphene sheet can be utilised to manipulate the terahertz waves. To validate this concept, future work will focus on fabrication and experimental verification.

In conclusion, the proposed tunable terahertz components on the substrateless silicon platform including high-Q disk resonators, 1-to-N switches, and optically tunable modulators hold the promise of significantly advancing terahertz integrated systems. These components together with future developments have the potential to enhance the practical applications for terahertz communications.

Bibliography

Alonso-del Pino-M., Jung-Kubiak-C., Reck-T., Lee-C., and Chattopadhyay-G. (2019). Micromachining for advanced terahertz: Interconnects and packaging techniques at terahertz frequencies, *IEEE Microwave Magazine*, **21**(1), pp. 18–34.

Amarloo-H., Ranjkesh-N., and Safavi-Naeini-S. (2018). Terahertz silicon–BCB–quartz dielectric waveguide: An efficient platform for compact THz systems, *IEEE Transactions on Terahertz Science and Technology*, **8**(2), pp. 201–208.

Arabhavi-A. M., Ciabattini-F., Hamzeloui-S., Flückiger-R., Saranovac-T., Han-D., Marti-D., Bonomo-G., Chaudhary-R., Ostinelli-O., and R. Bolognesi-C. (2022). InP/GaAsSb double heterojunction bipolar transistor emitter-fin technology with f_{MAX}= 1.2 THz, *IEEE Transactions on Electron Devices*, **69**(4), pp. 2122–2129.

Baccarani-G., and Ostoja-P. (1975). Electron mobility empirically related to the phosphorus concentration in silicon, *Solid State Electronics*, **18**(6), pp. 579–580.

Bozzi-M., Georgiadis-A., and Wu-K. (2011). Review of substrate-integrated waveguide circuits and antennas, *IET Microwaves, Antennas and Propagation*, **5**(8), pp. 909–920.

Brar-V. W., Jang-M. S., Sherrott-M., Lopez-J. J., and Atwater-H. A. (2013). Highly confined tunable mid-infrared plasmonics in graphene nanoresonators, *Nano Letters*, **13**(6), pp. 2541–2547.

Chen-C.-W., Lin-Y.-C., Chang-C.-H., Yu-P., Shieh-J.-M., and Pan-C.-L. (2010). Frequency-dependent complex conductivities and dielectric responses of indium tin oxide thin films from the visible to the far-infrared, *IEEE Journal of Quantum Electronics*, **46**(12), pp. 1746–1754.

Cheng-L.-J., and Liu-L. (2013). Optical modulation of continuous terahertz waves towards cost-effective reconfigurable quasi-optical terahertz components, *Optics Express*, **21**(23), pp. 28657–28667.

CHEN-H.-T., PADILLA-W. J., ZIDE-J. M., GOSSARD-A. C., TAYLOR-A. J., AND AVERITT-R. D. (2006). Active terahertz metamaterial devices, *Nature*, **444**(7119), pp. 597–600.

CHOY-T. C. (2015). *Effective Medium Theory: Principles and Applications*, Vol. 165, Oxford University Press.

CUI-T., BAI-B., AND SUN-H.-B. (2019). Tunable metasurfaces based on active materials, *Advanced Functional Materials*, **29**(10), art. no. 1806692.

DABIDIAN-N., DUTTA-GUPTA-S., KHOLMANOV-I., LAI-K., LU-F., LEE-J., JIN-M., TRENDAFILOV-S., KHANIKAEV-A., FALLAHAZAD-B., EMANUEL-T., MIKHAIL A-B., AND GENNADY-S. (2016). Experimental demonstration of phase modulation and motion sensing using graphene-integrated metasurfaces, *Nano Letters*, **16**(6), pp. 3607–3615.

DAI-J., ZHANG-J., ZHANG-W., AND GRISCHKOWSKY-D. (2004). Terahertz time-domain spectroscopy characterization of the far-infrared absorption and index of refraction of high-resistivity, float-zone silicon, *Journal of the Optical Society of America B*, **21**(7), pp. 1379–1386.

DARMAWAN-S., AND CHIN-M. (2006). Critical coupling, oscillation, reflection, and transmission in optical waveguide-ring resonator systems, *Journal of the Optical Society of America B*, **23**(5), pp. 834–841.

DECHWECHPRASIT-P., AKO-R. T., SRIRAM-S., FUMEAUX-C., AND WITHAYACHUMNANKUL-W. (2023a). Terahertz disk resonator on a substrateless dielectric waveguide platform, *Optics Letters*, **48**(17), pp. 4685–4688.

DECHWECHPRASIT-P., FUMEAUX-C., AND WITHAYACHUMNANKUL-W. (2021). Integrated resonant cavities on substrateless terahertz dielectric waveguide platform, *2021 46th International Conference on Infrared, Millimeter and Terahertz Waves (IRMMW-THz)*, IEEE, pp. 1–2.

DECHWECHPRASIT-P., FUMEAUX-C., AND WITHAYACHUMNANKUL-W. (2022). Integrated disk resonator on substrateless dielectric waveguide platform for terahertz switch applications, *2022 47th International Conference on Infrared, Millimeter and Terahertz Waves (IRMMW-THz)*, IEEE, pp. 1–2.

DECHWECHPRASIT-P., LEES-H., HEADLAND-D., FUMEAUX-C., AND WITHAYACHUMNANKUL-W. (2023b). 1-to-N terahertz integrated switches enabling multi-beam antennas, *Optica*, **10**(11), pp. 1551–1558.

DING-J.-Q., SHI-S.-C., ZHOU-K., ZHAO-Y., LIU-D., AND WU-W. (2017). WR-3 band quasi-elliptical waveguide filters using higher order mode resonances, *IEEE Transactions on Terahertz Science and Technology*, **7**(3), pp. 302–309.

FOROUZMAND-A., SALARY-M. M., INAMPUDI-S., AND MOSALLAEI-H. (2018). A tunable multigate indium-tin-oxide-assisted all-dielectric metasurface, *Advanced Optical Materials*, **6**(7), art. no. 1701275.

GAO-W., FUMEAUX-C., AND WITHAYACHUMNANKUL-W. (2021a). Terahertz integrated polarization beam splitter based on effective-medium waveguide, *2021 IEEE Asia-Pacific Microwave Conference (APMC)*, IEEE, pp. 100–102.

GAO-W., LEE-W. S., FUMEAUX-C., AND WITHAYACHUMNANKUL-W. (2021b). Effective-medium-clad Bragg grating filters, *APL Photonics*, **6**(7), art. no. 076105.

GAO-W., LEE-W. S., YU-X., FUJITA-M., NAGATSUMA-T., FUMEAUX-C., AND WITHAYACHUMNANKUL-W. (2020). Characteristics of effective-medium-clad dielectric waveguides, *IEEE Transactions on Terahertz Science and Technology*, **11**(1), pp. 28–41.

GAO-W., YU-X., FUJITA-M., NAGATSUMA-T., FUMEAUX-C., AND WITHAYACHUMNANKUL-W. (2019). Effective-medium-cladded dielectric waveguides for terahertz waves, *Optics Express*, **27**(26), pp. 38721–38734.

GREEN-M. A., AND KEEVERS-M. J. (1995). Optical properties of intrinsic silicon at 300 K, *Progress in Photovoltaics: Research and Applications*, **3**(3), pp. 189–192.

GU-J., SINGH-R., LIU-X., ZHANG-X., MA-Y., ZHANG-S., MAIER-S. A., TIAN-Z., AZAD-A. K., CHEN-H.-T., , ANTOINETTE J-T., JIAGUANG-H., AND WEILI-Z. (2012). Active control of electromagnetically induced transparency analogue in terahertz metamaterials, *Nature Communications*, **3**(1), art. no. 1151.

HANHAM-S. M., AHMAD-M. M., LUCYSZYN-S., AND KLEIN-N. (2017). LED-switchable high-Q packaged THz microbeam resonators, *IEEE Transactions on Terahertz Science and Technology*, **7**(2), pp. 199–208.

HEADLAND-D., FUJITA-M., AND NAGATSUMA-T. (2019). Bragg-mirror suppression for enhanced bandwidth in terahertz photonic crystal waveguides, *IEEE Journal of Selected Topics in Quantum Electronics*, **26**(2), pp. 1–9.

HEADLAND-D., KLEIN-A. K., FUJITA-M., AND NAGATSUMA-T. (2021a). Dielectric slot-coupled half-Maxwell fisheye lens as octave-bandwidth beam expander for terahertz-range applications, *APL Photonics*, **6**(9), art. no. 096104.

HEADLAND-D., WITHAYACHUMNANKUL-W., FUJITA-M., AND NAGATSUMA-T. (2021b). Gratingless integrated tunneling multiplexer for terahertz waves, *Optica*, **8**(5), pp. 621–629.

HEADLAND-D., WITHAYACHUMNANKUL-W., YAMADA-R., FUJITA-M., AND NAGATSUMA-T. (2018). Terahertz multi-beam antenna using photonic crystal waveguide and Luneburg lens, *APL Photonics*, **3**(12), art. no. 126105.

HEADLAND-D., WITHAYACHUMNANKUL-W., YU-X., FUJITA-M., AND NAGATSUMA-T. (2020). Unclad microphotonics for terahertz waveguides and systems, *Journal of Lightwave Technology*, **38**(24), pp. 6853–6862.

HEYES-J. E., WITHAYACHUMNANKUL-W., GRADY-N. K., CHOWDHURY-D. R., AZAD-A. K., AND CHEN-H.-T. (2014). Hybrid metasurface for ultra-broadband terahertz modulation, *Applied Physics Letters*, **105**(18), art. no. 181108.

HOOPER-I., GRANT-N., BARR-L., HORNETT-S., MURPHY-J. D., AND HENDRY-E. (2019). High efficiency photomodulators for millimeter wave and THz radiation, *Scientific Reports*, **9**(1), art. no. 18304.

HUANG-Y.-W., LEE-H. W. H., SOKHOYAN-R., PALA-R. A., THYAGARAJAN-K., HAN-S., TSAI-D. P., AND ATWATER-H. A. (2016). Gate-tunable conducting oxide metasurfaces, *Nano Letters*, **16**(9), pp. 5319–5325.

HU-Y., JIANG-T., ZHOU-J., HAO-H., SUN-H., OUYANG-H., TONG-M., TANG-Y., LI-H., YOU-J., XIN-Z., ZHONGJIE-X., AND XIANGAI-C. (2020a). Ultrafast terahertz transmission/group delay switching in photoactive WSe_2-functionalized metaphotonic devices, *Nano Energy*, **68**, art. no. 104280.

HU-Y., YOU-J., TONG-M., ZHENG-X., XU-Z., CHENG-X., AND JIANG-T. (2020b). Pump-color selective control of ultrafast all-optical switching dynamics in metaphotonic devices, *Advanced Science*, **7**(14), art. no. 2000799.

IWAMATSU-S., ALI-M., ESTÉVEZ-J. L. F., GRZESLO-M., MAKHLOUF-S., RIVERA-A., CARPINTERO-G., AND STÖHR-A. (2023). Terahertz photodiode integration with multi-octave-bandwidth dielectric rod waveguide probe, *Optics Letters*, **48**(23), pp. 6275–6278.

JALALI-B., YEGNANARAYANAN-S., YOON-T., YOSHIMOTO-T., RENDINA-I., AND COPPINGER-F. (1998). Advances in silicon-on-insulator optoelectronics, *IEEE Journal of selected topics in Quantum Electronics*, **4**(6), pp. 938–947.

JOANNOPOULOS-J. D., MEADE-R., AND WINN-J. N. (1995). Photonic Crystals, *Molding the Flow of Light*.

JU-L., GENG-B., HORNG-J., GIRIT-C., MARTIN-M., HAO-Z., BECHTEL-H. A., LIANG-X., ZETTL-A., SHEN-Y. R., AND FENG-W. (2011). Graphene plasmonics for tunable terahertz metamaterials, *Nature Nanotechnology*, **6**(10), pp. 630–634.

KANNEGULLA-A., SHAMS-M. I. B., LIU-L., AND CHENG-L.-J. (2015). Photo-induced spatial modulation of THz waves: opportunities and limitations, *Optics Express*, **23**(25), pp. 32098–32112.

KARIMI-A., SHAH-U., AND OBERHAMMER-J. (2023). Compact high-isolation sub-THz micro-electromechanical SPST switch, *European Microwave Week 2023*.

KIM-T.-T., KIM-H., KENNEY-M., PARK-H. S., KIM-H.-D., MIN-B., AND ZHANG-S. (2018). Amplitude modulation of anomalously refracted terahertz waves with gated-graphene metasurfaces, *Advanced Optical Materials*, **6**(1), art. no. 1700507.

KOENIG-S., LOPEZ-DIAZ-D., ANTES-J., BOES-F., HENNEBERGER-R., LEUTHER-A., TESSMANN-A., SCHMOGROW-R., HILLERKUSS-D., PALMER-R., THOMAS-Z., CHRISTIAN-K., WOLFGANG, FREUDE OLIVER-A., JUERG-L., AND INGMAR-K. (2013). Wireless sub-THz communication system with high data rate, *Nature Photonics*, **7**(12), pp. 977–981.

KUMAR-A., GUPTA-M., PITCHAPPA-P., TAN-T. C., CHATTOPADHYAY-U., DUCOURNAU-G., WANG-N., CHONG-Y., AND SINGH-R. (2022a). Active ultrahigh-Q (0.2×10^6) THz topological cavities on a chip, *Advanced Materials*, **34**(27), art. no. 2202370.

KUMAR-A., GUPTA-M., PITCHAPPA-P., TAN-Y. J., WANG-N., AND SINGH-R. (2022b). Topological sensor on a silicon chip, *Applied Physics Letters*, **121**(1), art. no. 011101.

KUMAR-A., GUPTA-M., PITCHAPPA-P., WANG-N., SZRIFTGISER-P., DUCOURNAU-G., AND SINGH-R. (2022c). Phototunable chip-scale topological photonics: 160 Gbps waveguide and demultiplexer for THz 6G communication, *Nature Communications*, **13**(1), art. no. 5404.

KUO-Y.-H., LUO-J., HIDEHISA-T., ILYA-D., ALEX K-Y-J., HAROLD R-F., AND WILLIAM H-S. (2006). Ring resonator-based electrooptic polymer traveling-wave modulator, *Journal of Lightwave Technology*, **24**(9), pp. 3514–3519.

LEE-K. K., LIM-D. R., KIMERLING-L. C., SHIN-J., AND CERRINA-F. (2001). Fabrication of ultralow-loss Si/SiO$_2$ waveguides by roughness reduction, *Optics Letters*, **26**(23), pp. 1888–1890.

LEE-S. H., CHOI-M., KIM-T.-T., LEE-S., LIU-M., YIN-X., CHOI-H. K., LEE-S. S., CHOI-C.-G., CHOI-S.-Y., XIANG-Z., AND BUMKI-M. (2012). Switching terahertz waves with gate-controlled active graphene metamaterials, *Nature Materials*, **11**(11), pp. 936–941.

LEES-H., GAO-W., AND WITHAYACHUMNANKUL-W. (2021). All-silicon, low-cross-talk terahertz waveguide crossing based on effective medium, *Optics Letters*, **46**(21), pp. 5469–5472.

LIANG-J., GAO-W., LEES-H., AND WITHAYACHUMNANKUL-W. (2021). All-silicon terahertz planar horn antenna, *IEEE Antennas and Wireless Propagation Letters*, **20**(11), pp. 2181–2185.

LI-J., TAO-J., CHEN-Z. H., AND HUANG-X. G. (2016). All-optical controlling based on nonlinear graphene plasmonic waveguides, *Optics Express*, **24**(19), pp. 22169–22176.

LIM-W. X., MANJAPPA-M., SRIVASTAVA-Y. K., CONG-L., KUMAR-A., MACDONALD-K. F., AND SINGH-R. (2018). Ultrafast all-optical switching of germanium-based flexible metaphotonic devices, *Advanced Materials*, **30**(9), art. no. 1705331.

LIU-X., HUANG-J., CHEN-H., QIAN-Z., MA-J., SUN-X., FAN-S., AND SUN-Y. (2022). Terahertz topological photonic waveguide switch for on-chip communication, *Photonics Research*, **10**(4), pp. 1090–1096.

LOU-J., XU-X., HUANG-Y., YU-Y., WANG-J., FANG-G., LIANG-J., FAN-C., AND CHANG-C. (2021). Optically controlled ultrafast terahertz metadevices with ultralow pump threshold, *Small*, **17**(44), art. no. 2104275.

MALEKABADI-A., CHARLEBOIS-S. A., DESLANDES-D., AND BOONE-F. (2014). High-resistivity silicon dielectric ribbon waveguide for single-mode low-loss propagation at F/G-bands, *IEEE Transactions on Terahertz Science and Technology*, **4**(4), pp. 447–453.

MEADE-R. D. V., JOHNSON-S. G., AND WINN-J. N. (2008). Photonic crystals: Molding the flow of light.

MITTENDORFF-M., LI-S., AND MURPHY-T. E. (2017). Graphene-based waveguide-integrated terahertz modulator, *American Chemical Society Photonics*, **4**(2), pp. 316–321.

MURANO-K., WATANABE-I., KASAMATSU-A., SUZUKI-S., ASADA-M., WITHAYACHUMNANKUL-W., TANAKA-T., AND MONNAI-Y. (2016). Low-profile terahertz radar based on broadband leaky-wave beam steering, *IEEE Transactions on Terahertz Science and Technology*, **7**(1), pp. 60–69.

NAGATSUMA-T. (2011). Terahertz technologies: present and future, *IEICE Electronics Express*, **8**(14), pp. 1127–1142.

NAGATSUMA-T., DUCOURNAU-G., AND RENAUD-C. C. (2016). Advances in terahertz communications accelerated by photonics, *Nature Photonics*, **10**(6), pp. 371–379.

OKADA-T., AND TANAKA-K. (2011). Photo-designed terahertz devices, *Scientific Reports*, **1**(1), art. no. 121.

OKAMOTO-K. (2021). *Fundamentals of Optical Waveguides*, Elsevier.

PADILLA-W., ARONSSON-M., HIGHSTRETE-C., LEE-M., TAYLOR-A., AND AVERITT-R. (2007). Electrically resonant terahertz metamaterials: Theoretical and experimental investigations, *Physical Review B*, **75**(4), art. no. 041102.

PADILLA-W. J., TAYLOR-A. J., HIGHSTRETE-C., LEE-M., AND AVERITT-R. D. (2006). Dynamical electric and magnetic metamaterial response at terahertz frequencies, *Physical Review Letters*, **96**(10), art. no. 107401.

POZAR-D. M. (2011). *Microwave Engineering*, John Wiley and Sons.

RAHM-M., LI-J.-S., AND PADILLA-W. J. (2013). THz wave modulators: a brief review on different modulation techniques, *Journal of Infrared, Millimeter, and Terahertz Waves*, **34**, pp. 1–27.

REICHEL-K. S., LOZADA-SMITH-N., JOSHIPURA-I. D., MA-J., SHRESTHA-R., MENDIS-R., DICKEY-M. D., AND MITTLEMAN-D. M. (2018). Electrically reconfigurable terahertz signal processing devices using liquid metal components, *Nature Communications*, **9**(1), art. no. 4202.

SASAO-K., AND MONNAI-Y. (2020). Variable terahertz attenuator integrated on nonradiative guide using photoinduced carriers, *IEEE Transactions on Terahertz Science and Technology*, **10**(3), pp. 256–259.

SCHNEIDER-T., WIATREK-A., PREUSSLER-S., GRIGAT-M., AND BRAUN-R.-P. (2012). Link budget analysis for terahertz fixed wireless links, *IEEE Transactions on Terahertz Science and Technology*, **2**(2), pp. 250–256.

SCHROTER-M., AND PAWLAK-A. (2018). SiGe heterojunction bipolar transistor technology for sub-mm-wave electronics—state-of-the-art and future prospects, *2018 IEEE 18th Topical Meeting on Silicon Monolithic Integrated Circuits in RF Systems (SiRF)*, IEEE, pp. 60–63.

SCHWELB-O., AND FRIGYES-I. (2003). Vernier operation of series-coupled optical microring resonator filters, *Microwave and Optical Technology Letters*, **39**(4), pp. 257–261.

SHCHERBAKOV-M. R., LIU-S., ZUBYUK-V. V., VASKIN-A., VABISHCHEVICH-P. P., KEELER-G., PERTSCH-T., DOLGOVA-T. V., STAUDE-I., BRENER-I., AND ANDREY A-F. (2017). Ultrafast all-optical tuning of direct-gap semiconductor metasurfaces, *Nature Communications*, **8**(1), pp. 1–6.

SINGH-P., AND SONKUSALE-S. (2017). High speed terahertz modulator on the chip based on tunable terahertz slot waveguide, *Scientific Reports*, **7**(1), art. no. 40933.

SINGH-R., ROCKSTUHL-C., LEDERER-F., AND ZHANG-W. (2009). The impact of nearest neighbor interaction on the resonances in terahertz metamaterials, *Applied Physics Letters*.

SMITH-P., AUSTON-D., JOHNSON-A., AND AUGUSTYNIAK-W. (1981). Picosecond photoconductivity in radiation-damaged silicon-on-sapphire films, *Applied Physics Letters*, **38**(1), pp. 47–50.

SRIVASTAVA-Y. K., CHATURVEDI-A., MANJAPPA-M., KUMAR-A., DAYAL-G., KLOC-C., AND SINGH-R. (2017). MoS_2 for ultrafast all-optical switching and modulation of THz Fano metaphotonic devices, *Advanced Optical Materials*, **5**(23), art. no. 1700762.

SUBASHIEV-A. V., AND LURYI-S. (2006). Modal control in semiconductor optical waveguides with uniaxially patterned layers, *Journal of Lightwave Technology*, **24**(3), art. no. 1513.

SURESH-M. I., SCHWEFEL-H. G. L., AND VOGT-D. W. (2023). Gallium arsenide whispering gallery mode resonators for terahertz photonics, *Opt. Express*, **31**(20), pp. 33056–33063.

TAN-T. C., SRIVASTAVA-Y. K., AKO-R. T., WANG-W., BHASKARAN-M., SRIRAM-S., AL-NAIB-I., PLUM-E., AND SINGH-R. (2021). Active control of nanodielectric-induced THz quasi-BIC in flexible metasurfaces: a platform for modulation and sensing, *Advanced Materials*, **33**(27), art. no. 2100836.

TSURUDA-K., FUJITA-M., AND NAGATSUMA-T. (2015). Extremely low-loss terahertz waveguide based on silicon photonic-crystal slab, *Optics Express*, **23**(25), pp. 31977–31990.

URTEAGA-M., GRIFFITH-Z., SEO-M., HACKER-J., AND RODWELL-M. J. (2017). InP HBT technologies for THz integrated circuits, *Proceedings of the IEEE*, **105**(6), pp. 1051–1067.

VOGT-D. W. (2022). Terahertz microresonators for material characterisation, *Optical Materials Express*, **12**(9), pp. 3463–3470.

VOGT-D. W., AND LEONHARDT-R. (2017). Fano resonances in a high-Q terahertz whispering-gallery mode resonator coupled to a multi-mode waveguide, *Optics Letters*, **42**(21), pp. 4359–4362.

VOGT-D. W., JONES-A. H., AND LEONHARDT-R. (2019). Free-space coupling to symmetric high-Q terahertz whispering-gallery mode resonators, *Optics Letters*, **44**(9), pp. 2220–2223.

VOGT-D. W., JONES-A. H., HAASE-T. A., AND LEONHARDT-R. (2020). Subwavelength thick ultrahigh-Q terahertz disc microresonators, *Photonics Research*, **8**(7), pp. 1183–1188.

VOGT-D. W., JONES-A. H., SCHWEFEL-H. G., AND LEONHARDT-R. (2018). Prism coupling of high-Q terahertz whispering-gallery-modes over two octaves from 0.2 THz to 1.1 THz, *Optics Express*, **26**(24), pp. 31190–31198.

WANG-Z., YUAN-S., DONG-G., WANG-R., CHEN-L., WU-X., AND ZHANG-X. (2019). On-chip single-mode high-Q terahertz whispering gallery mode resonator, *Optics Letters*, **44**(11), pp. 2835–2838.

WHITAKER-L., MARKMAN-B., AND RODWELL-M. J. (2023). Self-aligned InGaAs channel MOS-HEMTs for high frequency applications, *2023 Device Research Conference (DRC)*, IEEE, pp. 1–2.

WITHAYACHUMNANKUL-W., AND ABBOTT-D. (2009). Metamaterials in the terahertz regime, *IEEE Photonics Journal*, **1**(2), pp. 99–118.

WITHAYACHUMNANKUL-W., FUJITA-M., AND NAGATSUMA-T. (2018). Integrated silicon photonic crystals toward terahertz communications, *Advanced Optical Materials*, **6**(16), art. no. 1800401.

WU-K., BOZZI-M., AND FONSECA-N. J. (2021). Substrate integrated transmission lines: Review and applications, *IEEE Journal of Microwaves*, **1**(1), pp. 345–363.

XIE-J., ZHU-X., ZANG-X., CHENG-Q., CHEN-L., AND ZHU-Y. (2018). Terahertz integrated device: high-Q silicon dielectric resonators, *Optical Materials Express*, **8**(1), pp. 50–58.

XIE-Z., WANG-X., YE-J., FENG-S., SUN-W., AKALIN-T., AND ZHANG-Y. (2013). Spatial terahertz modulator, *Scientific Reports*, **3**(1), art. no. 3347.

YARIV-A. (2002). Critical coupling and its control in optical waveguide-ring resonator systems, *IEEE Photonics Technology Letters*, **14**(4), pp. 483–485.

YEE-C. M., AND SHERWIN-M. S. (2009). High-Q terahertz microcavities in silicon photonic crystal slabs, *Applied Physics Letters*, **94**(15), art. no. 154104.

YUAN-S., CHEN-L., WANG-Z., WANG-R., WU-X., AND ZHANG-X. (2019). Mode coupling in a terahertz multi-mode whispering-gallery-mode resonator, *Optics Letters*, **44**(8), pp. 2020–2023.

YU-X., HOSODA-Y., MIYAMOTO-T., OBATA-K., KIM-J.-Y., FUJITA-M., AND NAGATSUMA-T. (2019a). Terahertz fibre transmission link using resonant tunnelling diodes integrated with photonic-crystal waveguides, *Electronics Letters*, **55**(7), pp. 398–400.

YU-X., KIM-J.-Y., FUJITA-M., AND NAGATSUMA-T. (2018). Highly stable terahertz resonant tunneling diode oscillator coupled to photonic-crystal cavity, *2018 Asia-Pacific Microwave Conference (APMC)*, IEEE, pp. 114–116.

YU-X., KIM-J.-Y., FUJITA-M., AND NAGATSUMA-T. (2019b). Efficient mode converter to deep-subwavelength region with photonic-crystal waveguide platform for terahertz applications, *Optics Express*, **27**(20), pp. 28707–28721.

ZAKARIA-N., SALLEH-M. M., KHAN-Z. I., AND HASSAN-A. A. (2010). Compact coplanar waveguide pseudo-elliptic filter at microwave frequencies, *2010 IEEE Symposium on Industrial Electronics and Applications (ISIEA)*, IEEE, pp. 537–540.

ZHANG-B., LV-L., HE-T., CHEN-T., ZANG-M., ZHONG-L., WANG-X., SHEN-J., AND HOU-Y. (2015). Active terahertz device based on optically controlled organometal halide perovskite, *Applied Physics Letters*, **107**(9), art. no. 093301.

ZHAO-Y., VORA-K., LIU-X., BÖGEL-G. V., SEIDL-K., AND BALZER-J. C. (2022). Photonic crystal resonator in the millimeter/terahertz range as a thin film sensor for future biosensor applications, *Journal of Infrared, Millimeter, and Terahertz Waves*, **43**(5-6), pp. 426–444.

ZHAO-Y., ZHANG-Y., LIANG-S., QIAO-S., YANG-Z., HAO-Z., AND JIAO-L. (2021). High-speed terahertz modulation based on the control of metamaterial mode to waveguide mode, *2021 14th UK-Europe-China Workshop on Millimetre-Waves and Terahertz Technologies (UCMMT)*, IEEE, pp. 1–3.

Biography

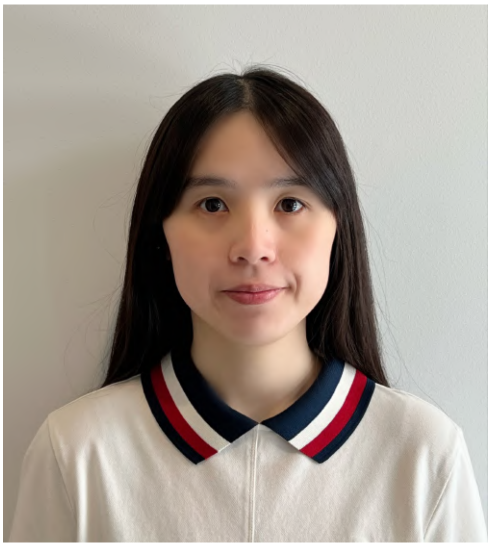

Panisa Dechwechprasit was born in Bangkok, Thailand in 1994. She received her Bachelor of Engineering in the field of Biomedical Engineering from Srinakharinwirot University, Thailand in 2017. In 2019, she received her Master of Engineering in the field of Computer Science and Information Engineering from the National Formosa University, Taiwan. After obtaining her master degree, she immediately joined the Terahertz Engineering Laboratory, School of Electrical and Mechanical Engineering at the University of Adelaide in the area of tunable terahertz components on a substrateless silicon platform under the supervision of Prof. Withawat Withayachumnankul and Prof. Christophe Fumeaux.

During her candidature, she received the ECMS Divisional Scholarship form the Faculty of Engineering, Computer and Mathematical Sciences. In 2022, she received the Frank Perry Travel Scholarship to attend the 47th International Conference on Infrared, Millimeter and Terahertz Waves (IRMMW-THz) in Delft, Netherlands. During her Ph.D. candidature, she was an area manager in the Terahertz Engineering Laboratory. Her research interests involve tunable terahertz components on a substrateless silicon platform.